Design and Fabrication of a Lightweight Robotic Manipulator

Matthew MacGregor Roy
Department of Mechanical Engineering
McGill University

A Thesis Submitted to the Faculty of Graduate Studies and Research in Partial Fulfillment of the Requirements of the Degree of Master of Engineering

0-612-37282-0

Abstract

Typically, when a robotic manipulator undergoes rapid acceleration, there is a commensurate loss in end-effector positional accuracy. To achieve high accuracy of the working end, massive links are usually required. Conversely, to achieve high accelerations, thin and flimsy links have to be employed, only to be plagued by large end-effector vibrations and long settling times. However, this traditional tradeoff can be circumvented through the application of high-performance materials such as graphite/epoxy which exhibits high stiffness-to-weight and strength-to-weight ratios as well as good damping properties. This thesis describes the process of designing and fabricating the three principal mechanisms of an anthropomorphic lightweight robotic arm: the shoulder joint, elbow joint and wrist. Each mechanism comprises various components which were individually optimized for strength, stiffness and weight by finite-element analysis. The components were then synthesized into shoulder, elbow and wrist mechanisms that exhibited excellent workspace, low backlash and low friction. This lightweight composite manipulator was developed as a multi-purpose arm for possible applications in the remote repair of hydroelectric power lines, minesweeping and the handling of hazardous materials.

Résumé

Normalement, lorsqu'un bras robotique accélère rapidement, il perd en conséquence de la précision. Pour atteindre un bon niveau de précision, la structure du bras doit être massive. A l'inverse, pour atteindre de hautes accélérations, la structure doit être mince et donc flexible. Néanmoins, en utilisant des matériaux composites, comme les fibres de carbone, ayant des excellentes qualités au niveau de force et rigidité, il est possible de concevoir et fabriquer un bras robotique très léger et performant. Cette thèse décrit le processus de concevoir et fabriquer les trois mécanismes principaux d'un bras robotique, c'est à dire l'épaule, le coude et le poignet, ayant les dimensions, la mobilité, et la performance approximatives d'un bras humain. Chaque mécanisme comprend plusieurs pièces qui ont été optimalisés pour la force, rigidité et poids par l'analyse d'éléments finis. Ce bras robotique a été conçu comme un bras polyvalent pouvant servir à plusieurs fins, notamment l'entretien des lignes hydroélectriques, la chasse des mines ainsi que la manipulation des objets toxiques ou dangereux.

Table of Contents

List of Figures

List of Tables

List of Symbols

[A]	=	laminate modulus matrix
[a]	=	laminate compliance matrix
c	=	shear factor
D	=	flexural rigidity
d	=	diameter
E	=	isotropic Young's modulus
E_X	=	Young's modulus in fiber direction
E_Y	=	Young's modulus in matrix direction
E_S	=	Young's modulus in shear
F	=	actuator force
G	=	shear modulus
h	=	laminate thickness
I	=	moment of inertia
K	=	shear correction factor
K_1	=	longitudinal (x-direction) beam curvature
K_2	=	induced transverse (y-direction) beam curvature
K_3	=	induced transverse (z-direction) beam curvature
L	=	length of beam
m	=	mass
P	=	applied shear load
Q	=	first moment of area
r	=	radius
S	=	shear strength
t	=	thickness
w	=	total static deflection of box-beam
X_T	=	tensile strength in fiber direction
X_C	=	compressive strength in fiber direction
y	=	total static deflection of shaft
Y_T	=	tensile strength in matrix direction
Y_C	=	compressive strength in matrix direction
ε	=	strain
θ	=	ply orientation angle
ρ	=	density
σ_B	=	bending stress
σ_b	=	bearing stress
σ_t	=	tensile stress
σ_s	=	shear-out stress
τ	=	shear stress

Acknowledgments

There are numerous people to whom I owe a great deal of gratitude and without whose constant help, guidance and stewardship this endeavour never would have come to fruition. Primarily, I would like to single out two individuals, Professors Larry Lessard and Vincent Hayward, who were endlessly patient and kind and who found time for me even when they had none. I also owe a considerable debt of gratitude to Dr. Ian Sinclair of MPB Technologies of Pointe Claire for his forbearance and for making this collaboration possible in the first place. An engineer's conceptions are often limited by the talents of his machinists, but this was hardly true in my case. The bulk of the machining was done at the Physics Department machine shop by Joel Rous and Eddie Del Campo under the diligent supervision of Steve Kecani while the remainder of the machining was done at the Machine Tool Lab by Roy Westgate, Tony Micozzi and Danen Chellan under the aegis of Louis Hueppin. To all seven machinists, I would like to express my heartfelt thanks for a job well done. Not only was your professionalism unsurpassed but your advice, support and fellowship were very much appreciated. I would also like to thank the members of the Composites Group for their assistance and camaraderie, in particular Diao, John and Hamid for helping with the composites, and Tareck for his humour and friendship. Finally, nothing would have been possible without the unwavering support of the two greatest parents, Marilyn and Bob, to whom this work is dedicated.

Chapter 1

Introduction

One of the primary objectives of robotics engineering is to design a manipulator capable of high link accelerations without sacrificing positional accuracy. For industrial robotic applications, such as automated assembly, productivity is related to the speed and settling time of a robotic arm while the positional accuracy determines the quality control. These two attributes, high link acceleration and positional accuracy, were once considered mutually exclusive. Precise robotic manipulators were traditionally massive and slow whereas fast ones were light and flimsy, and afflicted with unwieldy end-effector vibrations. However, the traditional tradeoff can been circumvented by two methods. Firstly, the dynamic response of each link can be incorporated into the control algorithm for the entire arm. This is achieved by carefully quantifying the flexure and damping of each link and then using a computer control system to correct for the end-effector's vibrations [1-5]. The performance of robotic manipulators can also be dramatically improved by reducing the inertia of the links while maintaining stiffness and strength [6-8]. This can be achieved by utilizing materials with very high stiffness-to-weight and strength-to-weight ratios, such as composite materials, and by optimizing the geometry of various components to minimize deflection and stress.

Another fundamental concern of current robotics research has been to develop anthropomorphic (human-like) arms capable of emulating the dexterity, manipulability, workspace volume and payload-to-weight ratio of a human arm. Not only would anthropomorphic arms be ideal prostheses, but they would also make teleoperation in space, undersea and in hazardous environments that much easier for the human controller.

The advent of high-performance composite materials, with very high stiffness-to-weight and strength-to-weight ratios as well as excellent damping properties, have made it possible for robotics engineers to build manipulators with excellent stiffness, strength, damping and low inertia. This thesis describes the process of designing and fabricating a lightweight, anthropomorphic, seven-degree-of-freedom manipulator using graphite/epoxy, aluminum and stainless steel to achieve human-like payload-to-weight ratio, dexterity, manipulability, workspace volume as well as good positional accuracy without sacrificing link accelerations.

1.1 Definitions: What is a robot?

From an etymological standpoint, the term "robot" was derived from the Czech "robotnik" or "robota", meaning slave or subservience, and gained prominence from the science fiction play *RUR (Rossum's Universal Robots)* by Czechoslovakian playwright Karel Capek [9]. Nowadays, robots come in every imaginable shape and size. This has undoubtedly contributed to the apparent confusion regarding what exactly a robot is. For instance, what distinguishes a robotic arm from a crane, gantry or an excavator? Numerous robotics organizations around the world have attempted to clarify the issue by proffering definitions of a robot. In 1987, the Robotics Industry Association (RIA) of the United States [10,11] defined a robot as a "reprogrammable multifunctional machine designed to manipulate material, parts, tools, or specialized devices through variable programmed motion for the performance of a variety of tasks." The Swedish Industrial Robot Association [10] defined a robot as "an automatically controlled, reprogrammable, multi-purpose manipulative machine with or without locomotion for use in industrial automation applications."

Lest there be any confusion, the terms "robotic arm" and "manipulator" shall be hereafter treated as synonymous and often referred to simply as an "arm." While on the topic of terminology, "end-effector" shall be taken to mean the endpoint of the arm, which could be the tip of a tool, the center of mass of a payload or in the absence of any such object, merely the geometrical center of the gripper or hand.

1.2 Classifying Robotic Arms:

There are endless ways to classify robotic arms: by structure, by function, by the number of degrees-of-freedom (DOF), by the type of actuation, by whether the joints are serial or parallel, et cetera. The Japanese Industrial Robot Association (JIRA) classifies robots according to their capability [10]:

- Class 1 is a simple manual, teleoperated manipulator
- Class 2 is a fixed sequence robot that can only perform a single preordained task
- Class 3 is a variable sequence robot whose single task can be easily reprogrammed to perform a different task
- Class 4 is a robot that can replicate a sequence of steps shown to it by a human operator
- Class 5 is a numerically controlled robot
- Class 6 is an intelligent robot capable of sensing and navigating through its environment

Outside Japan, perhaps the most common approach [12-14] is to classify manipulators according to their structure. Accordingly, there are essentially six types of robot arms:

1. Cartesian Coordinate Arms (all prismatic joints)
2. Polar Coordinate Arms (3 revolute degrees-of-freedom)
3. Cylindrical Coordinate Arms (2 prismatic joints and 1 revolute joint)
4. Revolute Coordinate Arms (4 or more revolute DOF)
5. Serpentine Arms (numerous joints articulated in series like the human spine)
6. Anthropomorphic Arms (consisting of shoulder, elbow and wrist joints)

1.3 Problems Associated with Current Robotic Arms

Most current robotic arms possess poor payload-to-weight ratios, poor damping and lack anthropomorphic manipulability and dexterity. Futhermore, the essential dynamic tradeoff between link acceleration and positional accuracy hasn't been properly addressed. Conventionally, to design a fast-moving arm required that the links have low inertia. Inevitably, this resulted in large end-effector vibrations and long settling times. Conversely, to achieve high positional accuracy required bulky, massive links. Due to the large inertia of the links, these robotic arms cannot move rapidly and require inordinate amounts of power. However, robot researchers the world over have already begun to offer many design solutions to these problems. To achieve the manipulability and dexterity of a human arm, innovative new joint mechanisms have been studied. The advent of high stiffness-to-weight composite materials has also had a significant impact on overcoming the conventional tradeoff between link acceleration and positional accuracy.

1.4 Objectives

Bearing in mind the aforementioned shortcomings, the objectives of this thesis were to design and fabricate a lightweight anthropomorphic robotic arm that has a payload-to-weight ratio of 1:1, a maximum static deflection of 1 cm while lifting its maximum payload of 10 kg and, furthermore, exhibits the manipulability, dexterity and workspace volume approaching that of a human arm. To achieve these design criteria, each component of the shoulder, elbow and wrist mechanisms was optimized for maximum strength-to-weight and stiffness-to-weight ratios.

1.5 Potential Lightarm Applications

Lightarm was designed as a general-purpose arm with a wide variety of potential applications ranging from repairing high-voltage power lines to minesweeping [15]. Spin-off applications may include bomb disposal and handling hazardous materials, both chemical and nuclear [16]. In the nuclear industry, however, radiation is known to have a deleterious effect not only on the robot's electronic circuitry but also on the mechanical properties of carbon fiber reinforced plastics [17]. Yet another possible application for Lightarm is in medicine where surgeons have already begun to use robotic manipulators such as the AESOP arm for certain simple procedures [18,19]. To perform such a wide gamut of tasks, the robotic arm must be able to emulate the speed, precision, payload, dexterity and workspace volume of its human counterpart.

Chapter 2

2.1 Survey of Current Robotic Arms

Due to the sheer number of manipulators currently in existence, it would not be feasible to discuss and describe each one. So, in the interest of brevity, the following is a mere sampling of some interesting arms that have bearing on the current work.

A payload-to-weight ratio of 1:1 has already been achieved with the ROTEX manipulator, shown in Figure 2.1, designed by Gombert et al. at the German Aerospace Research Establishment [20,21].

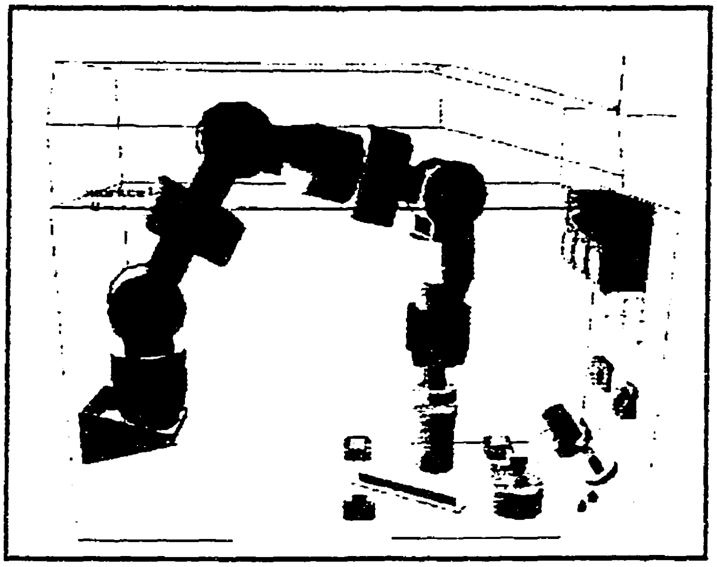

Figure 2.1: ROTEX

The Canadian Space Agency and SPAR Aerospace used graphite/epoxy to design the space shuttle's remote manipulator system, the Canadarm, shown in Figure 2.2. For space applications, lightness, high stiffness-to-weight ratio and good damping properties are typically the driving factors in the design. The next generation of space robots, such as the Space Station Remote Manipulator System (SSRMS), are using graphite/epoxy to make even lighter, stiffer and better performing arms.

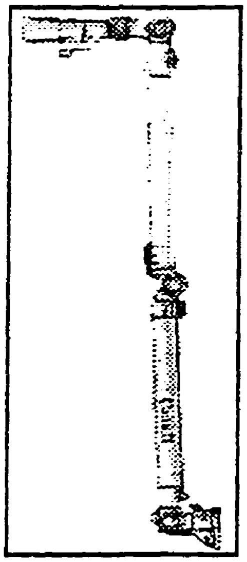

Figure 2.2: Canadarm

Schilling Robotic Systems has developed a high-performance six-degree-of-freedom titanium arm called the Titan II. Powered by hydraulics running at a pressure of 3000 psi (20.7 MPa), the Titan II has an excellent lift capacity of 240 pounds (109 kg) at its full extension of 76 inches (1.9 m) and is designed to operate in radioactive, toxic-chemical, high-voltage and undersea environments [22]. Schilling's latest refinements are embodied in the Titan III, shown in Figure 2.3.

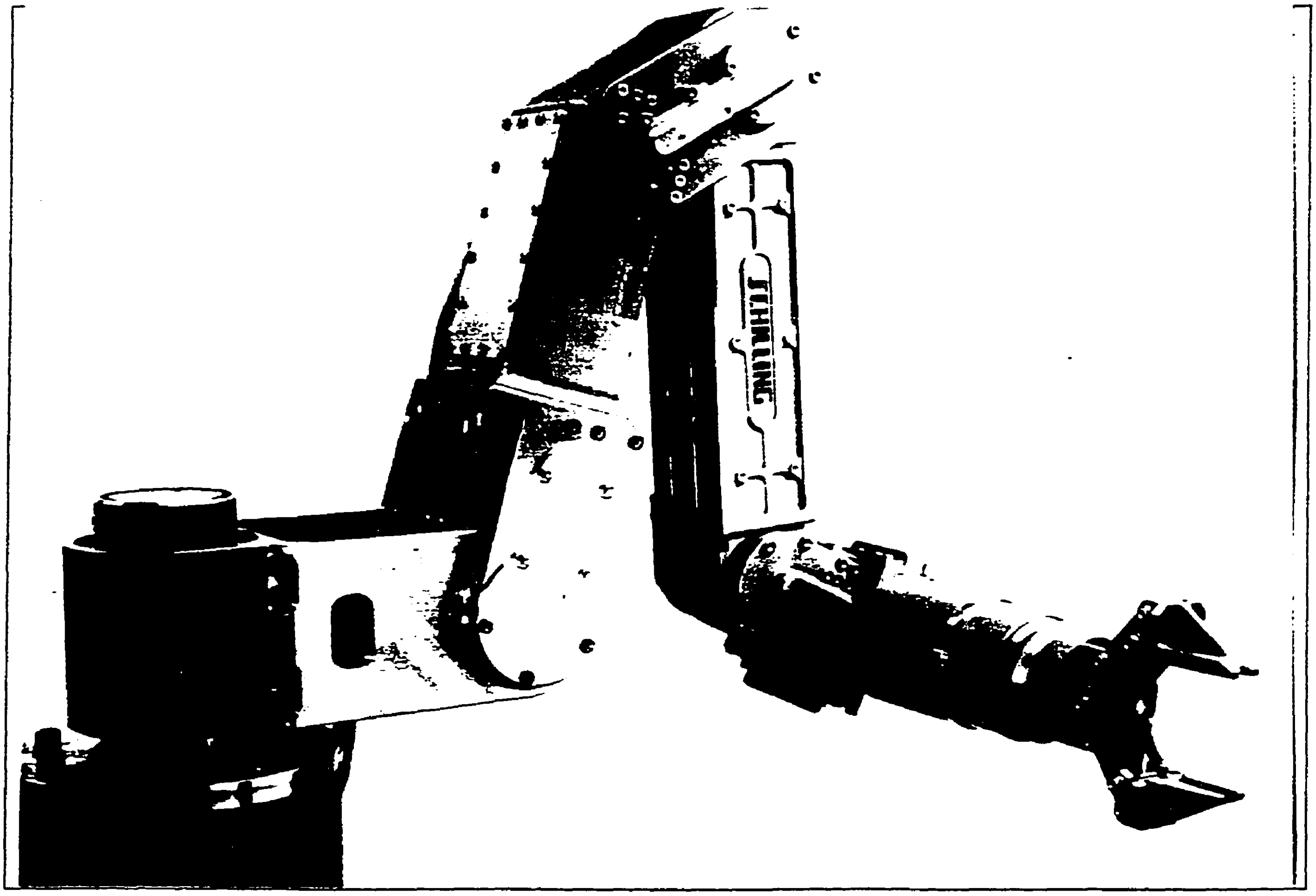

Figure 2.3: Titan III © 1997 GEC Alsthom Schilling Robotic Systems, Inc.

Mitsubishi Heavy Industries produce the six-degree-of-freedom Paint Coating Robot. Powered by hydraulics running at a relatively low 7.4 MPa, the 450-kilogram arm is rated for a payload of only 5 kilograms [23]. This is a typical example of an industrial robotic manipulator which is designed for simple, repetitive manufacturing tasks. In many of these applications, the introduction of high-performance manipulators would not be justified because the task the arm performs (e.g. spray-painting) requires neither speed nor precision.

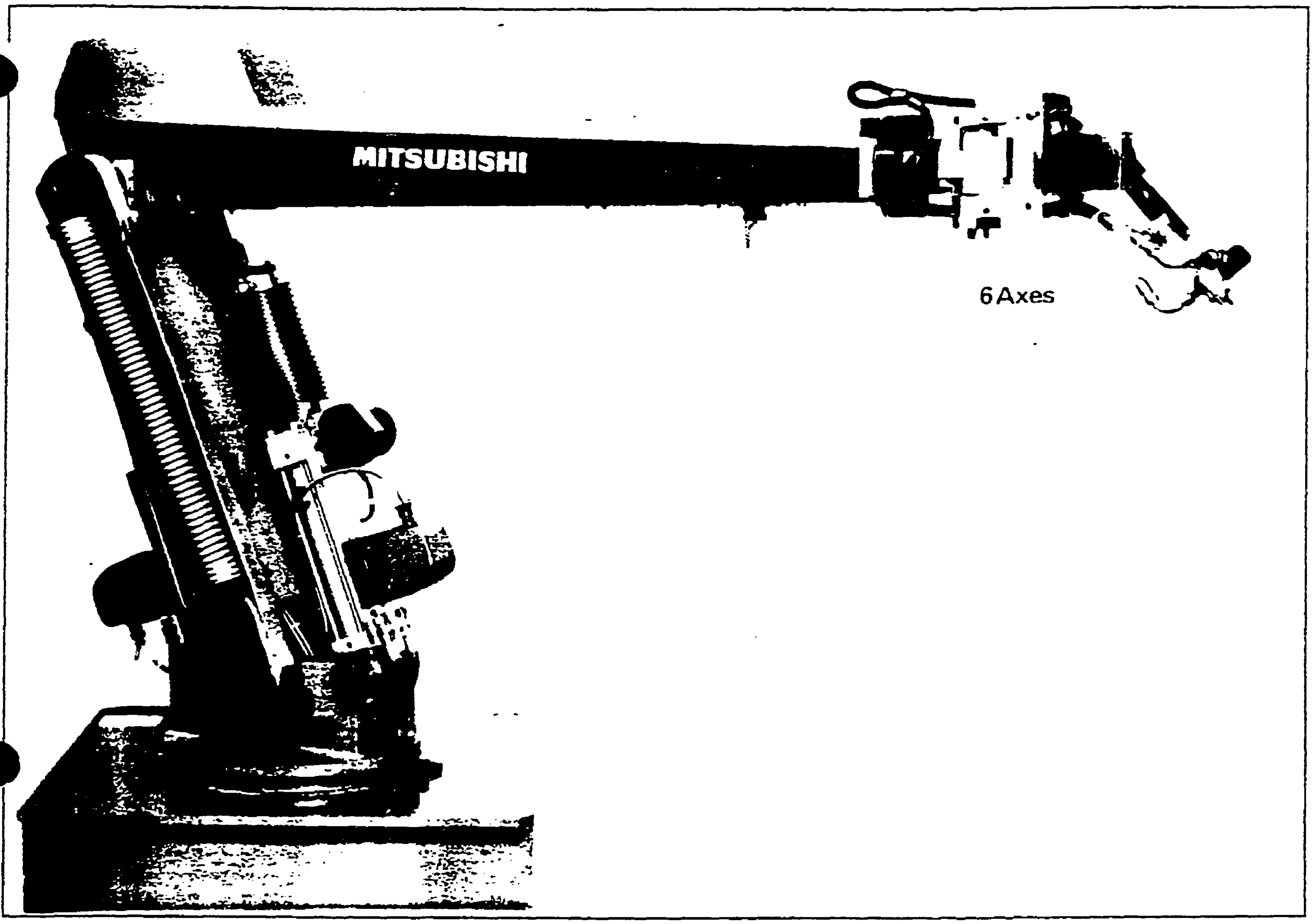

Figure 2.4: Mitsubishi Paint Coating Robot

The six-degree-of-freedom, servo-hydraulic MTS 200A was designed as a general-purpose industrial manipulator for handling tools, loading and unloading machines and performing inspection on production lines. The MTS arm is capable of achieving a repeatable end-point precision of ± 0.13 mm with loads up to 100 kg [24].

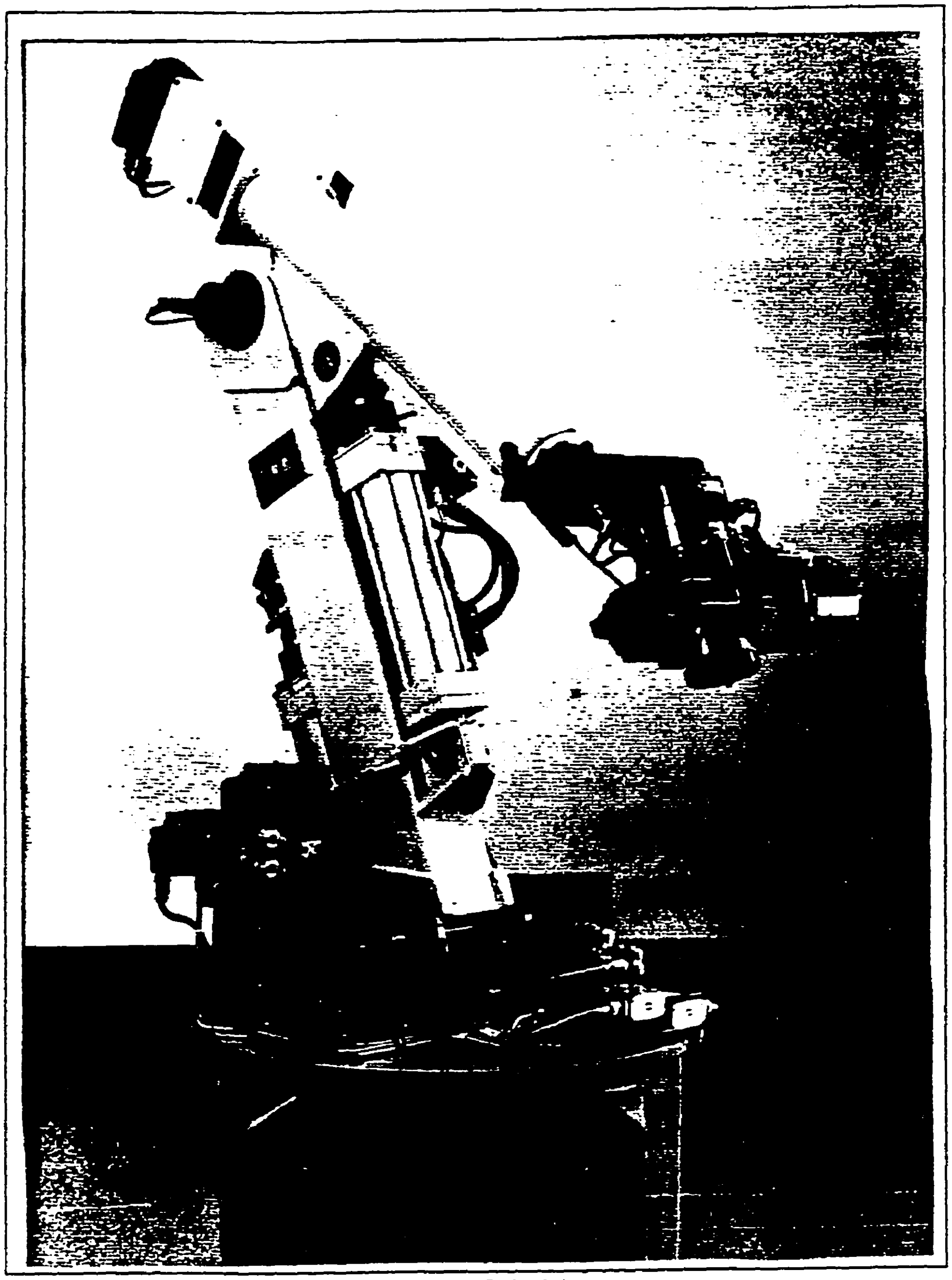

Figure 2.5: MTS 200A

The ASEA Industrial Robot System IRB 6/2 is another general-purpose six-degree-of-freedom industrial robot. Designed for grinding, polishing, arc welding, deburring, and assembly, this arm has a rated payload of 6 kg and a repeatability of ±0.2 mm [25].

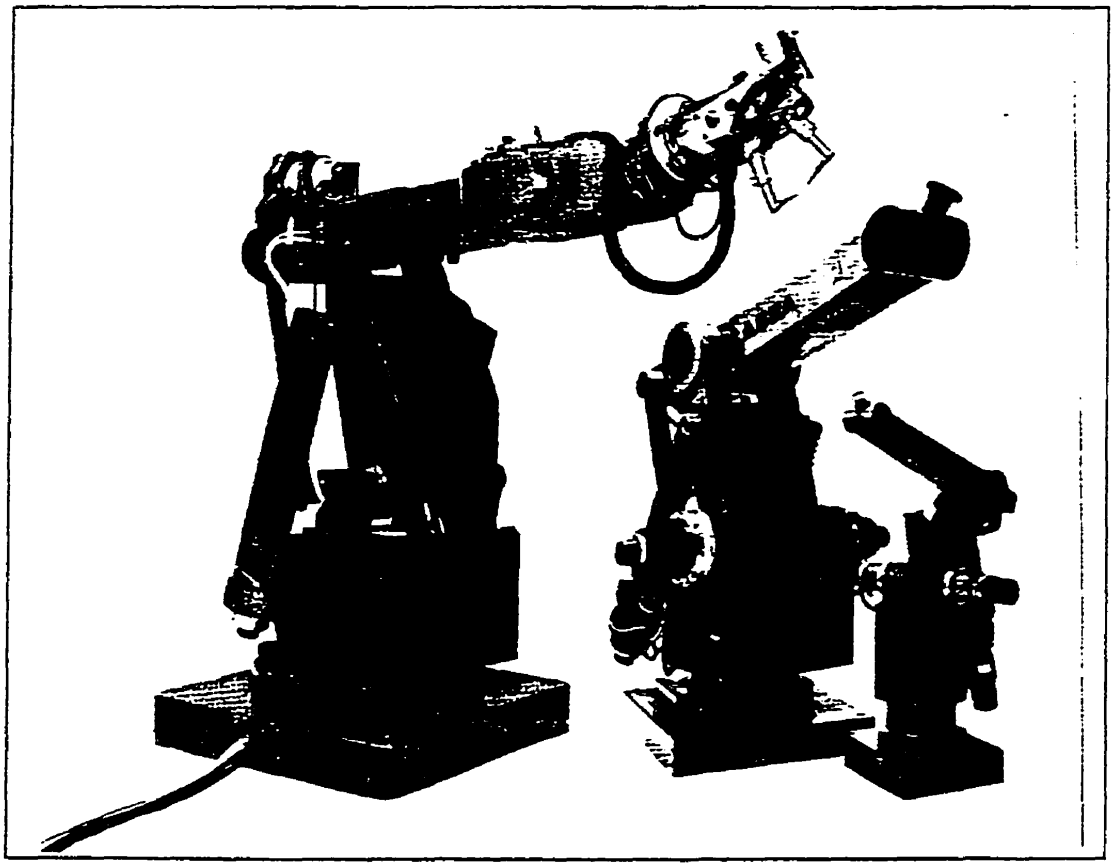

Figure 2.6: ASEA IRB 6/2

Advanced Automation Products produces the BASE Robot which is a Cartesian-coordinate arm coupled with a revolute gripper. Constructed of aluminum, stainless steel and bronze, the BASE Robots are actuated by a pneumatic pressure. At 80 psi (552 kPa), forces generated in the x-y-z directions vary from 55 to 90 pounds (25 to 41 kg) [26].

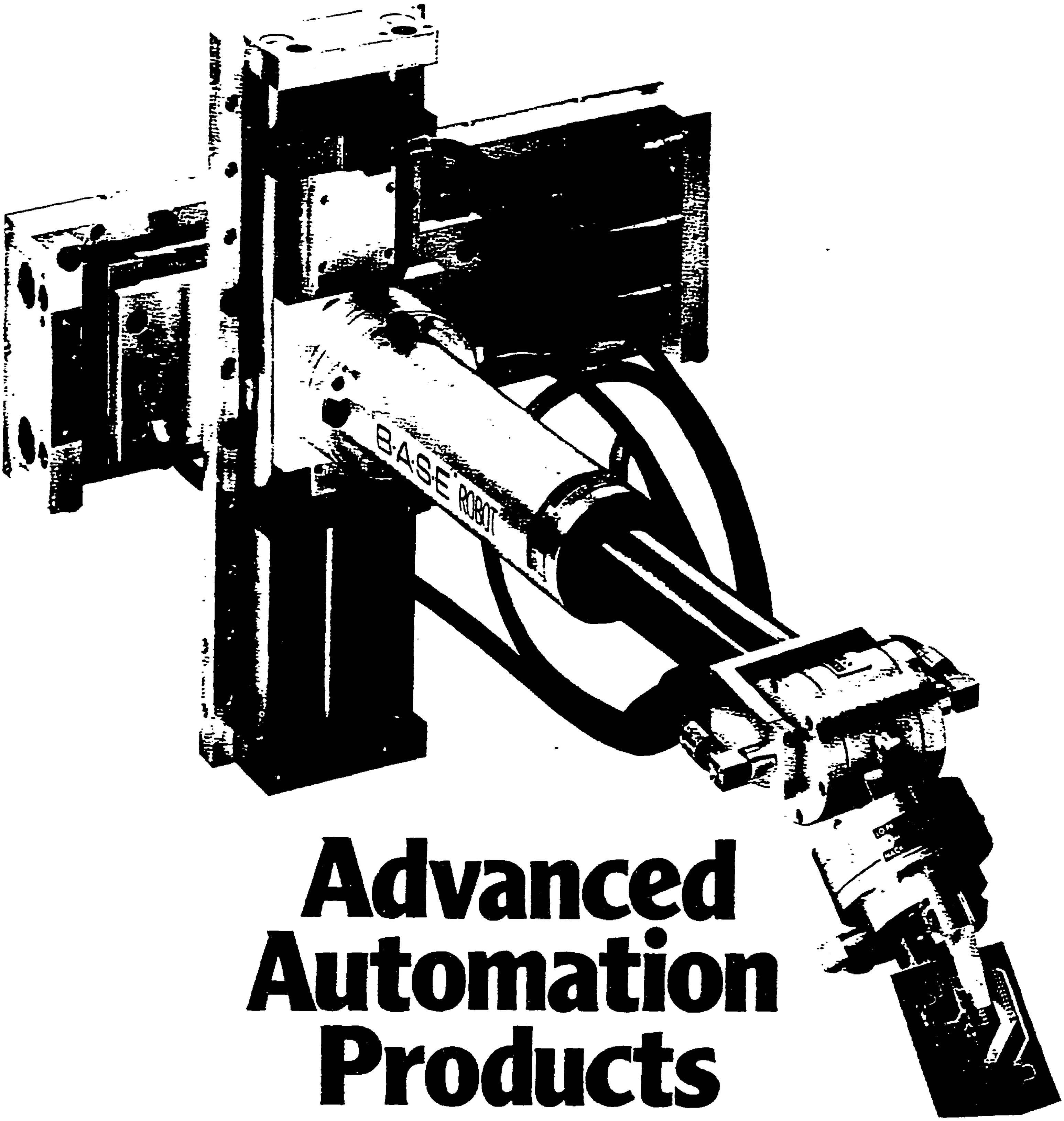

Figure 2.7: Advanced Automation Products BASE Robot

The Sarcos Dextrous Arm, one of which can be found at the McGill Center for Intelligent Machines, has ten degrees of freedom and operates at 3000 psi (20.7 MPa) of hydraulic pressure. The tele-operator of the Sarcos Dextrous Arm "wears" the master arm and by moving his human arm inside the master arm, the motion is replicated by the slave arm. The load cells in the Sarcos arm can sense forces as small as one ounce, permitting the operator to engage in delicate manipulations [27].

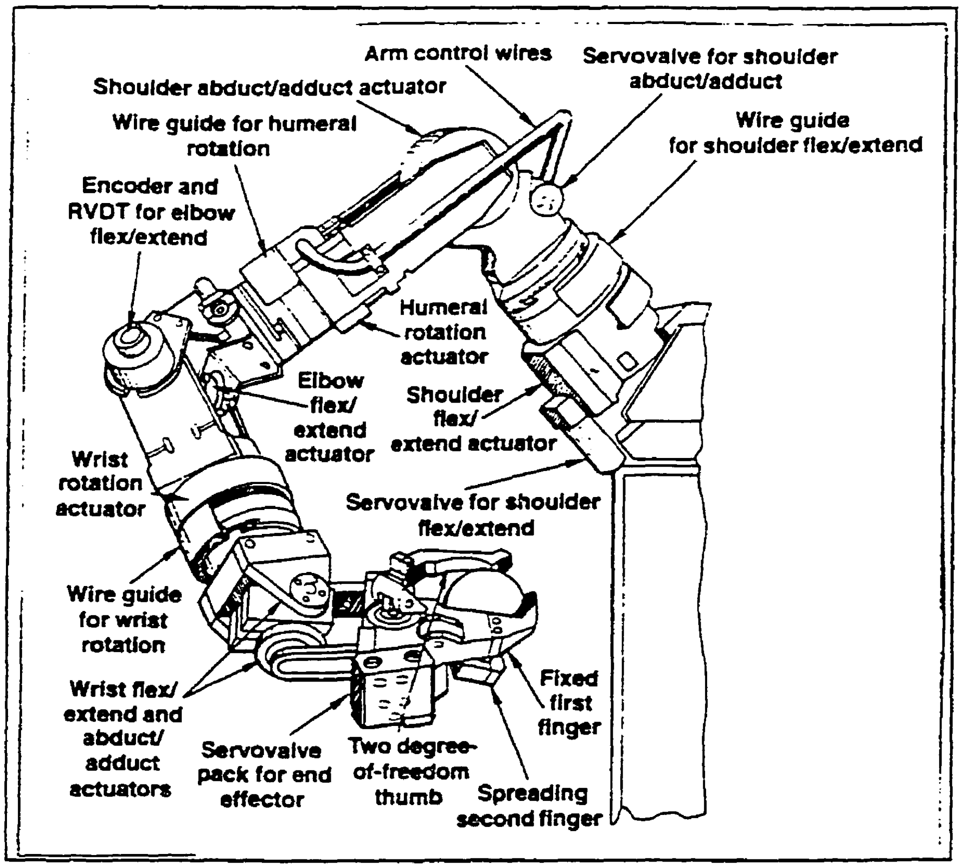

Figure 2.8: Sarcos Dextrous Arm

Spine Robotics of Sweden has developed a serpentine manipulator for industrial applications ranging from spray painting to arc welding. With its electro-hydraulic servos and seven degrees of freedom, it is a highly dextrous arm [28].

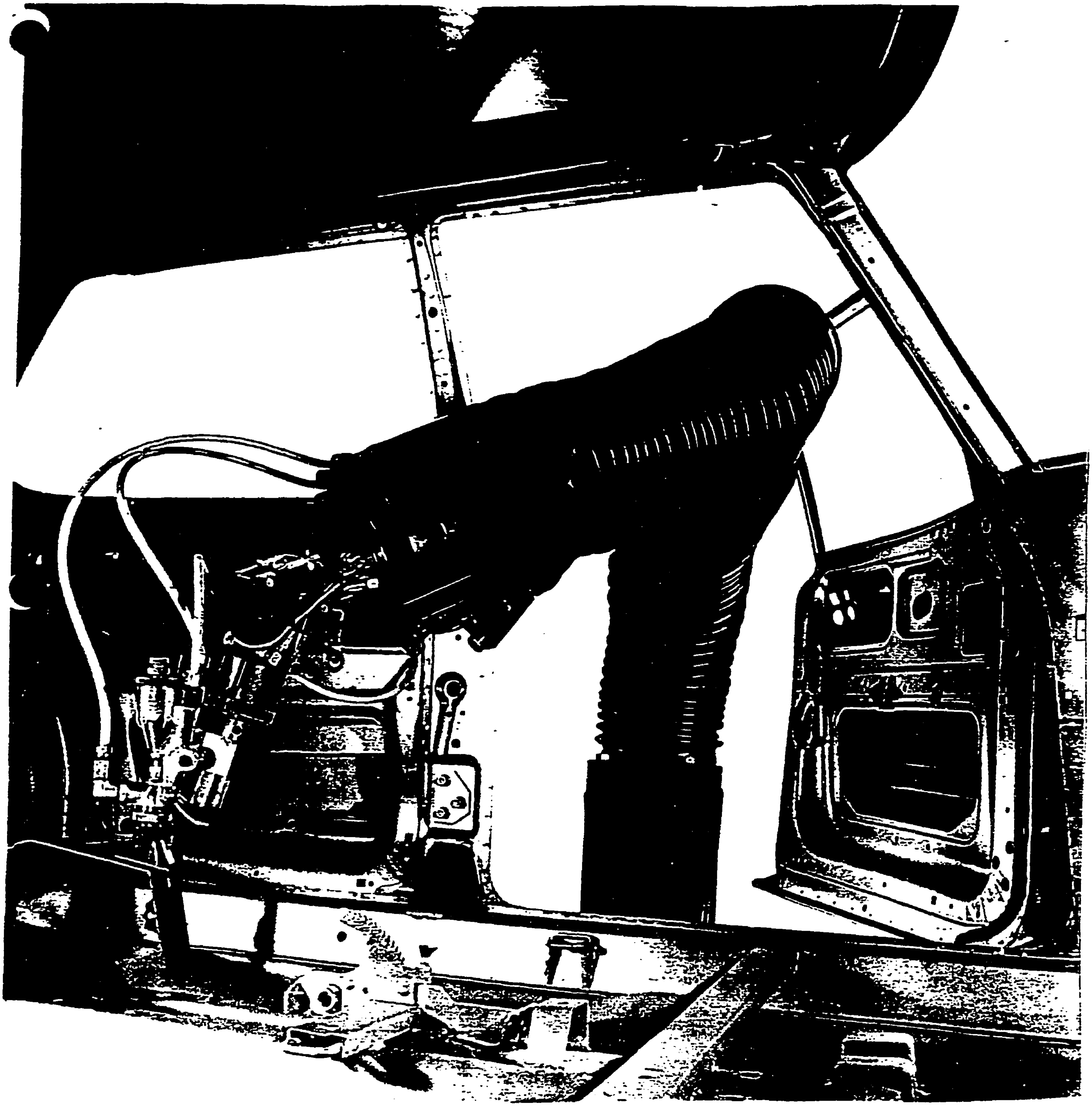

Figure 2.9: The Spine Robot spray painting the interior of a car body

Barrett Technology has developed a lightweight, highly dextrous, zero-backlash, seven-degree-of-freedom manipulator. The four DOF of the 7-pound (3.2 kg) aluminum and steel shoulder/elbow are powered by brushless DC electric motors and generate a force at the tip of 5 lbs (22 N). The 3-DOF wrist, constructed of magnesium and a carbon/Kevlar composite, weighs only 4 lbs (1.8 kg) yet generates pitch and roll torques of 42 in-lb (4.7 N-m). The multi-fingered Barrett Hand exhibits similarly impressive dexterity, with the capability of manipulating objects as large as 1 meter in diameter or as small as 1 centimeter [29].

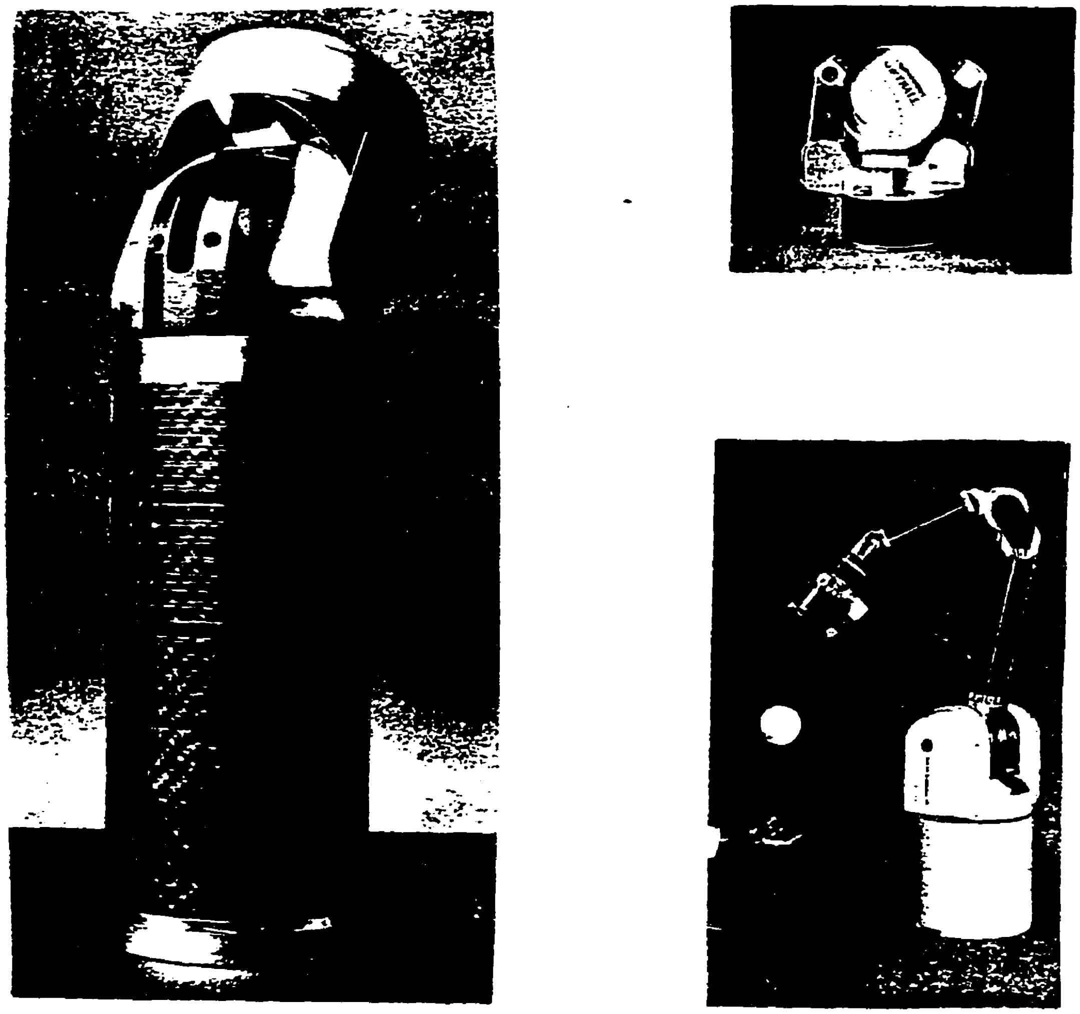

Figure 2.10: Barrett Wrist (left), Barrett Hand (top right) and Barrett Arm (bottom right)

Some fascinating innovations in anthrorobotics (the area of study concerned with robots of human-like form and function) have also come from Ross-Hime Designs. Possessing remarkable dexterity, the Omni-Hand and the Omni-Wrist are rugged enough to be used in everything from for nuclear material handling to underwater manipulators. Both are rated for a payload of 25 pounds (11.4 kg). The Omni-Wrist allows for 180° of pitch and yaw as well as 360° of continuous roll which makes it ideal for manipulating tools [30].

Popular examples of revolute coordinate manipulators are the Programmable Universal Manipulator for Assembly (PUMA) designed by Unimation [31], Cincinnati Milacron arms [32], and the Selective Compliance Assembly Robot Arm (SCARA), like the French Scemi [33]. There are also numerous anthropomorphic arms currently on the market: the Intelledex 660 [34], the ABB IRB 1000, Tetrabot, and the Martin Marietta Flight Telerobotic Servicer (FTS).

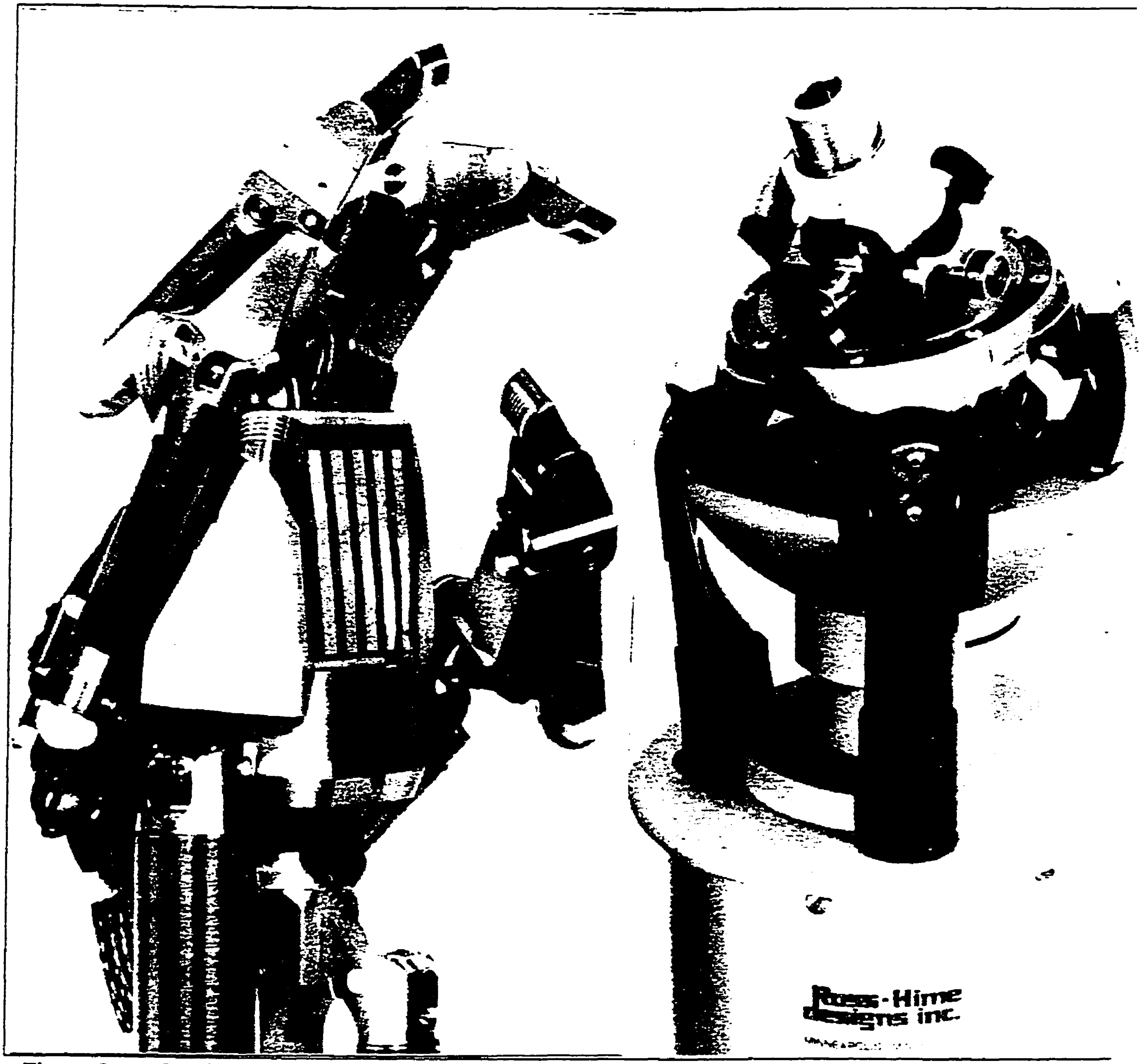

Figure 2.11: Omni-Hand (left) and Omni-Wrist (right) of Ross-Hime Designs, Inc.

2.2 Anatomy of an Anthropomorphic Arm

Essentially, an anthropomorphic robotic arm, such as Lightarm, consists of a shoulder, elbow, wrist and a hand or gripper as illustrated in the schematic below. These mechanisms are typically not mere prismatic or revolute joints but comprise gimbals, ball-and-sockets, universal joints and cams. These provide more fluid and dextrous motion, the better to emulate the kinematics of a human arm. To be truly anthropomorphic, the kinematics of an anthropomorphic arm should replicate those of its human counterpart in its full seven degrees-of-freedom. The shoulder should be able to achieve 270° of pitch, 180° of yaw and 90° of roll while the elbow should be able to achieve 150° of pitch. Finally, the wrist ought to produce singularity-free movement through 170° of pitch, 70° of yaw and 90° of roll. The addition of a hand or gripper provides yet more dexterity.

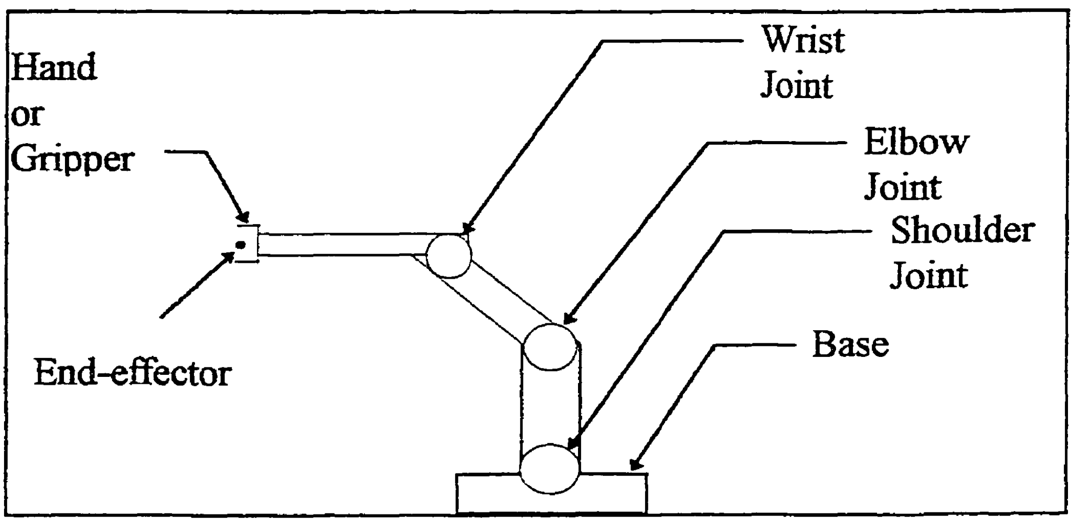

Figure 2.12: Anatomy of an Anthropomorphic Arm

2.3 Survey of Composite Robot Research

For at least a decade now, researchers have explored the application of lightweight materials such as graphite/epoxy to the design of robotic arms. As mentioned earlier, Gombert et al. at the Institute for Robotics and System Dynamics of the German Aerospace Research Establishment designed and built ROTEX, an ultra-light carbon-fiber grid structure manipulator having a payload-to-weight ratio of 1:1. At the Technion in Israel, Salomonski et al. [35] have designed a light manipulator with a 1:1 ratio of payload to weight based on an inflatable thin shell structure. Such an arm could be folded into a compact package, lofted into space and then deployed by inflating it with compressed air. Yet another lightweight space robot, dubbed the Self-Mobile Space Manipulator, has been developed by Yangsheng Xu et al. [36] at Carnegie Mellon. The 7-DOF arm is intended for inspection, maintenance and construction of the trusswork of Space Station Freedom. In South Korea, Dai Gil Lee et al. [37] have designed and built a SCARA-type direct-drive robot using graphite/epoxy. They have shown that, in addition to weight savings, the static deflection, natural frequency of vibration and damping ratio were superior in the composite arm compared to its aluminum predecessor. The same authors [38] later developed a carbon-fiber anthropomorphic arm which has 6 DOF, a 70 N payload and a positional accuracy of 0.1 mm. The composite arm weighed a quarter of its steel predecessor and exhibited a natural frequency double that of the steel arm. The optimal angle for the filament-winding of the graphite/epoxy was determined to be 15°. Finally, these same authors [39] also designed and fabricated the third arm of a 6-DOF articulated robotic manipulator with graphite/epoxy. The cylindrical structure is rated for a payload of 60 Newtons and can achieve a positional accuracy of 0.1 mm. Once again they observed that the composite arm exhibited superior damping and stiffness characteristics compared to the original aluminum prototype.

Thompson and Sung [40] have investigated the performance improvements achieved by replacing the steel forearm of a General Electric P50 industrial process robot with unidirectional or ±45° graphite/epoxy laminates. Their findings indicate that graphite/epoxy radically improves the damping and reduces the settling time. The damping ratios were calculated to be 0.2 at 500 Hz for the unidirectional and 1.1 at 500 Hz for the ±45°. Since the natural frequency of the graphite/epoxy forearm was estimated to be approximately 500 Hz higher than its steel counterpart, the composite forearm has a larger bandwidth and is thus easier to control. The same authors [41] have developed a mathematical methodology for optimizing the lay-ups of composite robotic arms, taking into account stiffness, strength, damping, and mass. Another laminate optimization technique for minimizing tip deflection of a robot link has been presented by Chao [42].

While some robotic arms move slowly enough that they may be considered quasi-static, others accelerate and decelerate rapidly and thus require full dynamic analysis. Gordaninejad et al. [43-46] have addressed this issue using Hamilton's Principle and Timoshenko beam theory to derive equations of motion of a laminated composite flexible robotic arm that take into account the effects of geometric nonlinearity, rotary inertia and shear deformation. In subsequent papers, they investigated the effects of fiber orientation, stacking sequence and damping on dynamic properties. Sung and Shyl [47] studied the dynamic response of a box-beam link of a robotic arm. A ply orientation of 36.8° optimized the specific damping capacity of the link. Caprino and Langella [48] optimized a robotic arm for maximum fundamental frequency using the Rayleigh-Ritz energy method to find an expression for the flexure of a beam.

Finally, the issue of controlling a flexible composite arm has been addressed in numerous papers. Ghazavi and Gordaninejad [49] used nonlinear controllers with PID compensators to control a graphite/epoxy arm. They observed the effect of the control system on the new lighter, stiffer composite structure and compared it with the previous dynamic performance of the aluminum arm. The relative advantages of active and passive control were examined by Gordaninejad and Vaidyaraman [50] with an eye to reducing end-effector vibration and settling time. Lastly, Choi et al. [51] investigated the vibration attenuation of a composite robotic arm using a non-linear state feedback controller.

2.4 Survey of Materials

The following table provides a summary of various high-performance engineering materials that were considered for critical components of the Lightarm manipulator. Of particular interest were materials with high stiffness-to-weight ratio (i.e. specific stiffness) and high strength-to-weight ratio (i.e. specific strength). The anisotropic nature of graphite/epoxy is evident in the radical difference in the strength and stiffness in the fiber direction vis-à-vis the matrix direction. In the fiber direction, graphite/epoxy exhibits vastly superior specific stiffness and specific strength than do the metals. In the matrix direction, however, graphite/epoxy has relatively poor specific stiffness and specific strength. Thus, to design a graphite/epoxy structure requires carefully tailoring the orientation of each constituent ply to provide aggregate strength and stiffness properties that are optimized for the loads and the geometry of the structure.

Material	Density [kg/m^3]	Young's Modulus [GPa]	Specific Stiffness [MNm/kg]	Tensile Strength [MPa]	Specific Strength [kNm/kg]
Aluminum 6061-T6	2710	70	26	260[1] *(240)*[2]	96 *(89)*
Aluminum 7075-T6	2800	72	26	570 *(500)*	204 *(179)*
Titanium 6AL-4V	4730	115	24	900 *(830)*	190 *(176)*
Steel AISI 4340 Q&T 350 °C	7860	207	26	1720 *(1590)*	219 *(202)*
Stainless Steel Type 440C Tempered 315 °C	7800	200	26	1970 *(1900)*	253 *(244)*
E-glass/epoxy (fiberglass)	1800	39	21	1062	590
Graphite/epoxy T300/N5208 (fiber direction)	1600	181	113	1500	**938**
Graphite/epoxy T300/N5208 (matrix direction)	1600	10	7	40	26
Graphite/epoxy LTM25 (fiber direction)	1547	126	82	1724	**1114**

Table 2.1: Mechanical Properties of Some High-Performance Engineering Materials
[1]ultimate
[2]*yield*

Although the mechanical properties tabulated above were considered paramount, they were not the sole factors in the material selection for the various components of Lightarm. Cost, manufacturability, wear and corrosion were also determining factors. For instance, although titanium has excellent strength and corrosion properties, it is not only costly per unit weight but it is also difficult to machine which, in turn, translates into a high manufacturing cost per part. Aluminum is considered a soft metal and, as such, is easy to machine. The downside of that is, of course, that aluminum wears rapidly in contact with harder metals such as steel. Of all the tabulated materials, graphite/epoxy is by far the most difficult to machine. Machining operations such drilling, tapping, sawing and milling are difficult with conventional High-Speed Steel (HSS) tools due to the intrinsic hardness of the graphite fibers. Tungsten carbide-tipped or diamond-encrusted tools are necessary to cut graphite/epoxy without inducing delamination, fraying or splintering between the plies. In summation, for the Lightarm manipulator, the optimal materials were stainless steel, aluminum and graphite/epoxy. Dynamically, the mass of the shoulder mechanism contributes very little to the overall inertia of the arm. Thus, stainless steel proved to be ideal for the shoulder where high strength, machinability, low wear and corrosion-resistance were of paramount importance. Unlike the shoulder, the mass of the upper arm creates significant inertia. Therefore, the high strength-to-weight ratio of graphite/epoxy was optimal for the main upper arm structure while aluminum, being light and easy to machine, proved to be ideal for the numerous smaller components that comprise the elbow mechanism and the forearm.

Chapter 3

The Shoulder Joint

3.1 Kinematics of Lightarm

The Lightarm manipulator has seven degrees of freedom. The shoulder mechanism has three degrees of freedom, the elbow one and the wrist three. The arm is effectively a hybrid serial/parallel mechanism. The wrist, elbow and shoulder joints are serial with respect to each other, meaning that each joint operates independently of the others. But the joints themselves are parallel mechanisms. In a parallel mechanism, there are two "platforms" linked by two or more actuators working concurrently. For instance, in the shoulder mechanism, illustrated in Figure 3.1, the H-Base and the SRC Flange are the two "platforms" which are linked by the shoulder's four parallel actuators. Serial actuation has certain inherent shortcomings, such as lack of structural rigidity, low natural frequency as well as accumulation of positional error. Not only does parallel actuation not suffer from these three problems but, in addition, parallel actuation allows for high bandwidth and workspace augmentation as well as backlash elimination through the use of actuator redundancy [52]. By arranging the three parallel mechanisms (shoulder, elbow and wrist) in series like in a human arm, the advantages of both serial and parallel actuation can be exploited to maximize the performance of Lightarm.

From a kinematic standpoint, the shoulder is a *combinatorial* mechanism in which its four actuators work in parallel. In current robotics jargon, such an arrangement is termed "actuator-redundant" although this nomenclature is slightly misleading because in fact no actuator is truly redundant and all contribute to the motion of the shoulder. The term redundant arises from the fact that, in the event that one of the four actuators fails, the shoulder will continue to function, albeit with a greatly diminished workspace.

Moreover, actuator-redundancy enlarges the workspace, eliminates singularities and improves the overall structural rigidity of the mechanism [53-55].

The shoulder is capable of producing an acceleration of 130 m/s^2 at the wrist joint. The maximum velocity at the wrist was measured to be 0.45 m/s. The theoretical singularity-free workspace of the shoulder mechanism was calculated (assuming all parts have zero thickness) to be 180° of tilt in both directions and 270° of swivel. The first prototype achieved roughly 90° of tilt in both directions and 180° of swivel.

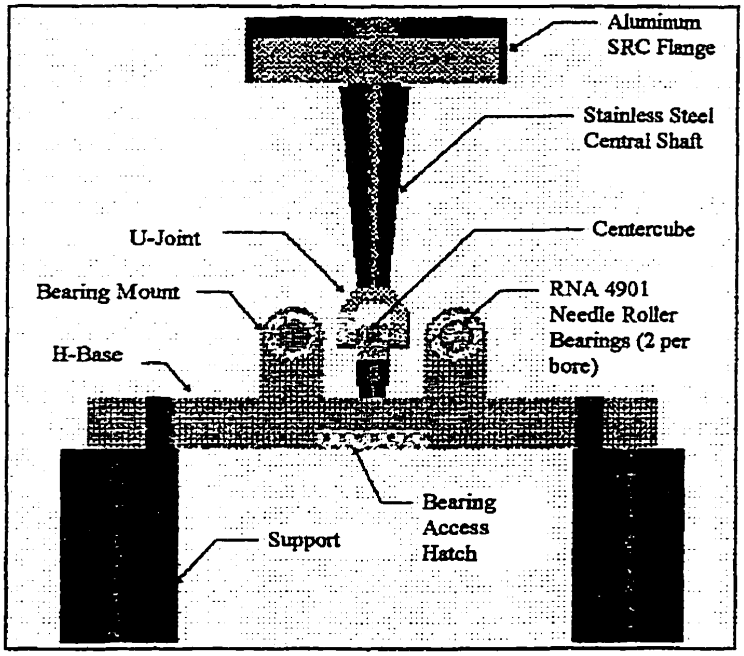

Figure 3.1: Shoulder Joint Nomenclature

3.2 Redesign of the Shoulder Mechanism

The initial shoulder prototype was designed and built by the Sarcos Research Company of Utah. Essentially, the design was successful. The shoulder develops a surprising 200 Nm of torque around all three axes over a bandwidth of 100 Hz and the moving mass of the shoulder is only approximately 1 kg. Despite this remarkable performance, however, there were two problems with the design. First of all, the base was too narrow and consequently not particularly conducive for attachment to a boom or vehicle. From a stability point of view, it is preferable for the points of attachment to be spread further apart in order to diminish the moment applied to the boom or vehicle as the arm manipulates a heavy payload. Thus, a new H-Base (so termed for its shape when viewed from above) was designed to meet this requirement. Retaining the key dimensions and kinematic parameters of its Sarcos predecessor, the H-Base is more easily adapted to mobile bases and booms. Constructed of Stainless Steel Type 304, the H-Base, shown in Figure 3.2, houses the shoulder's four actuators which power the shoulder mechanism.

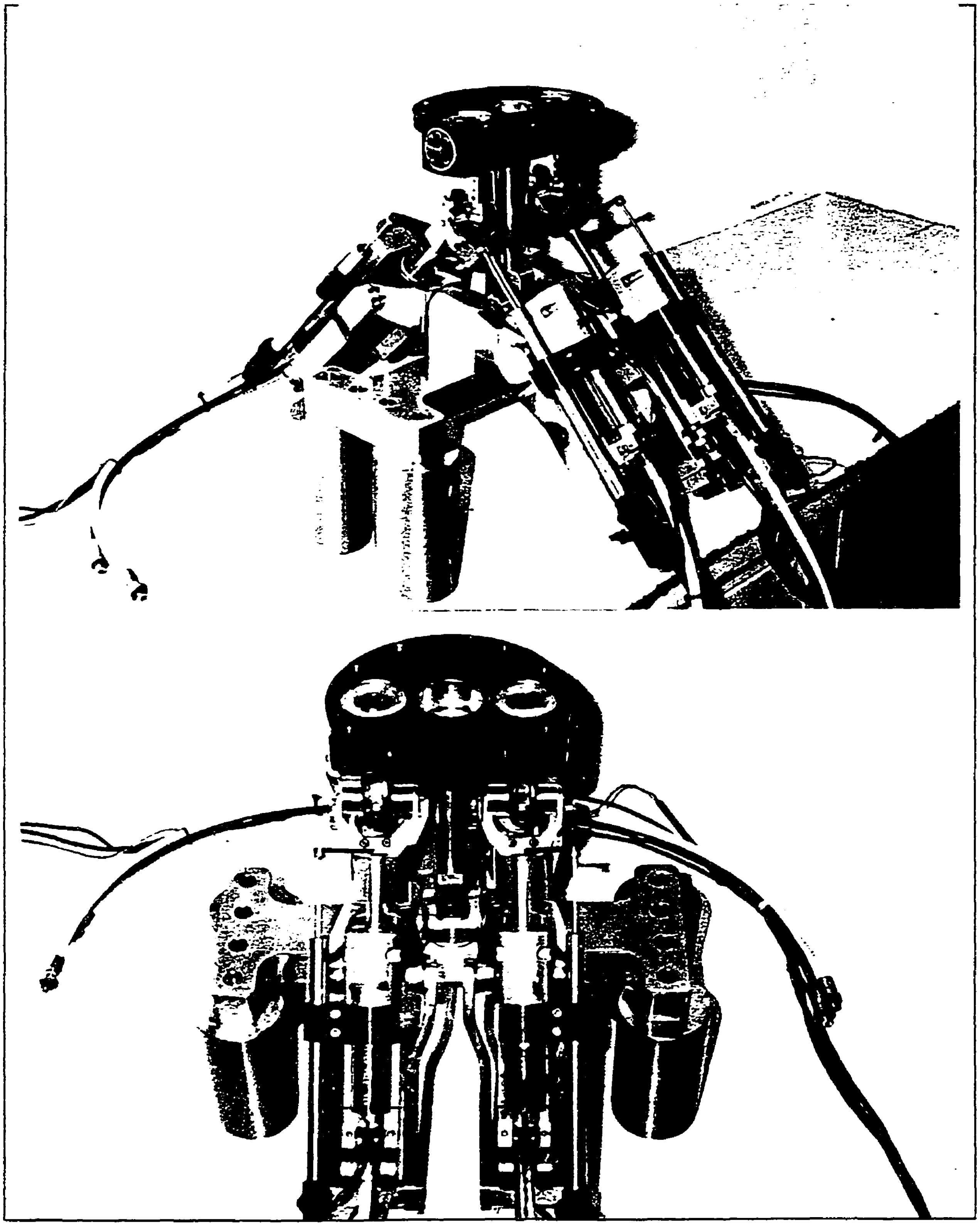

Figure 3.2: Redesigned Shoulder Joint

The Animate Systems hydraulic actuators run at a mere 500 psi (3.45 MPa) which is a substantially lower and safer pressure than the 3000 psi (20.7 MPa) most commonly found in industrial robot hydraulics. Despite the low operating pressure, each actuator is capable of developing 300 pounds force (1340 Newtons) while displacing the piston at up to 10.2 cm/s. The mass of each actuator is 612 grams. With a damping factor of 0.14, the actuators create a beneficial hydraulic damping effect in each of the joints of the robotic arm. The natural frequency of each actuator is 394 Hz which makes control feasible. Each actuator is equipped with Teflon-sealed pistons and is piggy-backed with its own suspension electromagnetic jet pipe valve and an LVDT position transducer which tracks the piston throughout its 7.2-cm stroke. The black horseshoe-shaped object at the end of each actuator is a Hall Effect force transducer. Parenthetically, two identical actuators drive the elbow mechanism [56-62].

Following the completion of the Sarcos shoulder prototype, tests conducted to gauge the dynamic and kinematic characteristics of the new mechanism resulted in a broken central shaft. Consequently, a much stronger central shaft was needed. At the same time, it became apparent that the actual workspace of the shoulder was not even close to what was theoretically possible. Thus, the challenge was to design a central shaft and universal joint that not only enlarged the workspace volume of the shoulder mechanism, but also improved its strength and robustness.

In order to maximize the workspace volume of the shoulder mechanism, the gap between the bearing mounts of the H-Base, Δ (shown in the figure below) had to be as large as possible. However, from a kinematic standpoint, it would not suffice to, say, spread the bearing mounts further apart because this would only reduce the lateral workspace of the shoulder. The distance, D, between the bearing centers had already been optimized by graphical techniques and by constructing a wood and Lucite model. Thus, a finite-element model was used to determine the minimum wall thickness, t, that would safely withstand the loading of the actuators. Although it ultimately didn't prove to be a consideration, it should be noted here that the minimum wall thickness is also governed by the practicalities of machining. To accurately bore a hole to the tolerances required for the needle roller bearings, a minimum wall thickness is required or else the cutting force of the boring bar or reamer will cause the metal to deflect locally thereby ruining the cylindricity of the hole. The second design criterion was, of course, to ensure that the deflection of the H-Base was as minuscule as possible so as to make control of the moving links computationally simpler.

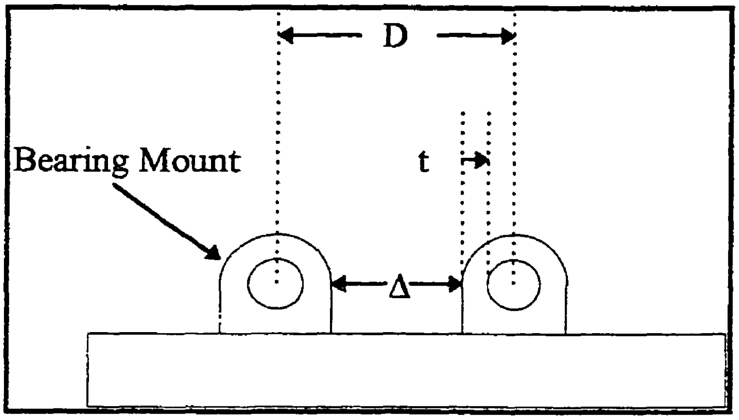

Figure 3.3: Kinematic Parameters of the Shoulder

A finite-element model was constructed using 8-node solid brick, 6-node solid pie-slice and 4-node thin-shell elements. The thin-shell elements were used to model the bearing mounts so that the wall thickness could be varied. The results of the seven iterations are presented in Table 3.1. From the finite-element modeling, when the wall thickness falls below 2.0 mm, the highest Von Mises stress is located on the thin wall of the bearing mounts. When the wall thickness equals or exceeds 2.0 mm, the highest Von Mises stress is no longer located on the thin wall of the bearing mount. Rather, the highest stress migrates to a point on the horizontal extension of the H-Base, as illustrated in the figure below. It is manifest from the foregoing table that the Von Mises stress becomes asymptotic at 212 MPa and that the optimal wall thickness for the bearing mounts of the H-Base is 2.0 mm, a thickness beyond which the Von Mises stress remains effectively constant.

Wall Thickness, t (mm)	Maximum Displacement (mm)	Maximum Von Mises Stress (MPa)
0.5	0.198	1370
1.0	0.123	433
1.25	0.118	305
1.5	0.115	229
2.0	0.112	212
2.5	0.111	212
3.0	0.110	212

Table 3.1: Finite-Element Analysis Iterations for Wall Thickness of Bearing Mounts

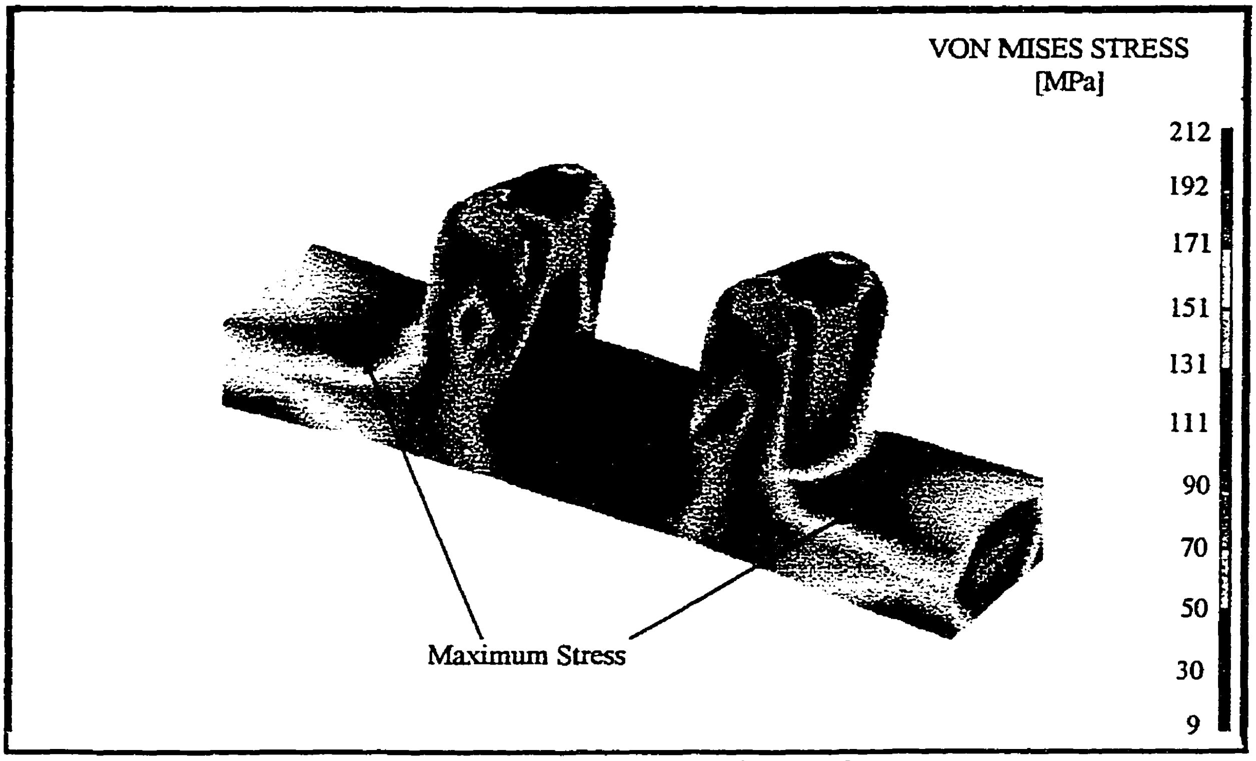

Figure 3.4: Stress Contours in H-Base for a Wall Thickness of 2.0 mm

3.3 Design of Universal Joint

At the kinematic center of the shoulder mechanism is a universal joint whose small size is critical in the performance of the shoulder. Once again, to ensure that the shoulder joint enjoys a large range of motion, the universal joint had to be as small as possible, yet be able to withstand the large loads imposed upon it by the four actuators. All the components of the U-joint are Stainless Steel Type 303 which has high strength, corrosion-resistance and contains a trace of Sulphur which makes it easier to machine than the other 300-series stainless steels. The HK0408 TN drawn cup needle roller bearings determine the minimum dimensions of the universal joint since they are the smallest bearings capable of safely taking the loads imposed upon them by the four actuators. The inside of the forks of the U-joint have been rounded in order to provide smoother motion. In order to prevent the prongs of the "centercube" from sliding through the needle roller bearings, four conical black Delrin spacers were machined to mate with the conical section of the centercube. These items are visible in Figure 3.5.

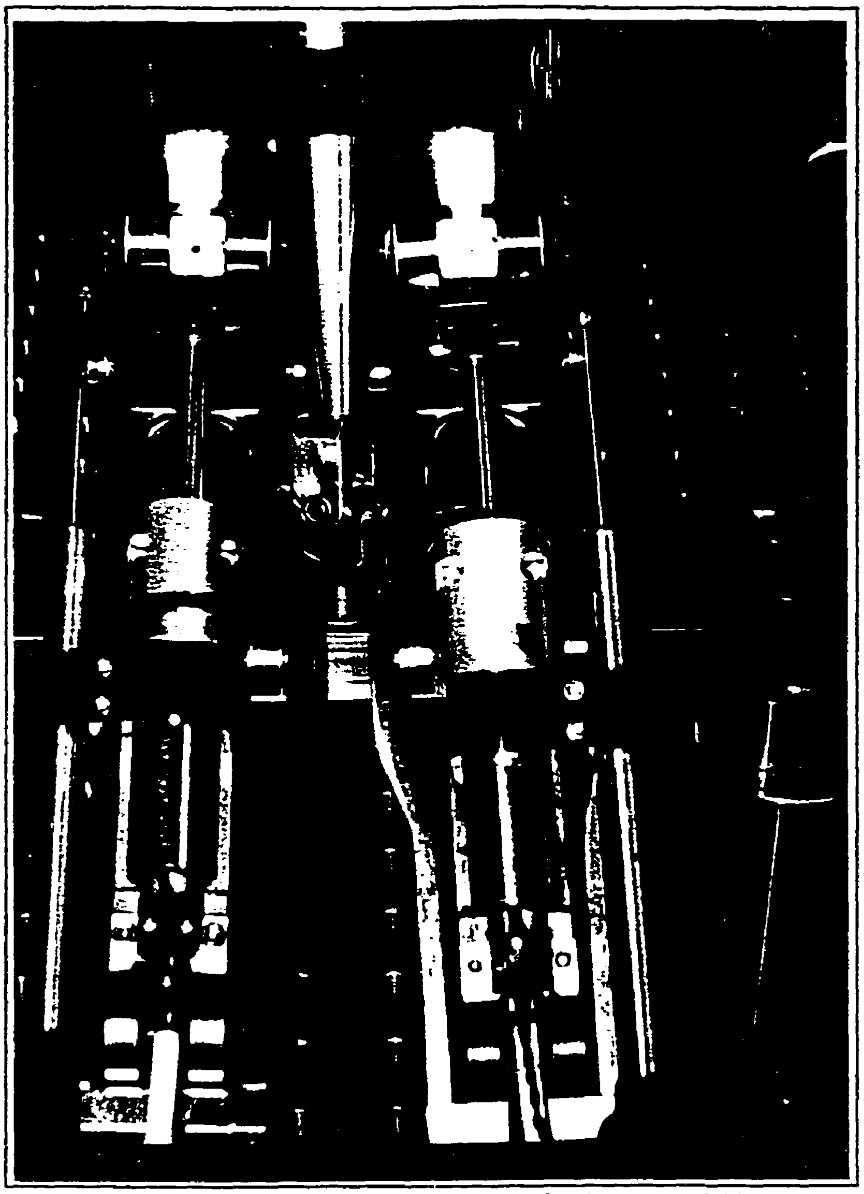

Figure 3.5: Universal Joint at Kinematic Center of Shoulder

3.4 Stress Analysis of Centercube

The four-pronged "centercube" is shown in plan view in Figure 3.6. The part has two planes of symmetry which are exploited to reduce the scope of the finite-element model.

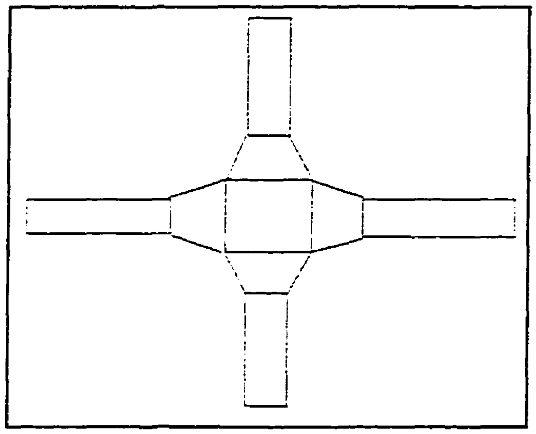

Figure 3.6: Plan View of Centercube

Built of high yield strength precipitation-hardened (PH) stainless steel, this component withstands stresses of 183 MPa as illustrated in Figure 3.7. The worst-case loading of the centercube would occur if the controller mistakenly drove both pairs of actuators antagonistically. Since each pair of actuators operates at roughly 90° to the opposite pair, the total force generated in the vertical plane is:

$$F = 2\sqrt{2}(1340\,N) = 3790\,N \tag{3.1}$$

This load is then divided between the central shaft and the two actuator output linkages. Therefore, only one-third of the total load is felt by the centercube, of which only a quarter of that (or one twelfth of the total) is felt by each prong. A finite-element model of one such prong was constructed using 8-node solid brick elements and 6-node solid pie-slice elements. Assuming a yield strength of 350 MPa, the factor of safety for the centercube is 1.9. It should be recalled that this loading only occurs if all the actuators are mistakenly driven antagonistically. In proper usage, the centercube is not subjected to such loads. In fact, under normal operating conditions, the load on the centercube is merely the centrifugal force due to the rotation of the arm about the universal joint. This centrifugal force is practically negligible due to the low angular velocity of the arm about the universal joint.

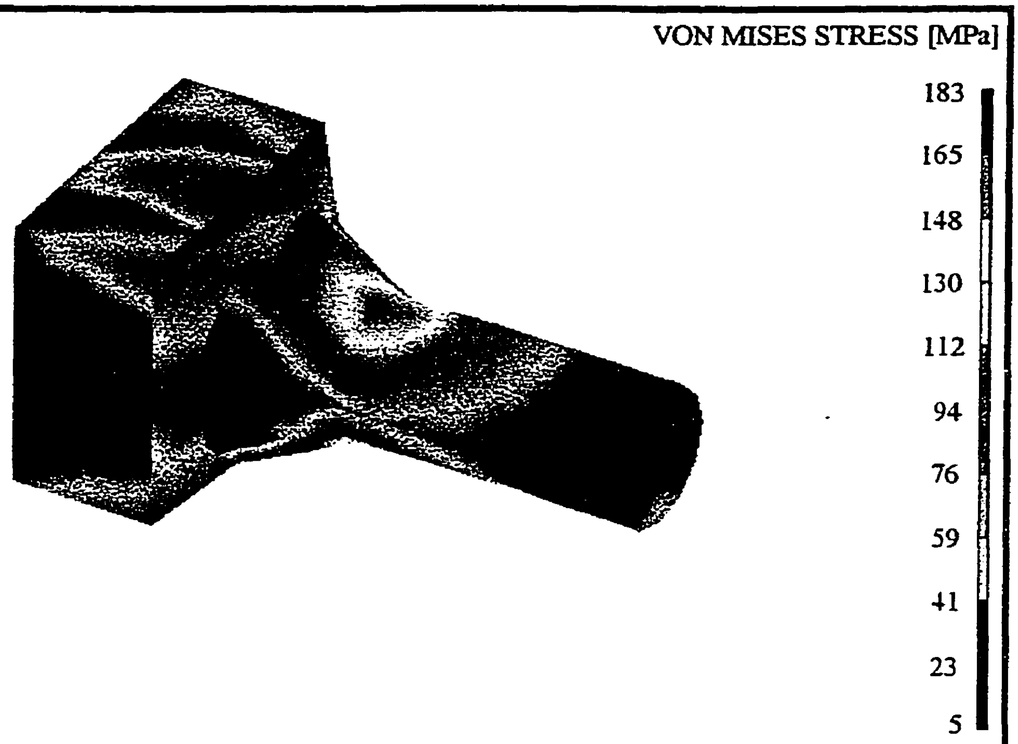

Figure 3.7: Stress contours on one of the four prongs of the centercube

By minimizing the dimensions of both the universal joint and the wall thickness of the H-Base, the shoulder joint now exhibits an excellent range of motion as illustrated in Figure 3.8.

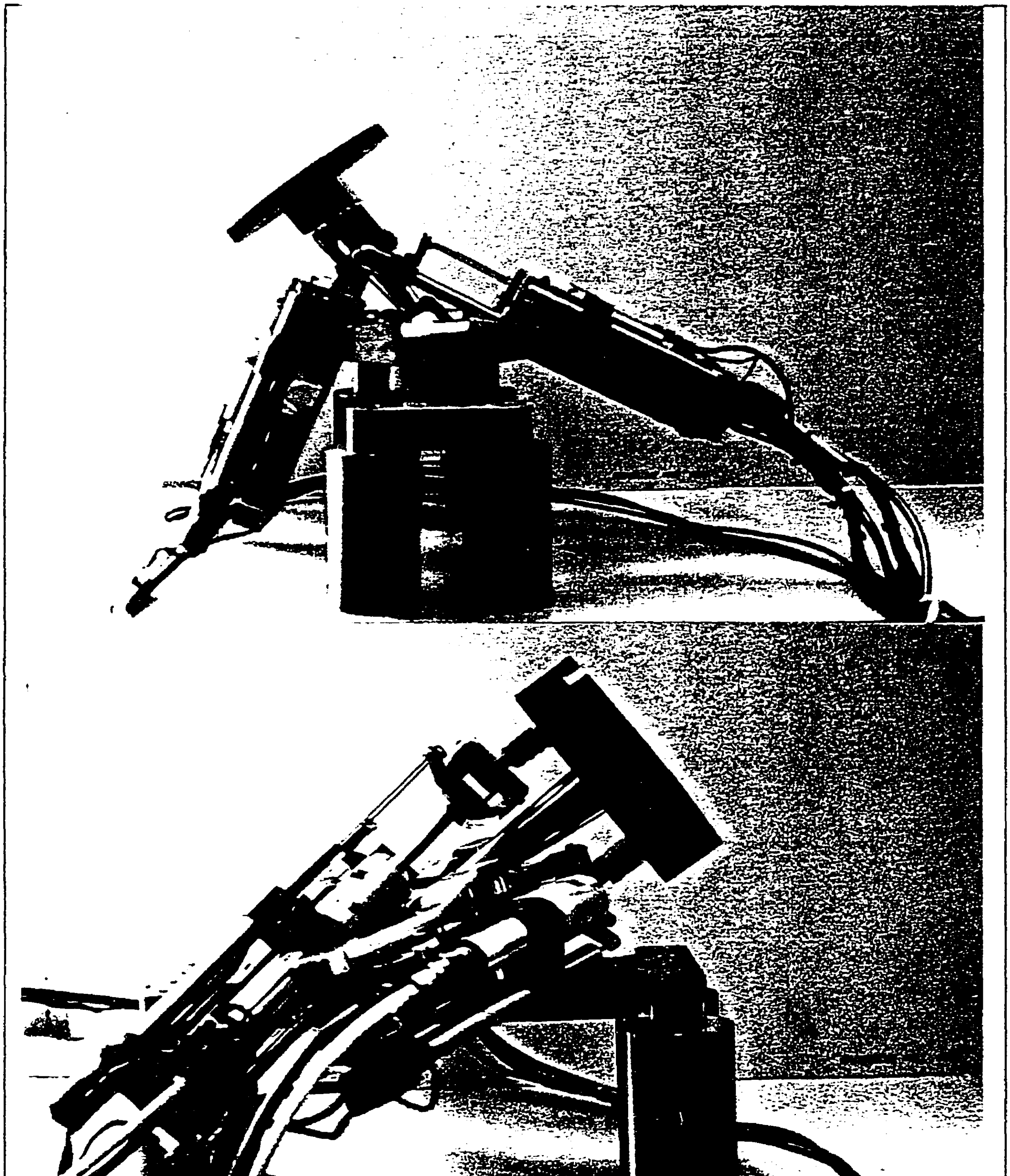

Figure 3.8: Range of Motion of Shoulder Joint

Chapter 4

The Elbow Joint

4.1 Design of the Elbow Mechanism

Whereas the weight of the shoulder mechanism was not all that critical, the weight of the elbow mechanism contributes very significantly to the overall inertia of the manipulator. Thus, the driving factor in the design of the various components of the elbow mechanism was strength-to-weight ratio. There are essentially two critical components that require extensive analysis: the main actuator shafts and the box-beam that houses the elbow mechanism. But before proceeding to the finite-element analysis iterations, it was first necessary to determine the loads that act on these components.

4.2 Force Analysis

As a worst-case loading scenario, one can imagine the arm attempting to lift an impossibly large mass. In such a case, the gripper (or end-effector) of the arm is constrained and the arm bends under the load of the shoulder's four actuators. Thus, to compute the worst-case loads acting on the box-beam, we sum vectorially the actuator forces. For the principal (strongest) direction, we get a force of 3790 Newtons.

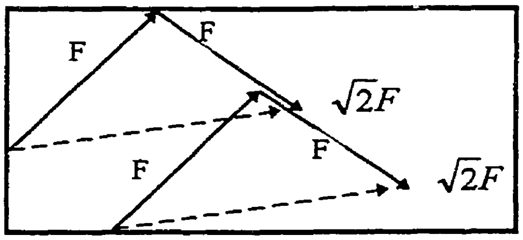

Figure 4.1: Vector Force Analysis

$$Total\ Force = 2\sqrt{2}F = 3790\ N \tag{4.1}$$

For the weak direction, the load can be calculated by calculating the moment produced when each pair of actuators acts antagonistically, as illustrated in Figure 4.2.

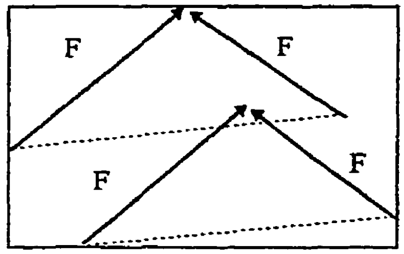

Figure 4.2: Vector Force Analysis for Weak Direction

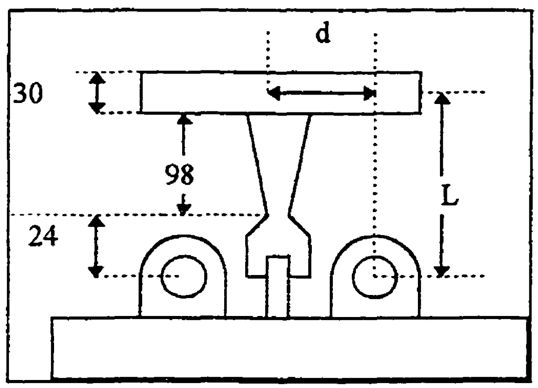

Figure 4.3: Key Dimension of Shoulder

$$d = 37.5\ \text{mm} \tag{4.2}$$

$$L = \frac{30}{2} + 98 + 24 = 137mm \tag{4.3}$$

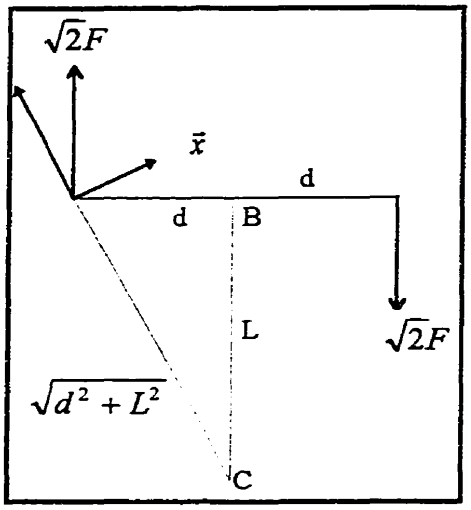

Figure 4.4: Vector Moment Analysis

$$\frac{\sqrt{2}F}{\|\vec{x}\|}=\frac{\sqrt{d^2+L^2}}{d} \tag{4.4}$$

$$\therefore \|\vec{x}\|=\frac{\sqrt{2}Fd}{\sqrt{d^2+L^2}} \tag{4.5}$$

$$T_C=2\|\vec{x}\|\sqrt{d^2+L^2} \tag{4.6}$$

$$\therefore T_C=2\sqrt{2}Fd \tag{4.7}$$

Therefore, the equivalent load at point B that would produce this torque is:

$$F_B=\frac{T_C}{L}=\frac{2\sqrt{2}Fd}{L}=\frac{2\sqrt{2}(1340N)(37.5mm)}{(137mm)}=1037N \tag{4.8}$$

In summary, the loads acting on the box-beam of the elbow mechanism are shown in Figure 4.5:

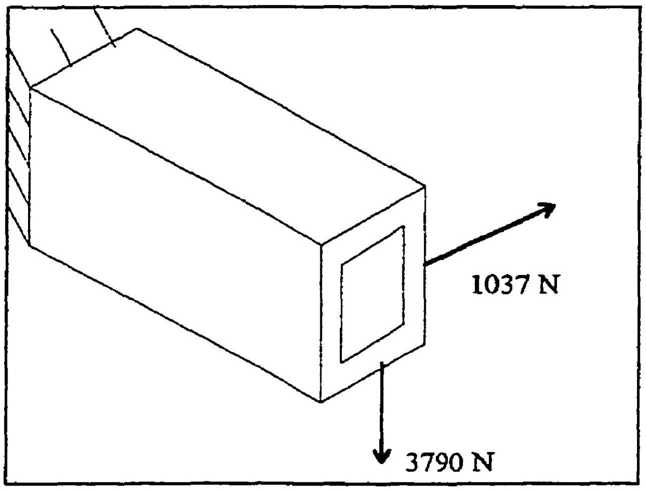

Figure 4.5: Forces Acting on Elbow Box-Beam

4.3 Design of Composite Box-Beam

The anatomical analog of this box-beam is an insect's exoskeleton. The box-beam houses and protects the upper arm's actuators which act antagonistically similarly to the biceps and triceps of a human arm. A material with high specific strength and high specific stiffness was sought to ensure that the box-beam is both rigid and strong yet light enough to ensure that the inertia of the arm is kept to a minimum. The graphite/epoxy composite used for this component was an Advanced Composites Group LTM25 prepreg with the following properties [63]:

E_X	126.2 GPa
E_Y	10 GPa
E_S	2.1 GPa
X_T	1724 MPa
X_C	1055 MPa
Y_T	40 MPa
Y_C	246 MPa
S	93 MPa
ρ	1547 Kg/m^3

Table 4.1: Mechanical Properties of LTM25 Graphite/epoxy

4.4 Finite Element Analysis

Using I-DEAS Master Series 2.1, a finite element model consisting of 1470 thin-shell elements was solved for a variety of lay-ups. Optimization was performed using an intuitive trial-and-error approach. The optimal lay-up was an 8-ply laminate, $[0_2/45/-45]$s, which provided a worst-case factor of safety of 1.7 in matrix tension in the two -45° layers. The addition of the 1 mm thick stainless steel end-fitting improved the factor of safety in matrix tension in the two -45° layers from 1.2 to 1.7. The $[0_3/90]$s laminate was second-best with a factor of safety of 1.4 in matrix tension in the two 90° plies. It is interesting to note the shear-strengthening effect of the 45° plies; while the $[0_2/45/-45]$s laminate had a minimum factor of safety of 3.2 in shear, the $[0_3/90]$s had a uniform safety factor in shear of only 2.0. Lastly, the angle-plies fared unexpectedly poorly. Neither the $[(\pm 30)_2]$s laminate nor the $[(\pm 15)_2]$s laminate was able to withstand the loads. The stresses in matrix tension in numerous plies were greater than its strength. Although the $[(\pm 15)_2]$s lay-up was used with success by Dai Gil Lee et al. [38], it did not prove to be very effective in this application largely due to the fact that the largest stresses were not due to bending but rather due to the loads on the holes. For withstanding this particular combination of loading, a laminate composed of 0° and ±45° plies provides the highest minimum factor of safety, as shown in Tables 4.2 to 4.8.

PLY	θ	X_T	X_C	Y_T	Y_C	S
1	0	7.2	6.0	2.1	15.8	10.0
2	0	7.2	6.0	2.1	15.8	10.0
3	45	3.8	7.1	2.3	14.1	4.3
4	-45	13.6	5.6	**1.2**	12.2	3.6
5	-45	13.6	5.6	**1.2**	6.8	3.4
6	45	3.8	7.1	2.2	14.1	4.0
7	0	7.2	5.7	2.1	15.8	10.0
8	0	7.2	5.7	1.3	4.6	5.3

Table 4.2: Factors of Safety using Maximum Stress Criterion for $[0_2/45/-45]$s with ¼ inch core without stainless steel end-fitting

PLY	θ	X_T	X_C	Y_T	Y_C	S
1	0	7.3	6.2	2.7	21.4	4.5
2	0	7.3	6.2	2.7	21.4	4.5
3	45	3.9	7.0	2.0	19.5	3.8
4	-45	13.4	5.5	**1.7**	10.8	3.2
5	-45	13.5	5.5	**1.7**	11.9	3.6
6	45	3.9	6.8	2.0	19.5	3.7
7	0	7.3	5.8	2.7	21.4	4.5
8	0	7.3	5.8	2.7	21.4	4.5

Table 4.3: Factors of Safety using Maximum Stress Criterion for $[0_2/45/-45]s$ with ¼ inch core and stainless steel end-fitting

PLY	θ	X_T	X_C	Y_T	Y_C	S
1	0	5.0	5.6	3.4	15.3	2.0
2	0	5.0	5.7	3.4	15.3	2.0
3	0	5.0	5.8	3.4	15.3	2.0
4	90	19.0	6.1	**1.4**	16.6	2.0
5	90	19.0	6.1	**1.4**	15.5	2.0
6	0	5.0	6.4	3.4	15.3	2.0
7	0	5.0	6.4	3.4	15.3	2.0
8	0	5.0	6.4	3.4	15.3	2.0

Table 4.4: Factors of Safety using Maximum Stress Criterion for $[0_3/90]s$ with ¼ inch core and stainless steel end-fitting

PLY	θ	X_T	X_C	Y_T	Y_C	S
1	30	4.1	5.0	**0.5**	4.1	0.9
2	-30	7.0	3.7	0.7	3.4	0.9
3	30	4.1	5.2	0.6	3.8	0.9
4	-30	7.0	3.9	0.6	3.6	0.9
5	-30	7.0	6.4	0.7	3.3	0.8
6	30	4.1	7.1	0.6	4.3	0.9
7	-30	7.0	6.5	0.7	3.2	0.8
8	30	4.1	7.0	**0.5**	4.6	0.8

Table 4.5: Factors of Safety using Maximum Stress Criterion for $[(\pm30)_2]s$ with ¼ inch core and stainless steel end-fitting

PLY	θ	X_T	X_C	Y_T	Y_C	S
1	15	4.0	9.0	1.8	9.2	2.3
2	-15	7.4	6.6	0.8	9.5	2.2
3	15	4.0	8.9	1.8	9.2	2.3
4	-15	7.4	6.7	**0.8**	9.5	2.2
5	-15	7.4	6.7	**0.8**	9.5	2.2
6	15	4.0	7.7	1.8	9.2	2.3
7	-15	7.4	6.6	0.8	9.5	2.2
8	15	4.0	7.6	1.8	9.2	2.3

Table 4.6: Factors of Safety using Maximum Stress Criterion for $[(\pm15)_2]_s$ with ¼ inch core and stainless steel end-fitting

PLY	θ	X_T	X_C	Y_T	Y_C	S
1	15	4.9	6.2	1.4	10.0	1.6
2	-15	7.7	5.2	1.5	8.8	1.6
3	45	4.0	7.2	2.2	15.0	4.1
4	-45	15.5	6.1	**1.2**	11.8	3.5
5	-45	15.5	6.1	**1.2**	13.6	4.1
6	45	4.0	7.0	2.1	14.6	3.9
7	-15	7.7	5.2	1.4	8.3	1.5
8	15	4.9	5.6	1.3	8.9	1.5

Table 4.7: Factors of Safety using Maximum Stress Criterion for $[\pm15/\pm45]_s$ with ¼ inch core and stainless steel end-fitting

PLY	θ	X_T	X_C	Y_T	Y_C	S
1	0	7.0	6.8	1.3	11.3	3.9
2	0	7.0	6.8	1.3	11.3	3.9
3	30	3.6	8.2	1.6	12.0	2.8
4	-30	9.0	6.0	**0.9**	9.4	2.6
5	-30	9.0	6.0	**0.9**	8.3	2.6
6	30	3.6	7.4	1.4	12.0	2.8
7	0	7.0	6.8	1.3	11.3	3.8
8	0	7.0	6.8	1.3	11.3	3.8

Table 4.8: Factors of Safety using Maximum Stress Criterion for $[0_2/30/-30]_s$ with ¼ inch core and stainless steel end-fitting

PLY	θ	X_T	X_C	Y_T	Y_C	S
1	0	16.0	10.2	4.5	22.3	23.3
2	0	15.8	10.1	5.3	27.3	22.7
3	45	8.9	21.6	**2.2**	21.2	4.0

4	-45	36.1	12.3	2.7	11.7	3.4
5	-45	37.2	12.1	2.7	11.7	3.5
6	45	8.8	17.8	2.3	21.0	4.2
7	0	14.2	10.0	5.7	27.5	22.1
8	0	13.9	10.0	4.5	21.8	22.1
9	0	13.7	12.1	6.3	36.9	5.6
10	90	19.6	15.3	3.8	31.9	21.6
11	45	8.4	15.0	8.4	27.5	38.8
12	-45	28.9	10.3	2.5	35.2	38.8
13	45	8.2	13.6	7.6	26.3	38.0
14	-45	26.3	9.6	2.5	32.8	37.7
15	0	12.1	10.6	6.4	34.8	20.0
16	90	24.4	14.4	3.4	27.3	19.7

Table 4.9: Factors of Safety using Maximum Stress Criterion for $[0_2/45/-45]s$ with stainless steel end-fitting but no core including 4 woven patches over hole regions

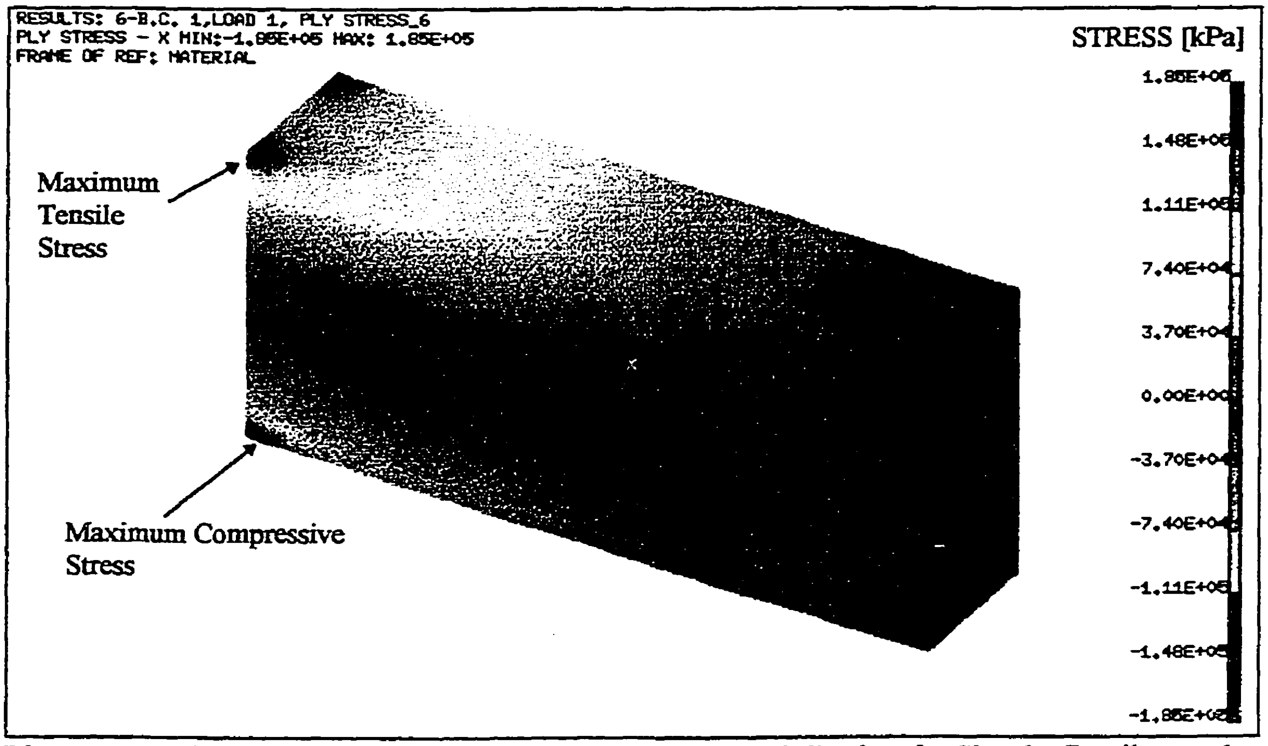

Figure 4.6: Fiber-Direction (X) Stress Contours in Top (0°) Ply of a Simple Cantilevered Box-Beam (Without Holes)

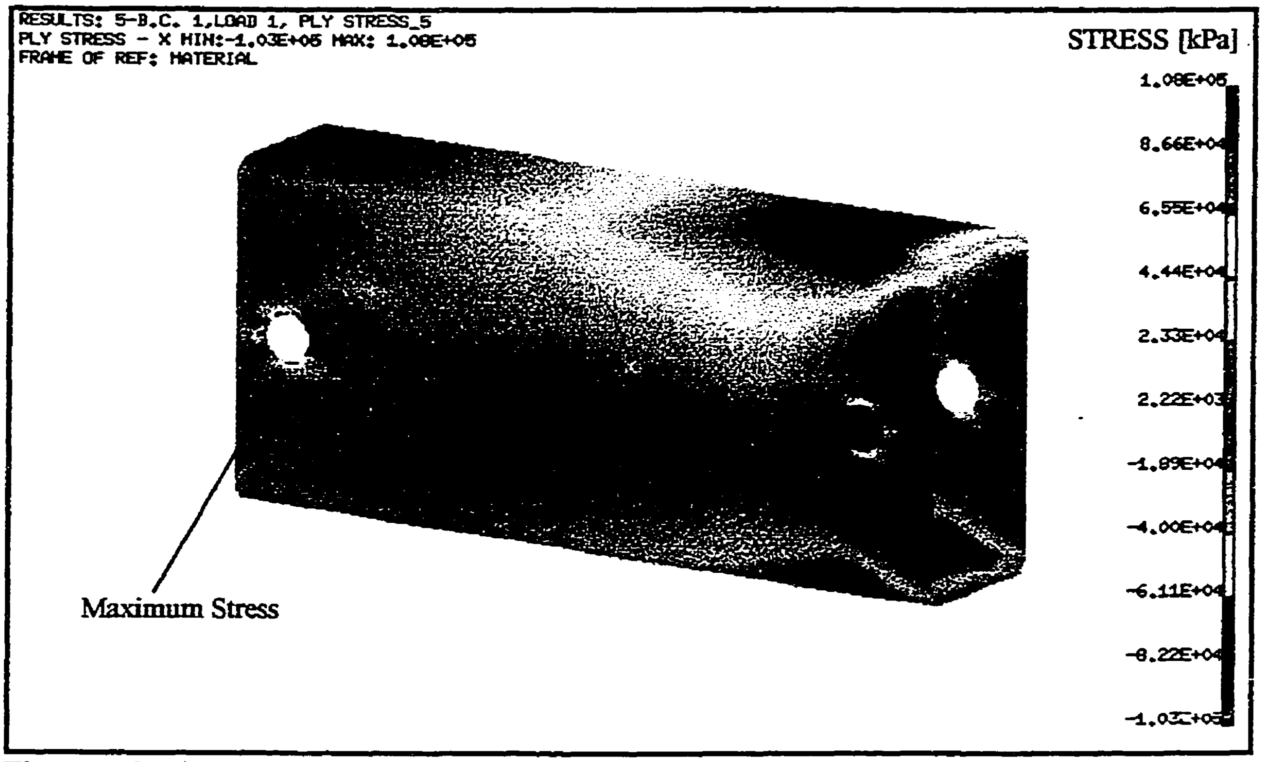

Figure 4.7: Fiber-Direction (X) Stress Contours in Top (0°) Ply of a Cantilevered Box-Beam due to Transverse End Load and In-plane Load at the Holes

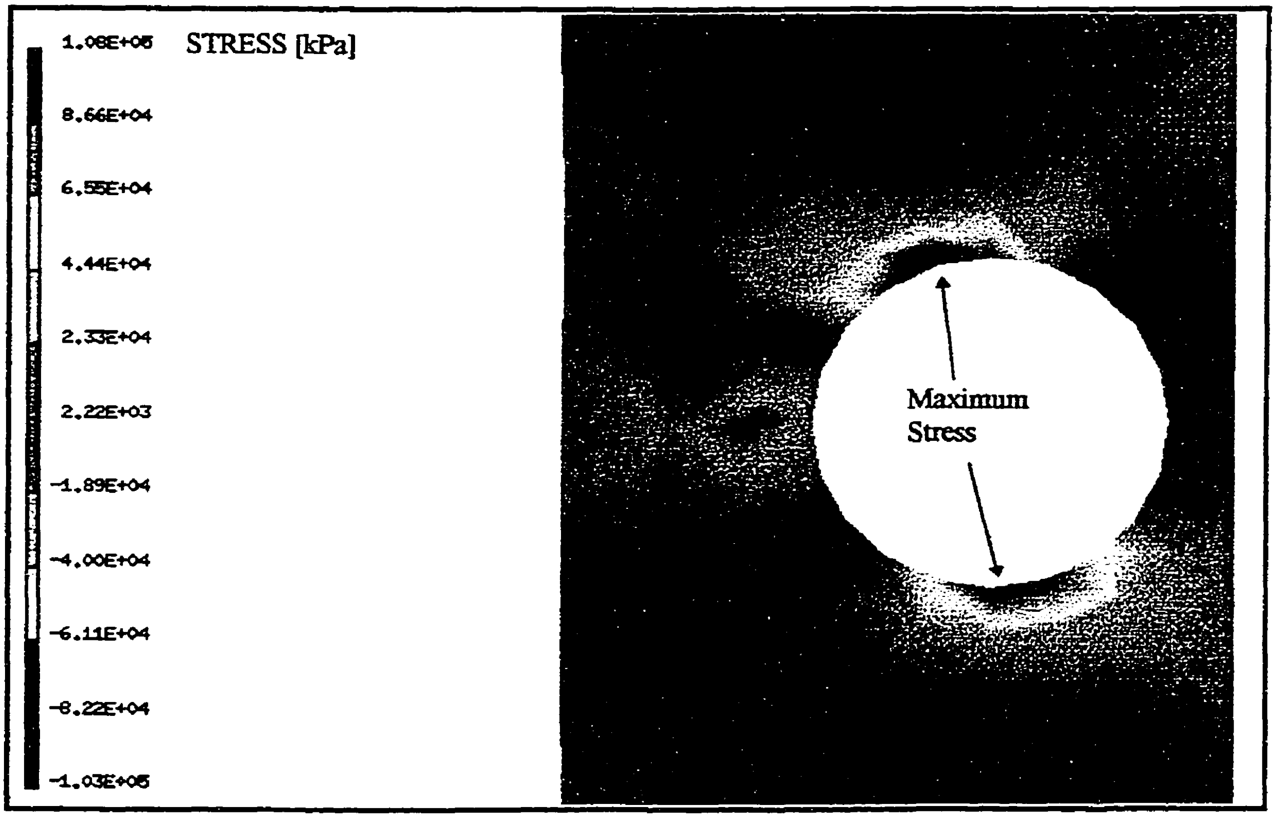

Figure 4.8: Close-up of Fiber-Direction Stress Contours around Holes (Top Ply)

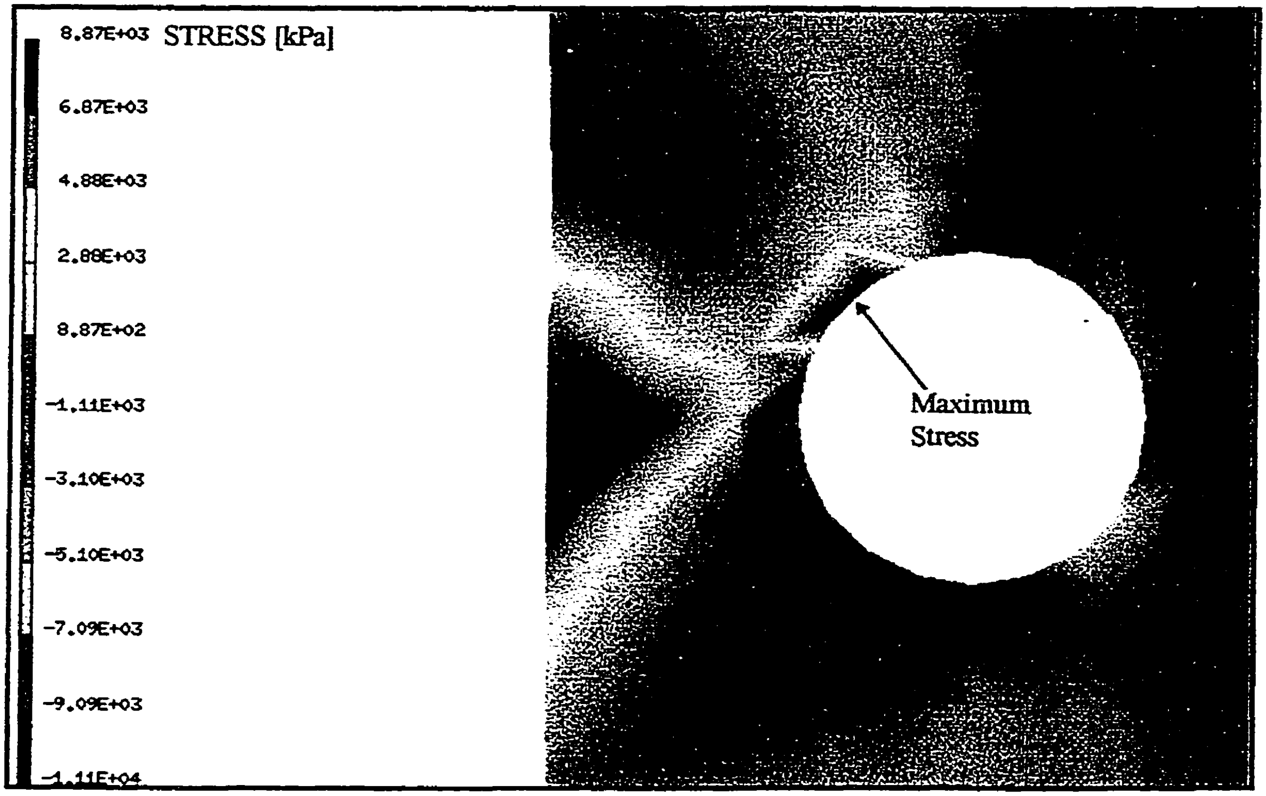

Figure 4.9: Close-up of Matrix-Direction (Y) Stress Contours Around Hole (Top Ply)

Shown in the table below is a comparison of the stresses due to bending and bearing. Clearly, the bearing stresses (stresses at the holes) are more severe and thus dictate the design of the box-beam.

Load Type	X_T	X_C	Y_T	Y_C	S
Bending	78 MPa	-78 MPa	3 MPa	-3 MPa	0 MPa
Bearing	108 MPa	-103 MPa	9 MPa	-9 MPa	4 MPa

Table 4.10: Comparison of Bending and Bearing Stresses in a 0° Ply

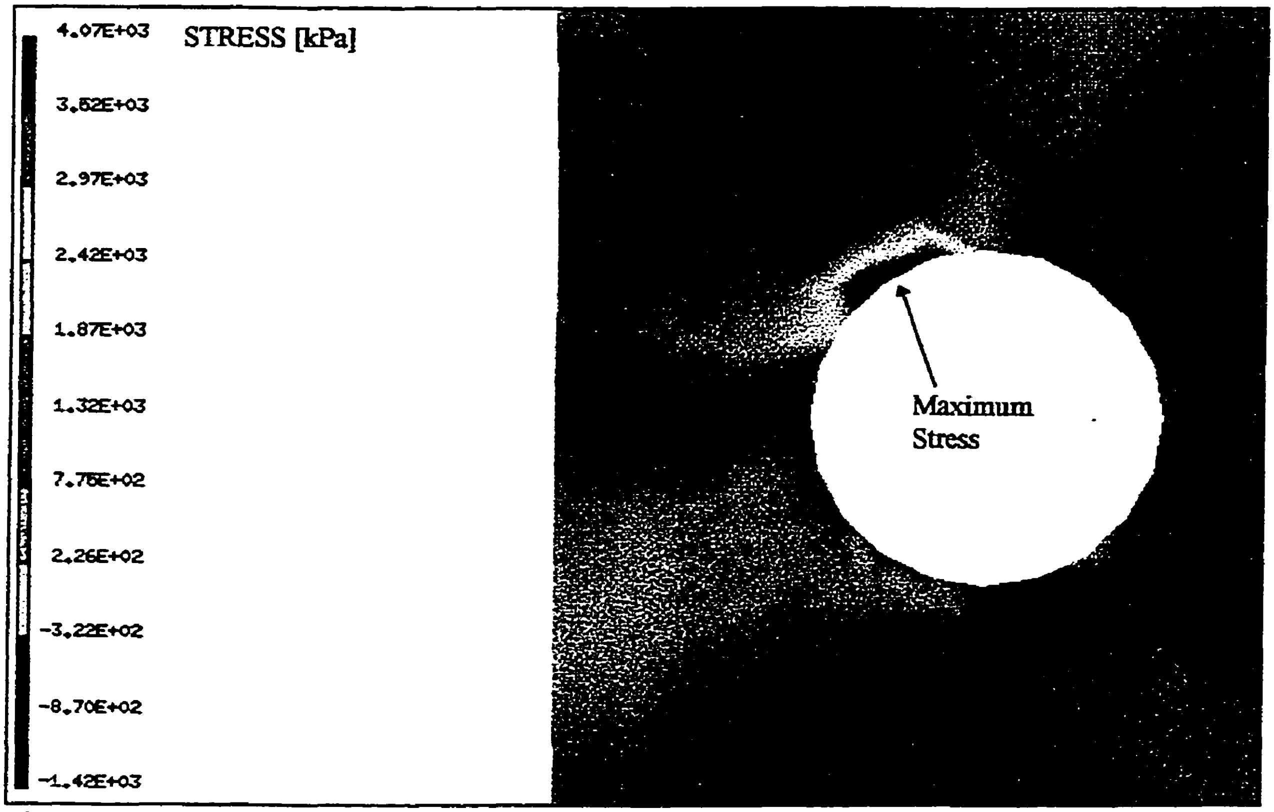

Figure 4.10: Close-up of XY Shear Stress around Hole (Top Ply)

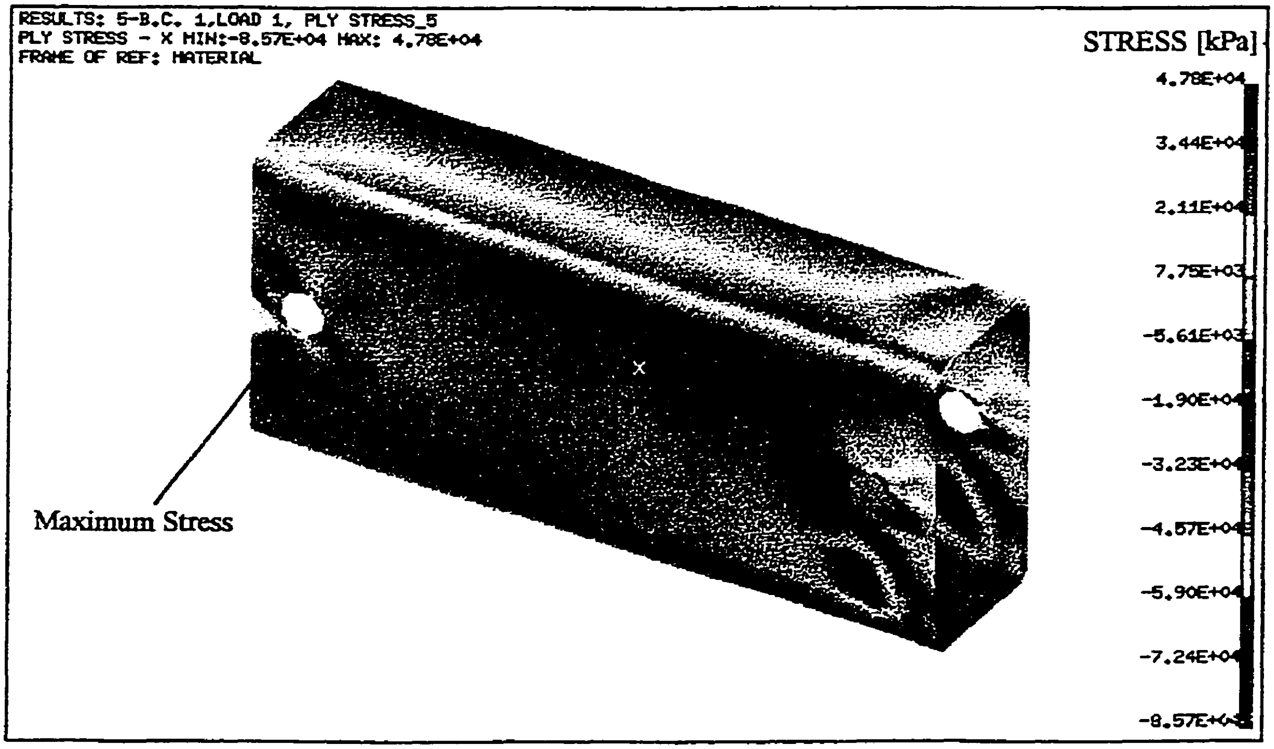

Figure 4.11: X-Stress Contours in 45° ply

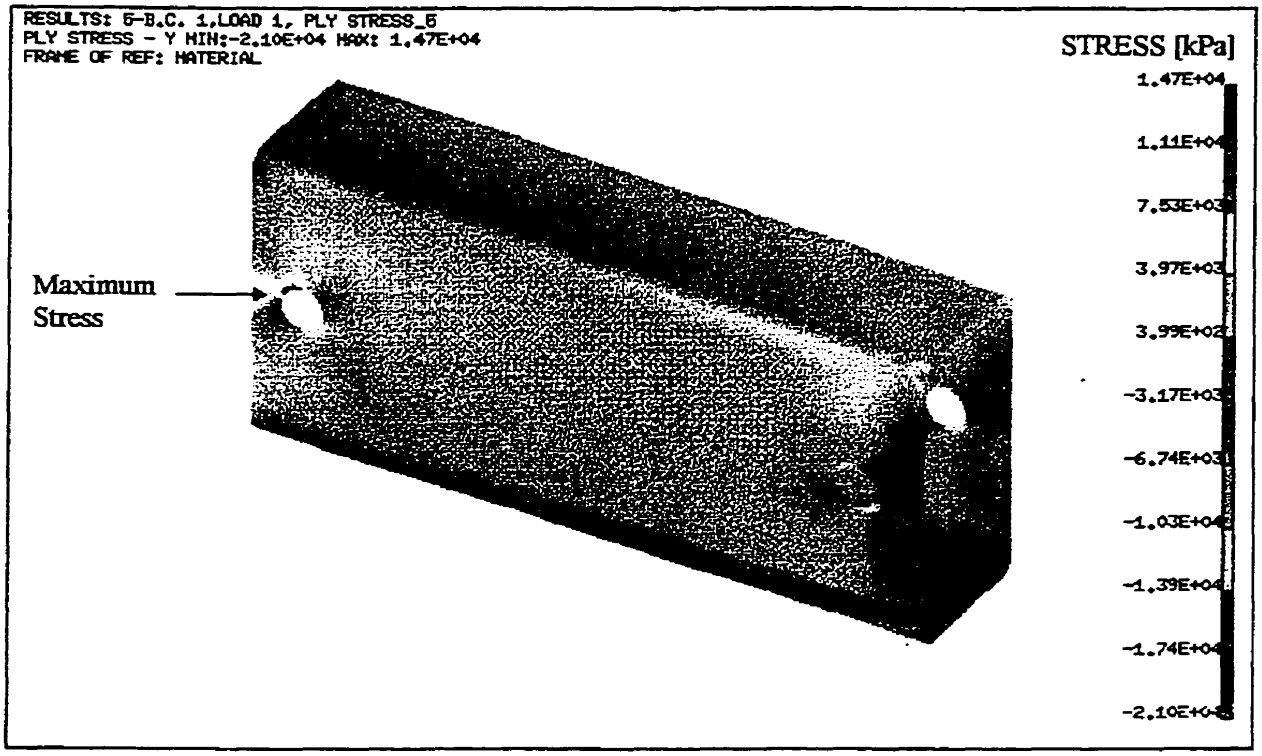

Figure 4.12: Y-Stress Contours in 45° ply

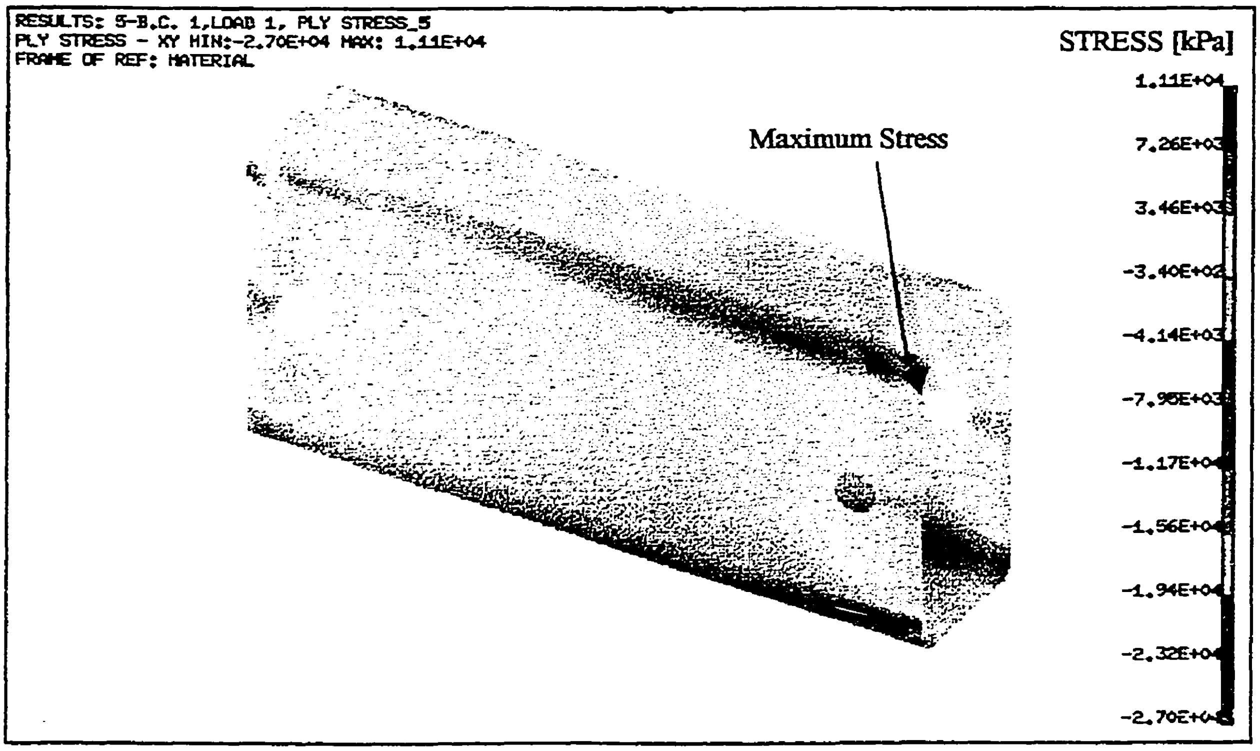

Figure 4.13: XY Shear Stress Contours in 45° ply

4.5 Modification of Box-Beam to Improve Elbow Joint Kinematics

After the elbow joint was assembled inside the composite box-beam, it became apparent that the elbow joint was not achieving its full range of motion due to interference with the box-beam. With the complete box-beam, the range of motion was approximately 90° whereas a fully anthropomorphic elbow mechanism ought to have a pitch of roughly 150°. Since the maximum stresses in the box-beam are concentrated primarily around the holes and at the bottom end (due to the cantilever effect), it was possible to safely cut away a slot at the top of one of the narrow faces as illustrated in the figure below. The amount to be cut away was determined graphically to be a swath 60 mm wide and 90 mm deep. This would allow the elbow mechanism to rotate through a full 150°. A new finite-element model was run to confirm that the machining of the slot would not have any deleterious effects on the structural integrity of the box-beam. The results tabulated below verify that, in fact, no meaningful loss of strength occurs.

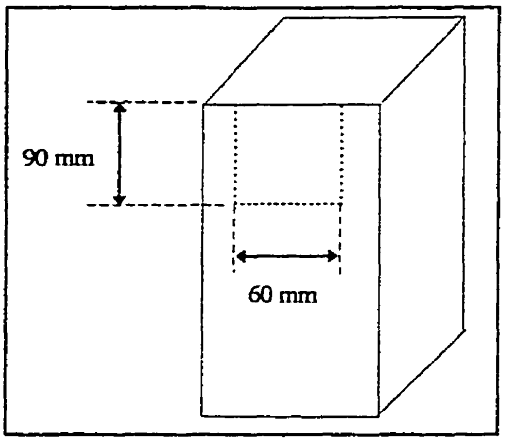

Figure 4.14: Dimensions of Slot

[illegible]	[illegible]	[illegible]	[illegible]	[illegible]	[illegible]	[illegible]
1	0	15.5	14.6	4.4	25.9	22.4
2	0	15.3	14.4	5.5	29.6	22.2

3	45	8.8	30.5	**2.2**	21.4	4.0
4	-45	36.2	16.1	2.7	11.8	3.5
5	-45	37.5	16.3	2.7	11.8	3.5
6	45	8.6	24.3	2.3	21.2	4.2
7	0	13.8	14.2	5.5	19.1	21.6
8	0	13.6	14.0	4.4	15.8	21.6
9	0	13.4	17.4	6.3	34.2	21.3
10	90	13.4	17.4	3.7	31.9	21.1
11	45	8.3	21.2	8.9	26.5	38.3
12	-45	31.2	14.4	2.5	34.6	38.3
13	45	8.1	19.5	8.0	25.7	37.8
14	-45	28.3	13.4	2.4	32.4	37.5
15	0	11.8	15.2	6.3	32.4	19.6
16	90	24.9	18.5	3.3	27.3	19.4

Table 4.11: Factors of Safety using Maximum Stress Criterion for $[0_2/45/-45]s$ with stainless steel end-fitting, no core, 4 woven patches over hole regions, and slot

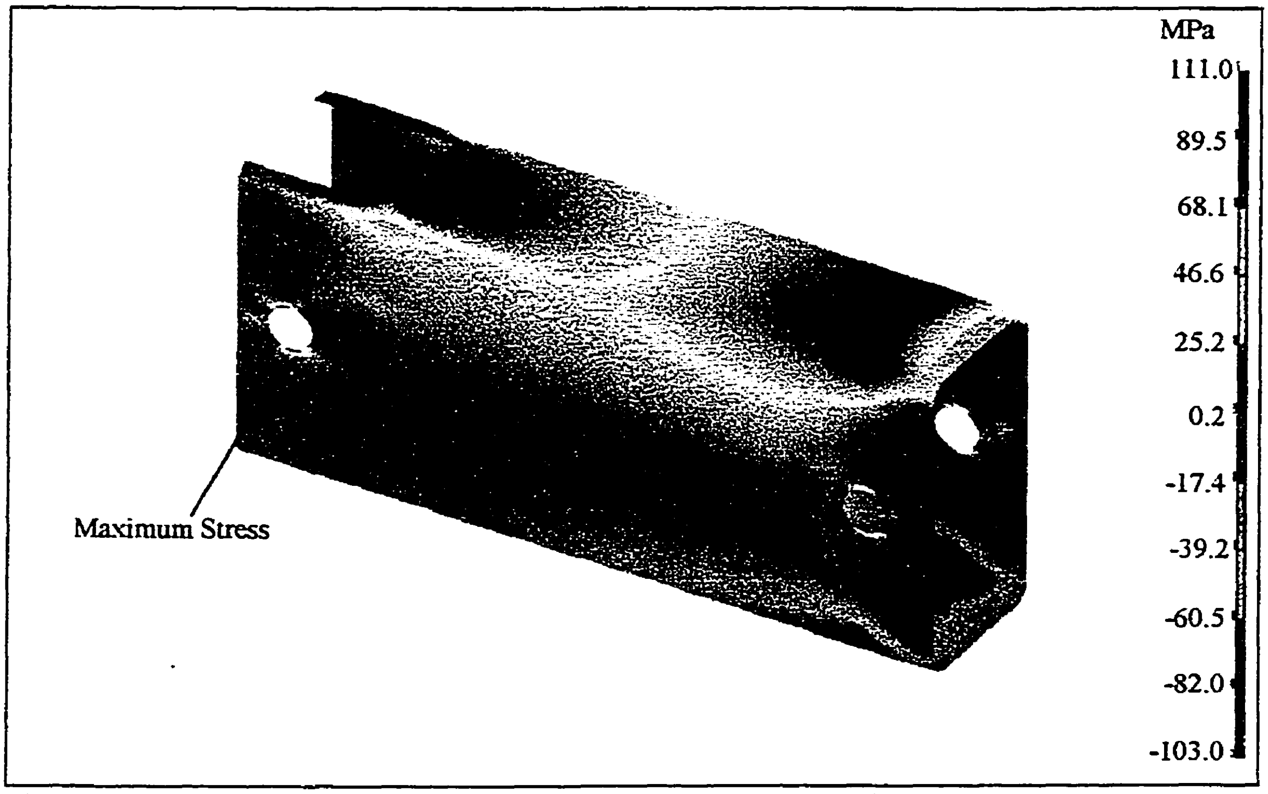

Figure 4.15: X-Stress Contours in Box-Beam with Slot (Top Ply)

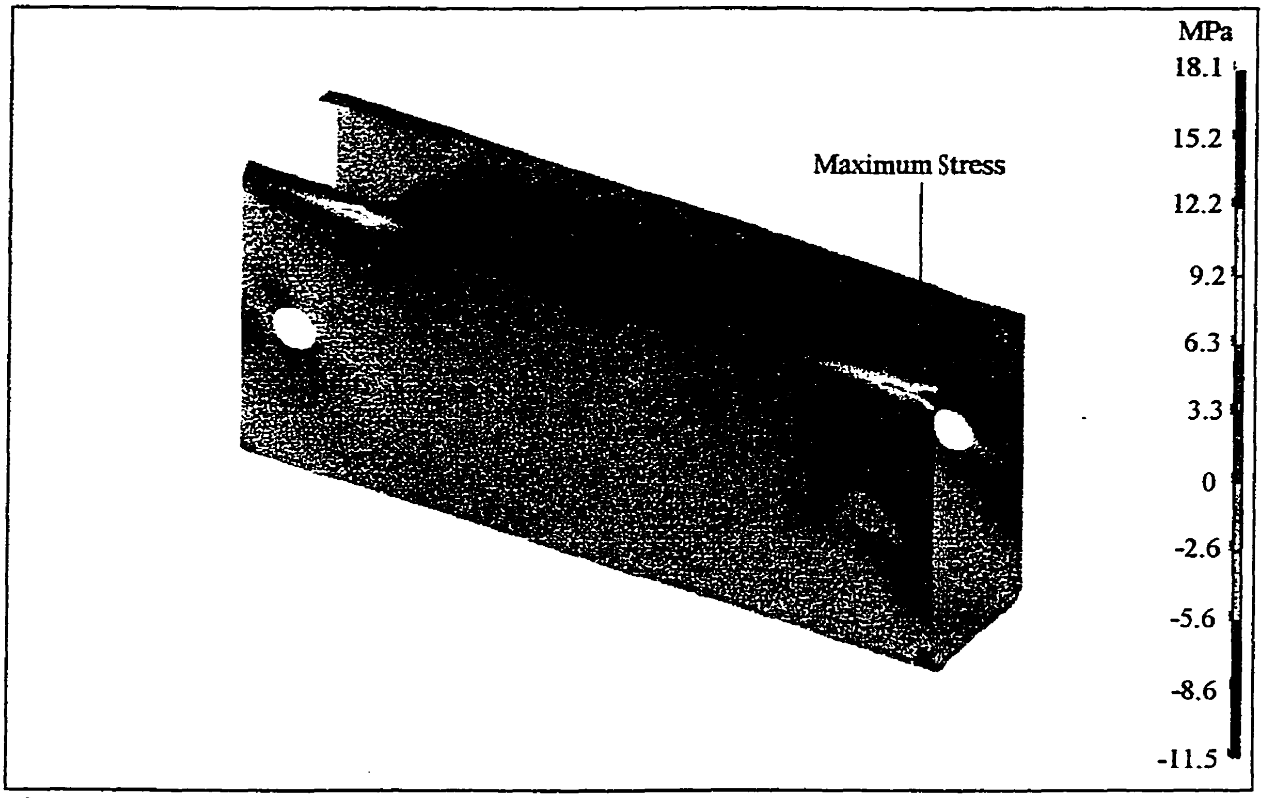

Figure 4.16: Y-Stress Contours of Box-Beam with Slot

4.6 Theoretical Deflection of Box-Beam

It is always good engineering practice to validate finite element analysis with "hand calculations". The vertical deflection of the graphite/epoxy box-beam by the finite element method was 0.381 m. This can be verified analytically by applying Castigliano's energy method [37] where the weight per unit length of the box-beam is neglected. In Equation 4.9, the first term is the standard analytic solution for the deflection of a cantilevered beam and the second term represents the shear correction.

$$w = \frac{PL^3}{3EI} + \frac{tL(h^5 + b^5)}{15GI^2}P \tag{4.9}$$

where $I = 1.096 \times 10^{-5}\ m^4$ (4.10)

$$E = \frac{1}{h}(A_{11} - \frac{A_{12}^{\ 2}}{A_{22}}) = 14.1\ \text{GPa} \tag{4.11}$$

L = 0.315 m, P = 3790 N, t = 7.35 mm, h = 159.7 mm, b = 84.7 mm (4.12)

$$G = \frac{1}{ha_{66}} \tag{4.13}$$

$$\therefore w = 0.255 + 0.130 = 0.385\ m \tag{4.14}$$

Not only does this calculation verify that the finite element model is accurate but it demonstrates the importance of the shear correction term, which accounts for 0.130 m or 34% of the deflection. While it is common practice to ignore the shear correction term when dealing with long isotropic beams, the shear deformation becomes critical when the ratio of the length of the beam to its thickness (measured in the bending plane) is less than 10 and when the degree of anisotropy is large [64,65]. Care must be taken in judging the degree of importance of the latter, as certain formulae for box-beam deflections, such as the one proposed by Tsai [66] neglect the shear correction:

$$w = \frac{PL^3}{3EI^*} \tag{4.15}$$

where $I^* = (3a^2b + a^3)\frac{h}{6}$ (4.16)

where a and b are, respectively, the height and width of the box-beam

$$w = \frac{(3790N)(0.315m)^3}{3(14 \times 10^9 Pa)(1.29 \times 10^{-5} m^4)} \tag{4.17}$$

$$\therefore w = 0.22\ \text{mm} \tag{4.18}$$

The shear-corrected deflection solution can be corroborated by Bank [67,68] who used the Timoshenko/Cowper Method, as follows:

$$w = \frac{PL^3}{3EI} + \frac{PL}{KAG_{SZ}} \tag{4.19}$$

$$K = \frac{20(1+3m)^2}{[(180m^3 + 300m^2 + 144m + 60m^2n^2 + 60mn^2 + 24) - \frac{\nu_{SZ}G_{SZ}}{E}(-30m^2 + 50mn^2 + 30m^2n^2 - 6m + 4)]}$$

$$n = \frac{b}{h} = m$$

$$w = \frac{(3790N)(0.315m)^3}{3(14 \times 10^9)(1.096 \times 10^{-5} m^4)} + \frac{(3790N)(0.315m)}{(0.60(3.38 \times 10^{-3} m^2)(4 \times 10^9 Pa)}$$

$$\therefore w = 0.255 + 0.147 = 0.402mm \tag{4.20 - 4.23}$$

A fourth and final analytical solution, proposed by Caprino and Langella [48] is adduced as further corroboration of the finite-element deflection results. In the following, S represents the shear rigidity, A the cross-sectional area and c the shear factor [69]. The general form using the Rayleigh-Ritz energy method assumes a cosinusoidal deflection:

$$w \equiv f(x,t) = \frac{PL^3}{3EI}(1-\cos\frac{\pi \cdot x}{2L})(1+K)\sin\omega \cdot t \tag{4.24}$$

where K = shear correction term $= \frac{D}{S}(\frac{\pi}{2L})^2$ (4.25)

Obviously, the maximum deflection occurs when sin ωt = 1 and when x = L

$$\therefore w = \frac{PL^3}{3EI}[1+\frac{D}{S}(\frac{\pi}{2L})^2] \tag{4.26}$$

where

$$D \equiv EI = (14\times10^9 Pa)\cdot(1.096\times10^{-5} m^4) \tag{4.27}$$

$$S \equiv \frac{GA}{c} = \frac{(4\times10^9 Pa)\cdot(3.38\times10^{-3} m^2)}{2.0} \tag{4.28}$$

$$\therefore w = \frac{(3790N)(0.315m)^3}{3(14\times10^9 Pa)(1.096\times10^{-5} m^4)}(1+0.57) \tag{4.29}$$

$$\therefore w = 0.404mm \tag{4.30}$$

The five solutions to the deflection of the box-beam are summarized in Table 4.11. With the exception of Tsai's solution, which does not correct for shear deformation, the four remaining solutions are consistent within two hundredths of a millimeter.

Method of Analysis	Deflection [mm]
I-DEAS Finite-element Analysis	0.381
Castigliano's Method [37]	0.385
Tsai [66] without shear correction	0.22
Timoshenko/Cowper Method [67,68]	0.402
Rayleigh-Ritz Energy Method [48]	0.405

Table 4.12: Summary of Box-Beam Deflection Solutions

4.7 Theoretical Stress Analysis

4.7.1 Bending Stress

First, the on-axis modulus matrix is calculated [70]:

$E_X = 126.2$ GPa (4.31)

$E_Y = 10$ GPa (4.32)

$E_S = 2.1$ GPa (4.33)

$\nu_X = 0.3$ (4.34)

$$\frac{\upsilon_X}{\upsilon_Y} = \frac{E_X}{E_Y} \tag{4.35}$$

$$\therefore \upsilon_Y = \frac{\upsilon_X E_Y}{E_X} = \frac{(0.3)(10\,GPa)}{(126.2\,GPa)} = 0.024 \tag{4.36}$$

$$Q_{xx} = mE_x = 127.1\ GPa \tag{4.37}$$

$$Q_{yy} = mE_y = 10.1\,GPa \tag{4.38}$$

$$Q_{xy} = m\upsilon_y E_x = 3.0\,GPa \tag{4.39}$$

$$Q_{SS} = E_S = 2.1\,GPa \tag{4.40}$$

where $m = [1-\upsilon_X\upsilon_Y]^{-1} = [1-0.3)(0.024)]^{-1} = 1.007$ (4.41)

Now the off-axis modulus matrix is calculated:

$$[Q] = \begin{bmatrix} Q_{11} & Q_{12} & Q_{16} \\ Q_{12} & Q_{22} & Q_{26} \\ Q_{16} & Q_{26} & Q_{66} \end{bmatrix} \tag{4.42}$$

where

$$Q_{11} = U_1 + U_2\cos 2\theta + U_3\cos 4\theta \tag{4.43}$$

$$Q_{22} = U_1 - U_2\cos 2\theta + U_3\cos 4\theta \tag{4.44}$$

$$Q_{12} = U_4 - U_3\cos 4\theta \tag{4.45}$$

$$Q_{66} = U_5 - U_3\cos 4\theta \tag{4.46}$$

$$Q_{16} = \frac{1}{2}U_2\sin 2\theta + U_3\sin 4\theta \tag{4.47}$$

$$Q_{26} = \frac{1}{2}U_2\sin 2\theta - U_3\sin 4\theta \tag{4.48}$$

where

$$U_1 = \frac{1}{8}[3Q_{xx} + 3Q_{yy} + 2Q_{xy} + 4Q_{SS}] = 53.2\ GPa \tag{4.49}$$

$$U_2 = \frac{1}{2}[Q_{xx} - Q_{yy}] = 58.5\ GPa \tag{4.50}$$

$$U_3 = \frac{1}{8}[Q_{xx} + Q_{yy} - 2Q_{xy} - 4Q_{SS}] = 15.4\ GPa \tag{4.51}$$

$$U_4 = \frac{1}{8}[Q_{xx} + Q_{yy} + 6Q_{xy} - 4Q_{SS}] = 18.4\ GPa \tag{4.52}$$

$$U_5 = \frac{1}{8}[Q_{xx} + Q_{yy} - 2Q_{xy} + 4Q_{SS}] = 17.5\ GPa \tag{4.53}$$

Thus, the off-axis moduli of each ply can be calculated by substitution of the appropriate angle into the above expressions. Since the laminate in question is $[0_2/45/-45]s$, we need only calculate the off-axis moduli of the 0° and 45° plies.

$$[Q]_{0^\circ} = \begin{bmatrix} 127.1 & 3.0 & 0 \\ 3.0 & 10.1 & 0 \\ 0 & 0 & 2.1 \end{bmatrix} GPa \tag{4.54}$$

$$[Q]_{45^\circ} = \begin{bmatrix} 37.8 & 33.8 & 29.3 \\ 33.8 & 37.8 & 29.3 \\ 29.3 & 29.3 & 32.9 \end{bmatrix} GPa \tag{4.55}$$

$$[Q]_{-45^\circ} = \begin{bmatrix} 37.8 & 33.8 & -29.3 \\ 33.8 & 37.8 & -29.3 \\ -29.3 & -29.3 & 32.9 \end{bmatrix} GPa \tag{4.56}$$

To obtain the strain in the various plies of the box-beam, the curvature of the beam must first be calculated:

$$K_1 = \frac{M}{EI} \tag{4.57}$$

For laminates, E must be replaced by an effective modulus defined as follows:

$$E = E_0^1 = \frac{1}{a_{11}} \tag{4.58}$$

Thus, the matrix [a], representing the laminate compliance, is required. To obtain [a], its inverse, the laminate modulus [A], must first be calculated.

$$[A]=\begin{bmatrix} A_{11} & A_{12} & A_{16} \\ A_{12} & A_{22} & A_{26} \\ A_{16} & A_{26} & A_{66} \end{bmatrix} \text{ where } \begin{matrix} A_{11}=\frac{1}{h}\int_{-h/2}^{h/2} Q_{11}dz & A_{12}=\frac{1}{h}\int_{-h/2}^{h/2} Q_{12}dz \\ A_{16}=\frac{1}{h}\int_{-h/2}^{h/2} Q_{16}dz & A_{22}=\frac{1}{h}\int_{-h/2}^{h/2} Q_{22}dz \\ A_{26}=\frac{1}{h}\int_{-h/2}^{h/2} Q_{26}dz & A_{66}=\frac{1}{h}\int_{-h/2}^{h/2} Q_{66}dz \end{matrix} \quad (4.59)$$

where h is the thickness of the laminate.

$$\therefore [A]=\begin{bmatrix} A_{11} & A_{12} & A_{16} \\ A_{12} & A_{22} & A_{26} \\ A_{16} & A_{26} & A_{66} \end{bmatrix}=\begin{bmatrix} 82.5 & 18.4 & 0 \\ 18.4 & 24.0 & 0 \\ 0 & 0 & 17.5 \end{bmatrix} GPa \quad (4.60)$$

But $[a] = [A]^{-1}$

$$\therefore [a]=\begin{bmatrix} a_{11} & a_{12} & a_{16} \\ a_{12} & a_{22} & a_{26} \\ a_{16} & a_{26} & a_{66} \end{bmatrix}=\begin{bmatrix} 0.0146 & -0.0112 & 0 \\ -0.0112 & 0.0503 & 0 \\ 0 & 0 & 0.0571 \end{bmatrix}\frac{1}{GPa} \quad (4.61)$$

$$\therefore E_1^0=\frac{1}{0.0146}=68.5\ GPa \quad (4.62)$$

Next, the moment of inertia is computed, based on the geometry shown in Figure 4.17.

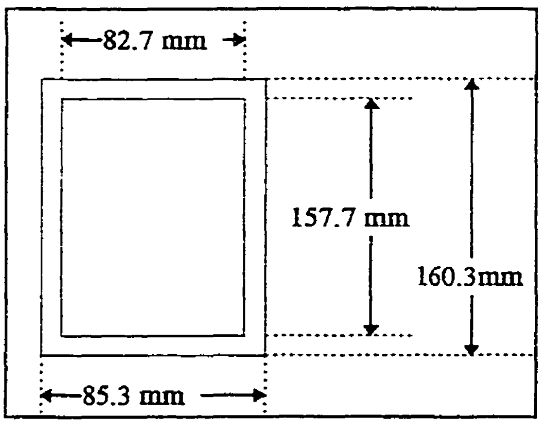

Figure 4.17: Dimensions of Box-Beam

$$I = \frac{1}{12}\left((85.3)(160.3)^3 - (82.7)(157.7)^3\right) = 2.25 \times 10^{-6}\ m^4 \tag{4.63}$$

Therefore, in the plane of the largest load, the curvature in the box-beam is:

$$K = \frac{(3790N)(0.315\,m)}{(68.5 \times 10^9\ Pa)(2.25 \times 10^{-6}\,m^4)} = 7.75 \times 10^{-3}\ m^{-1} \tag{4.64}$$

Accordingly, the induced curvatures are:

$$K_2 = -\upsilon_{21}^0 K_1 \tag{4.65}$$

$$K_3 = \upsilon_{61}^0 K_1 \tag{4.66}$$

where the coupling constants are defined as:

$$\upsilon_{21}^0 \equiv \frac{-a_{21}}{a_{11}} = \frac{-(-0.0112)}{(0.0146)} = 0.767 \tag{4.67}$$

$$\upsilon_{61}^0 \equiv \frac{a_{61}}{a_{11}} = 0 \tag{4.68}$$

$$\therefore K_2 = -5.94 \times 10^{-3}\ \frac{1}{m} \tag{4.69}$$

$$K_3 = 0 \tag{4.70}$$

The strain in a ply is related to the curvature in the following manner:

$$\varepsilon_1 = K_1 z \tag{4.71}$$

$$\varepsilon_2 = K_2 z \tag{4.72}$$

where z is defined below in Figure 4.18.

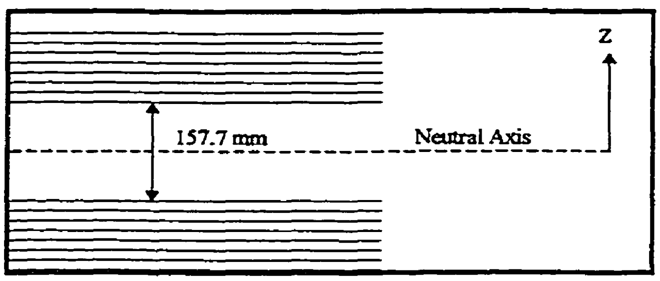

Figure 4.18: Ply Distance from Neutral Axis

PLY #	θ (°)	z (mm)	ε_1 (x10^{-4})	ε_2 (x10^{-4})
1	0	79.015	6.12	-4.69
2	0	79.180	6.14	-4.70
3	45	79.345	6.15	-4.71
4	-45	79.510	6.16	-4.72
5	-45	79.675	6.17	-4.73
6	45	79.840	6.19	-4.74
7	0	80.005	6.20	-4.75
8	0	80.170	6.21	-4.76

Table 4.13: Ply Strains

Finally, the off-axis ply stresses can be calculated using the stress-strain relations involving the modulus matrix [Q] for each ply.

$$[\sigma] = [Q][\varepsilon] \tag{4.73}$$

which can be expanded as follows:

$$\begin{bmatrix} \sigma_1 \\ \sigma_2 \\ \sigma_3 \end{bmatrix} = \begin{bmatrix} Q_{11} & Q_{12} & Q_{16} \\ Q_{12} & Q_{22} & Q_{26} \\ Q_{16} & Q_{26} & Q_{66} \end{bmatrix} \begin{bmatrix} \varepsilon_1 \\ \varepsilon_2 \\ \varepsilon_3 \end{bmatrix} \tag{4.74}$$

Thus, for ply 8, oriented at 0°,

$$\sigma_1 = (127.1\ GPa)(6.21 \times 10^{-4}) + (3.0\ GPa)(-4.76 \times 10^{-4}) = 77.5\ MPa \tag{4.75}$$
$$\sigma_2 = (3.0\ GPa)(6.21 \times 10^{-4}) + (10.1\ GPa)(-4.76 \times 10^{-4}) = -2.9\ MPa \tag{4.76}$$
$$\sigma_3 = 0\ MPa \tag{4.77}$$

Similarly, for ply 6, oriented at 45°,

$$\sigma_1 = (37.8\ GPa)(6.19 \times 10^{-4}) + (33.8\ GPa)(-4.74 \times 10^{-4}) = 7.4\ MPa \tag{4.78}$$
$$\sigma_2 = (33.8\ GPa)(6.19 \times 10^{-4}) + (37.8\ GPa)(-4.74 \times 10^{-4}) = 3.0\ MPa \tag{4.79}$$
$$\sigma_3 = 0\ MPa \tag{4.80}$$

Evidently, the bending stresses are quite low. This is rather intuitive since a box-beam of these dimensions has such a large moment of inertia, that an end load of 3790 Newtons is not enough to create much flexure. However, the stresses due to the loading at the holes is much more severe and is ultimately the critical aspect in the overall design.

4.7.2 Stresses at Holes

The actuators that drive the elbow mechanism are connected to the box-beam by two shafts. The maximum load of each actuator is 1340 Newtons, which is transferred to the four holes of the box-beam.

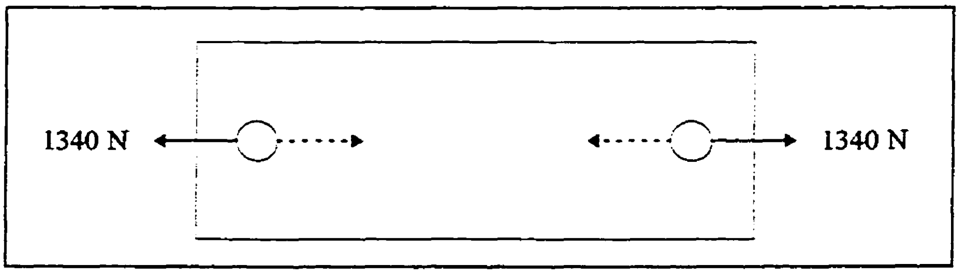

Figure 4.19: Loading of Holes by Actuators

The three fundamental stress components around a pin-loaded hole are bearing, tensile and shear, whose average values are:

$$\sigma_b = \frac{P}{td} \tag{4.81}$$

$$\sigma_t = \frac{P}{(w-d)t} \tag{4.82}$$

$$\sigma_s = \frac{P}{2et} \tag{4.83}$$

where t is the thickness of the laminate, P is the applied load, d the diameter of the hole, e the distance from the edge and w the width, as shown in Figure 4.20.

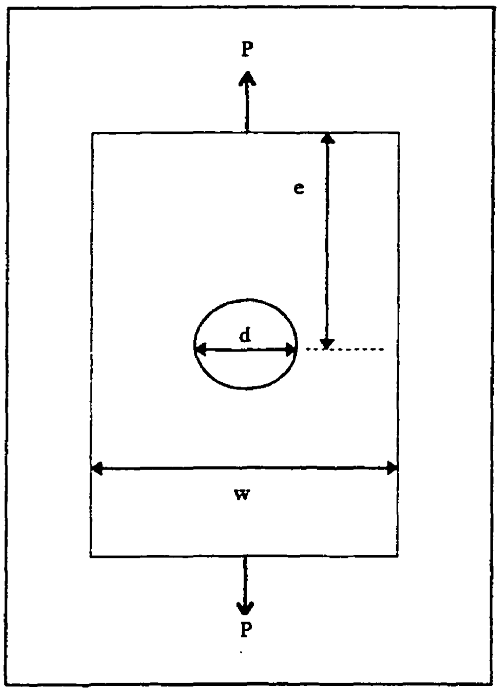

Figure 4.20: Dimensions of a Pin -Loaded Laminate

$$\sigma_b = \frac{1340\ N}{(132\ mm)(16\ mm)} = 63.4\ MPa \tag{4.84}$$

$$\sigma_t = \frac{1340\ N}{(157.7\ mm - 16\ mm)(132\ mm)} = 7.2\ MPa \tag{4.85}$$

$$\sigma_s = \frac{1340\ N}{2(24\ mm)(132\ mm)} = 21.1\ MPa \tag{4.86}$$

To verify the finite-element analysis, the bearing stress should be calculated "locally" on the segment of the hole which is loaded the most. Since the load in the finite-element model is distributed cosinusoidally over nine nodes, one approach would be to calculate the bearing stress by considering only the three nodes with the largest applied loads:

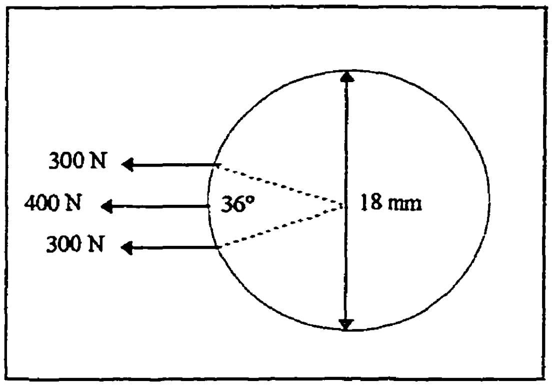

Figure 4.21: Three Nodes with Highest Loads

The sector over which these three loads are distributed is obtained from the arc length:

$$s = r\theta = (9\ mm)(\frac{36^o}{180^o}\pi) = 5.65\ mm \tag{4.87}$$

Now the local bearing stress can be obtained:

$$\sigma_b = \frac{(300+400+300)N}{(1.32\,mm)(5.65\,mm)} = 134\,MPa \tag{4.88}$$

According to Eckold [71], if the ratio of the hole diameter to the thickness of the laminate is greater than unity, as it is in this case, then the maximum bearing stress is diminished unless clamping pressure on the laminate is applied. Using ±45° plies and interference fits attenuate the stress. Generally, it is preferable for the bearing stress to exceed the tensile and shear stresses for the simple reason that bearing failure is typically not catastrophic. The expected mode of bearing failure would be characterized by shear cracks induced by local compression [72-74]. It is important to emphasize that bearing strengths can be greatly weakened by defects caused by imperfect machining techniques [75-77].

4.8 Box-Beam Comparison

For the sake of comparison, two box-beams, one steel and one aluminum, of equal wall-thickness were also analyzed for maximum principal stress, maximum deflection, and natural frequency. For the latter, I-DEAS Master Series 2.1 computed the three natural frequencies using Constraint Mode Dynamics, a vector iterative solution. Note that for the two metal box-beams, the factor of safety is calculated by simply dividing the maximum principal stress from the finite-element analysis by the yield strength. For the aluminum box-beam, the maximum principal stress was 110 MPa whereas for the steel box-beam the maximum principal stress was only 87 MPa. Although the stress around the holes is due primarily to the direct loading of the holes through the main actuator shafts, there is also a minor contribution from the bending of the box-beam due to the end load. Since the steel box-beam has the highest yield strength and highest flexural rigidity, its factor of safety is highest and its maximum deflection is lowest. For the graphite/epoxy box-beam, the safety factor is the minimum value of the all the safety factors previously calculated and tabulated. The results are summarized in the table shown below:

Material	Graphite/Epoxy LTM25	Aluminum 6061-T6	Stainless Steel 303
Factor of Safety	2.2	2.2	2.8
Max. Deflection	0.38 mm	0.35 mm	0.11 mm
Mass	418 g	729 g	2133 g
Deflection × Mass	159 g·mm	255 g·mm	235 g·mm
Vertical Nat. Freq.	576 Hz	148 Hz	245 Hz
Horizontal Nat. Freq.	1064 Hz	185 Hz	290 Hz
Extensional Nat. Freq.	1206 Hz	209 Hz	297 Hz

Table 4.14: Comparison of Box-Beams made of Graphite/epoxy, Aluminum and Steel

Although the graphite/epoxy box-beam has the lowest safety factor and deflects the most, it is by far superior to the aluminum and steel box-beams on a per unit mass basis. Moreover, the graphite/epoxy box-beam exhibits much higher natural frequencies. This is particularly significant in controlling the overall robotic arm. If the natural frequency falls below the sampling rate (in Hertz), then the control system cannot react properly. However, it should be noted that to truly evaluate any improvements in natural frequency, the entire arm should be considered as a whole. In addition, the epoxy matrix has superb damping characteristics [78] which help to reduce the vibration of the links and ultimately lowers the settling time of the end-effector.

4.9 Fabrication of Graphite/Epoxy Box-Beam

The box-beam was fabricated using LTM25 graphite/epoxy prepreg furnished by the Advanced Composites Group. An external aluminum mold was designed so as to achieve a smooth external finish on the composite part. This also allowed the external dimensions of the composite box-beam to be precisely controlled so that it would mate with the stainless steel end-fitting, allowing for a bond thickness of 0.50 mm.

The fabrication procedure was relatively straightforward. First, the inside of the mold was coated three times with Frekote Sealer B-15. Then, three coatings of Frekote 700-NC release agent were applied [79]. Four unidirectional plies were cut from the roll of prepreg to slightly larger dimensions than the actual interior surface area of the mold to allow for overlap. Laying these large plies proved to be rather arduous due to the tackiness of the material as well as the limited space inside the mold. This was overcome by slicing each ply into four thin strips. The ±45° plies were cut diagonally from a woven prepreg (0°/90°). Angle-plies (±θ°) can also be made from unidirectional plies by using a paper-folding technique [80] which reduces the amount of scrap as well as the cutting time. For two of the composite box-beams, honeycomb cores were sandwiched between the layers of the graphite/epoxy to give the faces additional rigidity [81]. However, both the aluminum flex-core and the Nomex honeycomb hindered the compaction of the layers around the corners of the box-beam. In the end, it was decided that the rigidity of the faces of the box-beam was non-essential. Since the honeycomb adds practically nothing to the in-plane strength around the box-beam's four holes, the honeycomb was discarded from the design. Four patches of woven LTM25 graphite/epoxy were used to reinforce the hole regions. In addition, four Renshape blocks were inserted under the woven patches to improve the rigidity of the hole regions and to facilitate the machining of the holes.

4.9.1 Vacuum-Bagging Technique

Once the plies of graphite/epoxy have been properly pressed down to remove bubbles and wrinkles, a release film covers the plies and prevents the breather from sticking to the epoxy during the cure cycle. The breather is permeable to air but prevents the epoxy from being drawn into the suction. The vacuum bag is then wrapped around the mold. In the case of the external mold, two bags were used, one on the inside and one on the outside of the mold. The inner and outer bags were then joined and sealed using sticky gum. The bag is pierced and the vacuum valve seals the opening [82].

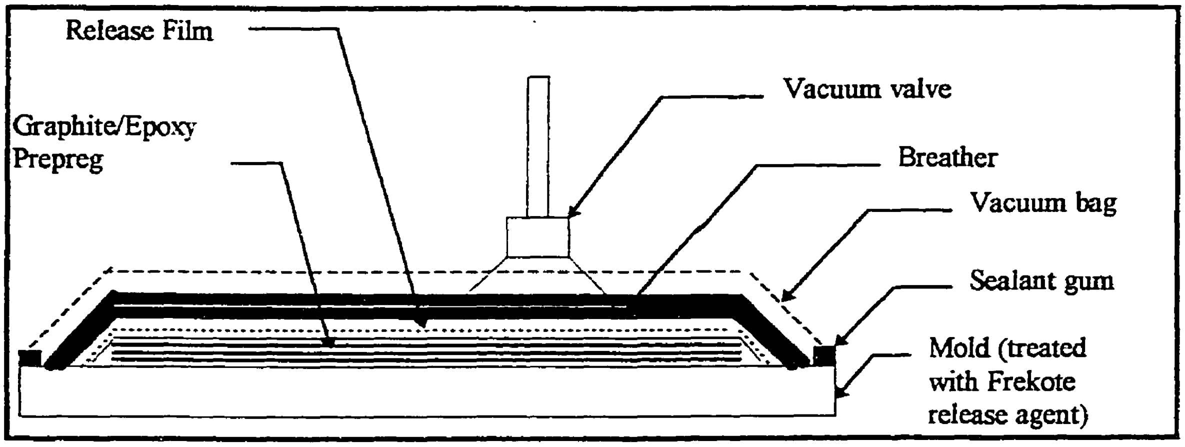

Figure 4.22: Vaccum-Bagging Technique

Finally, approximately 1 atmosphere of vacuum is drawn and the lay-up is then cured in an oven following the temperature cycle shown below.

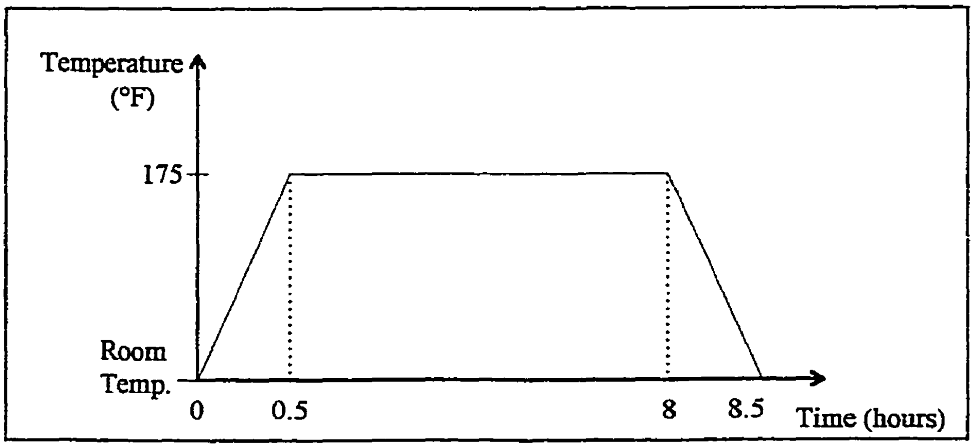

Figure 4.23: Cure Cycle for LTM25

Upon completion of the cure cycle, the mold is opened and, if the Frekote release agent was properly applied, the graphite/epoxy box is easily removed.

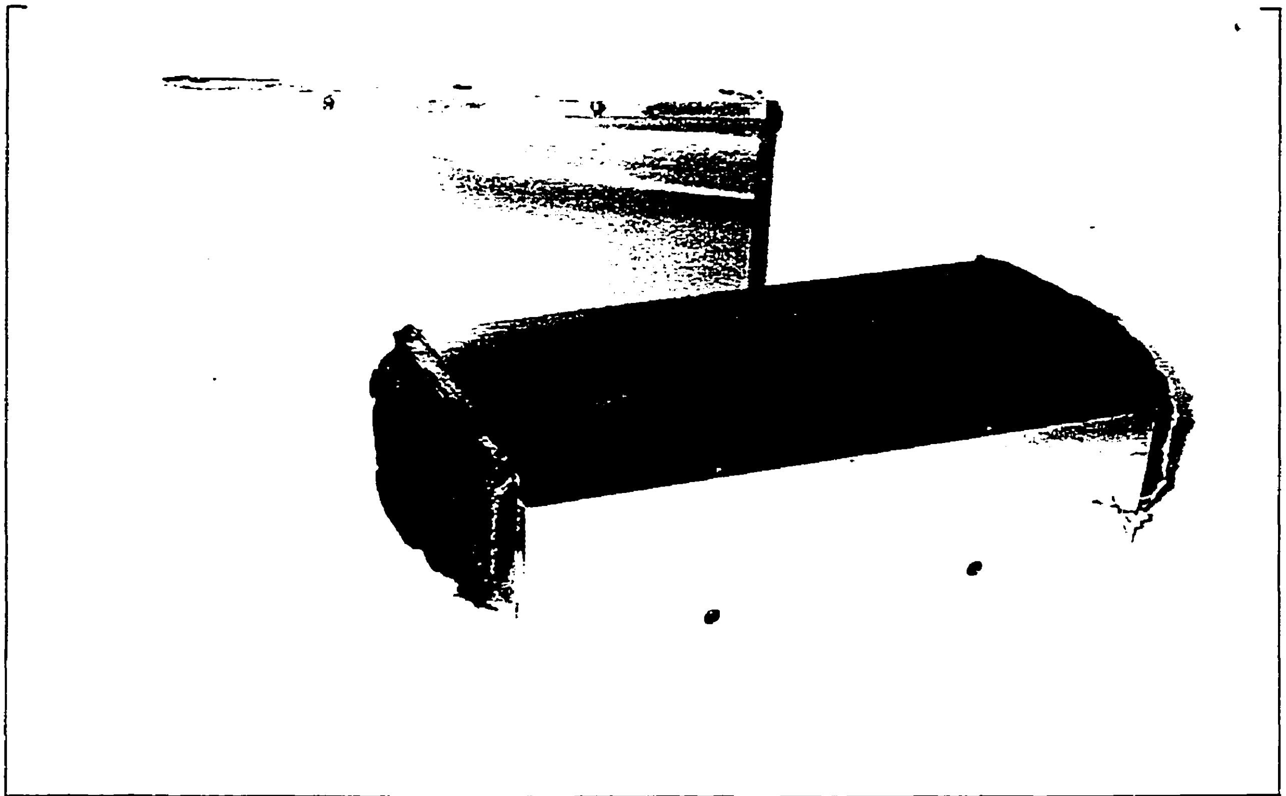

Figure 4.24: Removing the Cured Graphite/Epoxy Box-Beam from the Aluminum Mold

4.9.2 Machining of the Box-Beam

To undertake precision machining of the graphite/epoxy box-beam at McGill proved to be an arduous task because tungsten carbide-tipped or diamond-encrusted tools are required. Secondly, not only is the carbon dust a carcinogen but it also dirties the gear trains of conventional machine tools. For these reasons, the graphite/epoxy box-beam was milled, ground and drilled by Progressive Machine Works in Anjou, Quebec.

4.10 Box-Beam Strength Test

In order to ascertain whether the preceding computer models and calculations are accurate, a tension test was performed on one of the graphite/epoxy box-beams in an MTS machine [83]. The box-beams were designed to withstand a load of 1340 Newtons on each hole with a factor of safety of 2.2. To simulate the effect of two actuators loading the shafts that are restrained by the holes in the box-beam, a load was applied at the center of the shafts which by symmetry distributed itself equally on all holes. Thus, while the MTS machine applied from 0 to 10 kN, the load applied to each hole varied from 0 to 5 kN.

Figure 4.25: MTS Tension Test Set-up

Although the box-beam was expected to fail at a load of approximately 3 kN (per hole), taking into consideration the factor of safety of 2.2, in actuality the box-beam survived the full 5 kN per hole. At that point, however, bearing failure became observable. The following graph shows the tensile load on each hole as a function of displacement. The discrepancy between the theoretical and experimental strength of the box-beam is explained by the fact that certain values for the mechanical properties of the LTM25 graphite/epoxy were unavailable and hence had to be inferred from the data sheet.

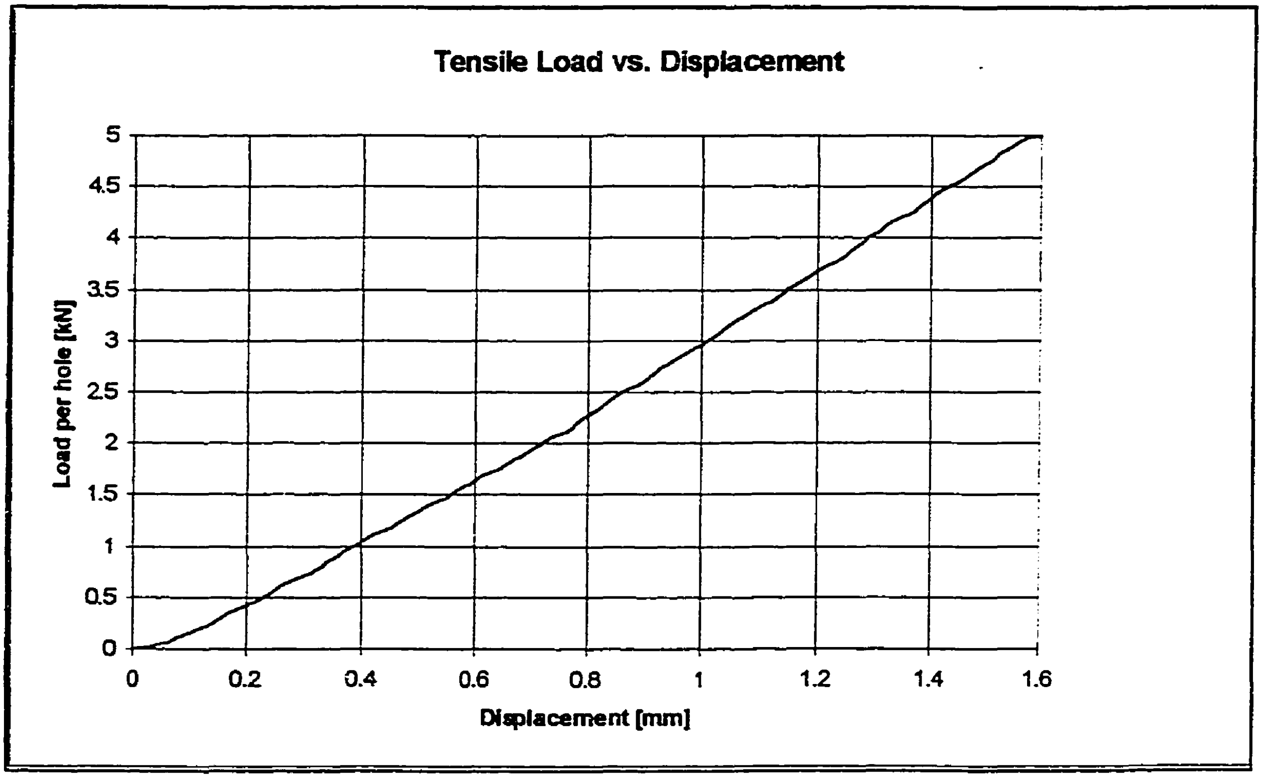

Figure 4.26: Linear Variation of Tensile Load with Displacement

4.11 Stainless Steel End-Fitting

When selecting a method of joining graphite/epoxy to metal, the factors which should be considered are the magnitude of the force involved, the geometry of the parts to be attached, whether disassembly is required, cost and reliability. Both bolted and bonded joints have numerous advantages. Whereas bolted joints are highly reliable, conducive to inspection, resilient to fatigue and allow for repeated assembly and disassembly, bonded joints enjoy a greater bond efficiency (bond strength/weight of joint), reduce the number of parts involved, minimize corrosion and avoid problems of laminate strength degradation incurred when drilling holes in composites [84-86]. The choice to bond the end-fitting bracket to the graphite/epoxy box-beam was largely due to availability of a large, easily accessed bond surface as well as the desire to preserve as much as possible the structural integrity of the box-beam by avoiding unnecessary holes. The second fundamental decision was the type of material to be used. Since graphite is an extremely cathodic material, the choice of material is not merely a function of strength, stiffness and density. When dissimilar metals are in contact in an electrolytic environment there is a galvanic potential developed between them [87,88]. The engineering materials that are least corroded by graphite composites are titanium and stainless steel [89]. As shown by the list of metals in Appendix D, aluminum would have been a poor choice for the end-fitting.

Although the adhesive itself acts as the primary protection against corrosion in graphite-to-metal bonded joints [90], further protection can be acquired through the use of an etchant, especially needed when joining aluminum to graphite. Yet another factor to be considered in joining metals to graphite is thermal expansion. The thermal mismatch between aluminum and graphite is the most severe while graphite and titanium is minimum. Although titanium is most compatible with graphite, it is an expensive metal and one that is difficult (and hence costly) to machine. For the Lightarm manipulator, where temperature variations are minor but where the environment might lead to corrosion, stainless steel was selected as the simplest and most cost-effective solution. In a bonded joint, there is a stress concentration at the edge of the bond. This can be attenuated by approximately 50% by tapering the metal end fitting. The optimal chamfer angle has been determined to be roughly 7° [91,92].

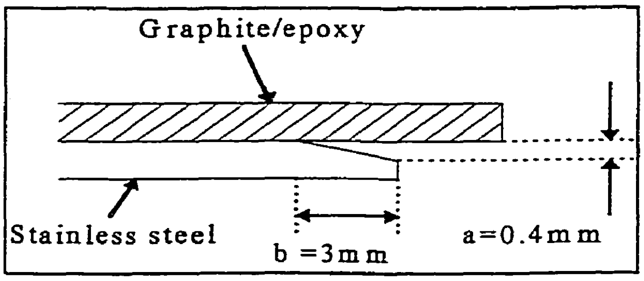

Figure 4.27: Dimension of End-fitting Chamfer

4.12 Stress Analysis of Adhesive Bond

A finite-element model consisting of 522 solid brick elements was constructed to study the stresses present in the adhesive bond during a worst-case static loading of the manipulator. The moment produced by the cantilever load of 3790 Newtons is counterbalanced by the shear forces in the bond. The magnitude of the shear forces is readily obtained by a simple moment balance. The bond thickness was chosen to be 0.5 mm [93,94]. The results of the FEA show quite clearly that the areas of maximum stress are located at the curved corners.

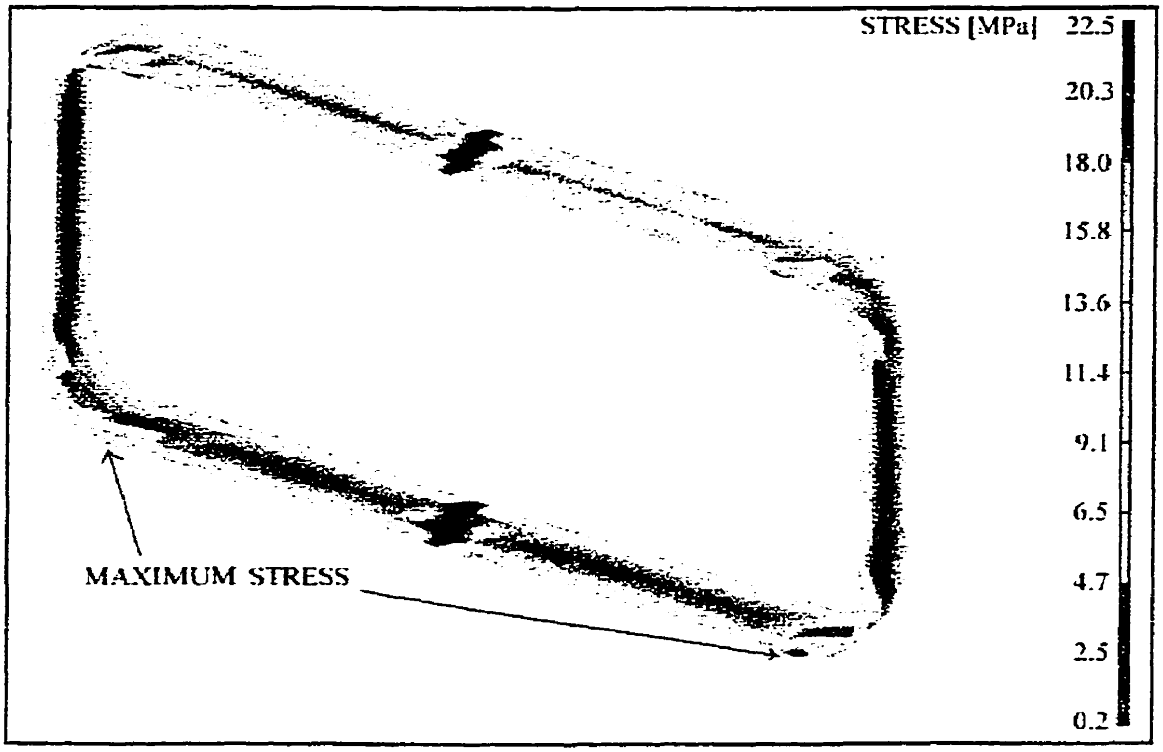

Figure 4.28: Von Mises Stress Contours in the Adhesive Bond

Manufacturer	Type	Tensile Lap Shear Strength (MPa)
Hysol	EA 9412	27.6
Hysol	EA 9430	31.0
Hysol	EPK 0151	12.8

Loctite	Depend 330	18.6
Ciba-Geigy	Araldite AW 138/HV 998	16.7
Ciba-Geigy	Araldite AW 106/HV 953	27.4
Ciba-Geigy	Araldite AW 136/HV 994	23.5

Table 4.15: Survey of Epoxy Adhesives - Adapted from [95-97]

Clearly, by using the Hysol EA 9430 (which is highly recommended for bonding stainless steel to graphite/epoxy), a factor of safety of 1.4 is achieved. It should be noted that the cantilevered load of 3790 Newtons represents an absolute worst-case scenario and thus the bond is unlikely to be stressed to the 22.5 MPa calculated by the finite-element model. Figure 4.29 illustrates how the stainless steel end-fitting mates with a cutaway of the graphite/epoxy box-beam.

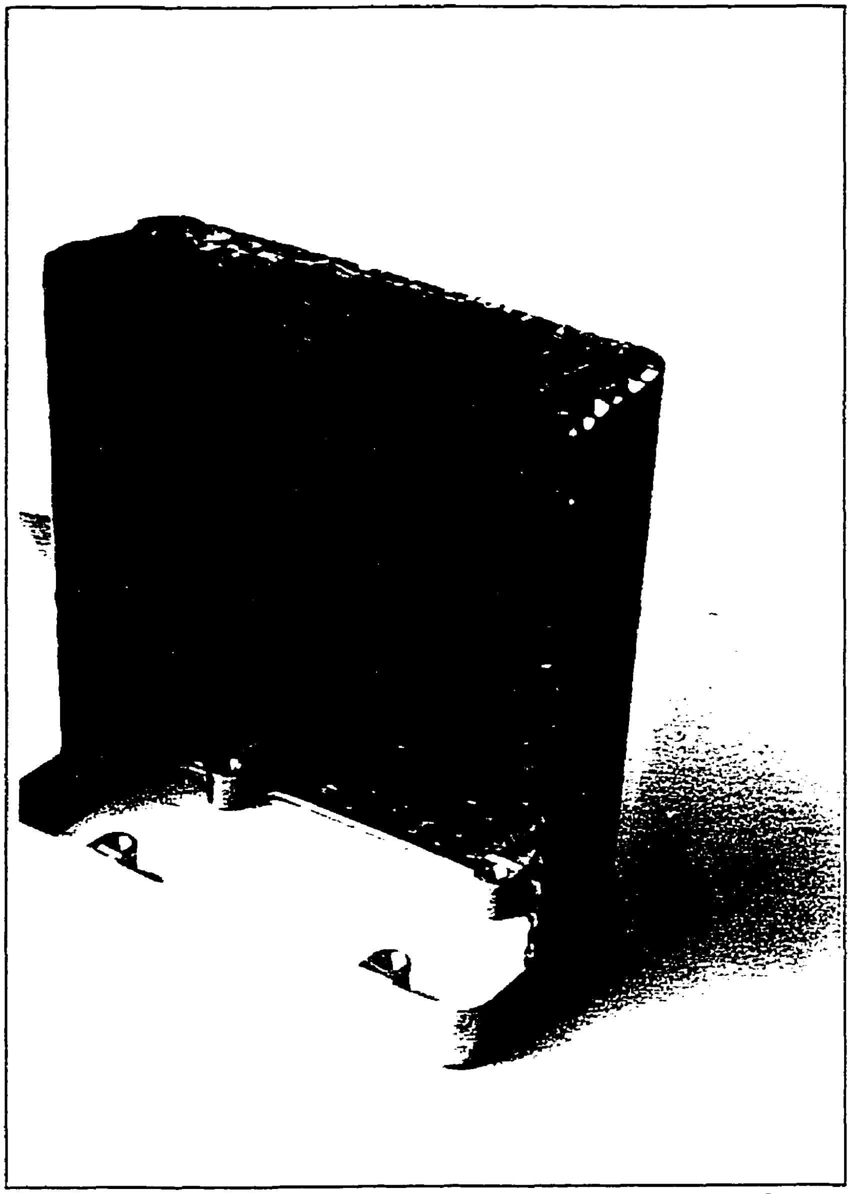

Figure 4.29: Stainless Steel End-fitting and Cutaway of Box-Beam

4.13 Stress Analysis of M6 Screws

There are four M6 hex-socket cap screws that fasten the SRC flange to the stainless steel end-fitting. As illustrated in Figure 4.30, the worst-case loading scenario for the M6 screws occurs when the shoulder exerts its maximum force of 3790 Newtons and the elbow is fully restrained.

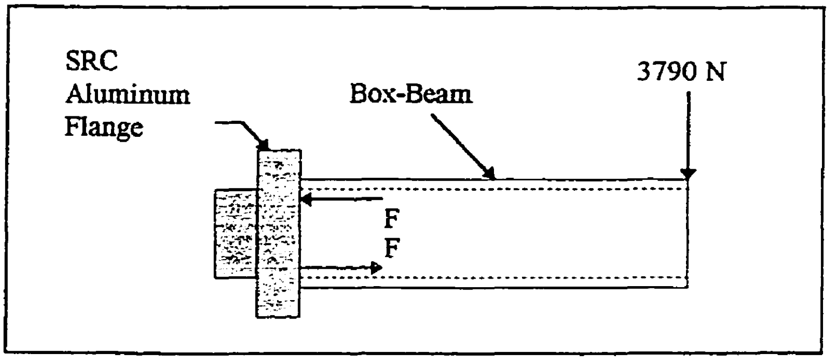

Figure 4.30: Cantilevered Loading of M6 Screws

The moment created by the end load of 3790 N has to be counteracted by the four M6 hex-socket cap screws that connect the box-beam's stainless steel end-fitting to the SRC shoulder flange. Mathematically, this moment equilibrium gives us the force, F, acting on the M6 screws. The top two screws are obviously in tension (if the end load is downward, as illustrated) while the bottom two screws are in compression.

$$M = (3790\,N)(0.315\,m) = 4F(45.9 \times 10^{-3}\,m) \tag{4.89}$$
$$\therefore F = 6502.4\,N \tag{4.90}$$

The tensile-stress area, A_t, of an M6 screw is 20.1 mm^2 (obtained from the mean of the pitch diameter and the minor diameter). Thus, the tensile (or compressive) stress in each M6 screw is:

$$\sigma = \frac{F}{A_t} = \frac{6502.4\,N}{20.1 \times 10^{-6}\,m^2} = 323.5\,MPa \tag{4.91}$$

In this application, the M6 cap screws are ISO-class 12.9, which are made from quenched and tempered alloy steel with a minimum proof strength of 970 MPa and a minimum yield strength of 1100 MPa. The factor of safety guarding against the screws acquiring a permanent set is:

$$F.S. = \frac{970\ MPa}{323.5\ MPa} = 3.0 \tag{4.92}$$

The stainless steel end-fitting has been designed so that the elbow mechanism that it supports can be mounted on the SRC shoulder flange in three distinct configurations. In the primary (i.e. anthropomorphic) configuration, the direction of the elbow's rotation is aligned with the principal power axis of the shoulder (i.e. the "strong" direction that produces 3790 N). In the secondary and tertiary configurations, the elbow is mounted perpendicular to the principal axis (i.e. along the shoulder's "weak" direction) facing either left or right. That the arm can be assembled in these three configurations confers upon Lightarm a tremendous degree of versatility in terms of workspace.

4.14 Design of Main Shafts

Again the factors driving the design of these components were strength and weight. Although aluminum would have been an excellent material for this application, it unfortunately has poor wear characteristics when in contact with the hard steel of the needle roller bearings. Thus, hollow steel shafts were designed and the geometry of the part lent itself to straightforward, analytical stress analysis. Each shaft can be treated as a hollow beam of circular cross-section which is fully restrained at either end and loaded at two points by 1340 Newtons. The bending moment diagram and the variation of moment along the beam can be obtained from a standard text on strength of materials [98].

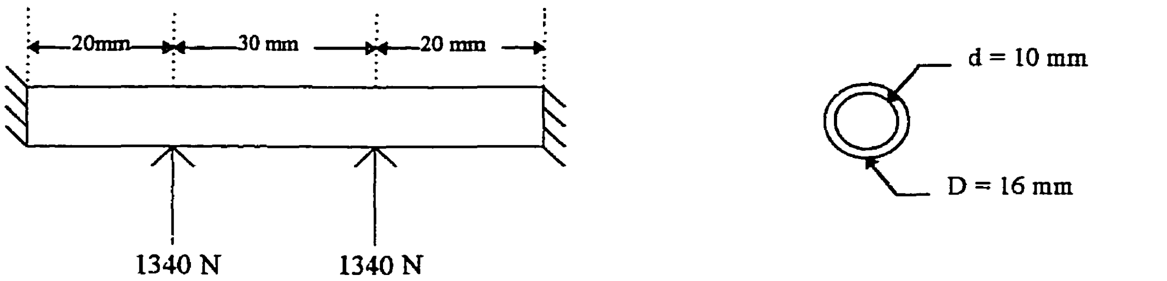

Figure 4.31: Dimensions of Main Shaft

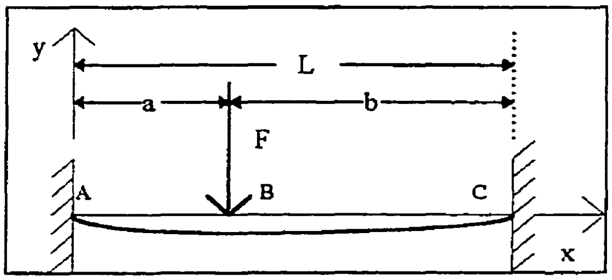

Figure 4.32: Beam Analysis

$$M_{AB} = \frac{Fb^2}{L^3}[x(3a+b) - aL] \tag{4.93}$$

$$M_{BC} = M_{AB} - F(x-a) \tag{4.94}$$

where

$$a = 0.02m \tag{4.95}$$

$$b = 0.05m \tag{4.96}$$

$$L = 0.07m \tag{4.97}$$

From the above expressions for the moment variation along the beam, bending moment diagrams can be readily drawn and then summed by applying the principle of superposition:

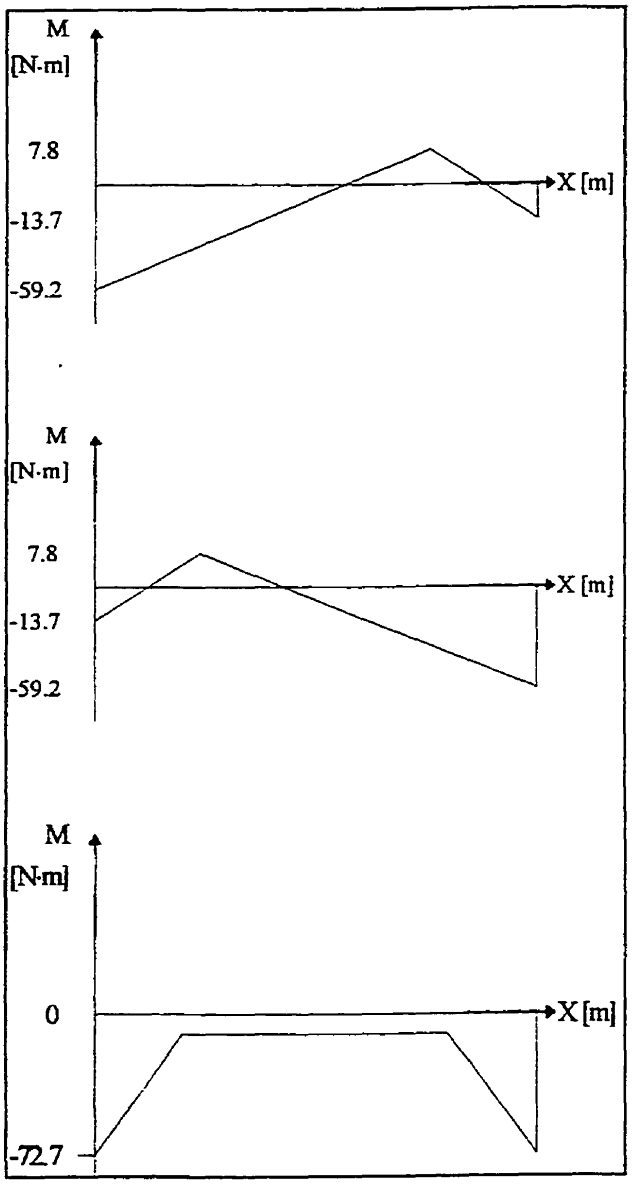

Figure 4.33: Summation of Bending Moment Diagrams

from which it is manifest that the largest moment acting is 72.7 N·m (at both ends of the shaft). Now, the stress due to bending can be calculated as follows:

$$\sigma_B = \frac{Mc}{I} \tag{4.98}$$

where

$$I = \frac{\pi}{64}(D^4 - d^4) \tag{4.99}$$

$$\therefore \sigma_B = \frac{64Mc}{\pi \cdot (D^4 - d^4)} \tag{4.100}$$

$$\therefore \sigma_B = \frac{64(72.7Nm)(0.008m)}{\pi \cdot [(0.016m)^4 - (0.010m)^4]} = 213MPa \tag{4.101}$$

The resulting factor of safety in yield is 1.6.

The shear stress can be obtained by first drawing the corresponding shear diagram, shown in Figure 4.34.

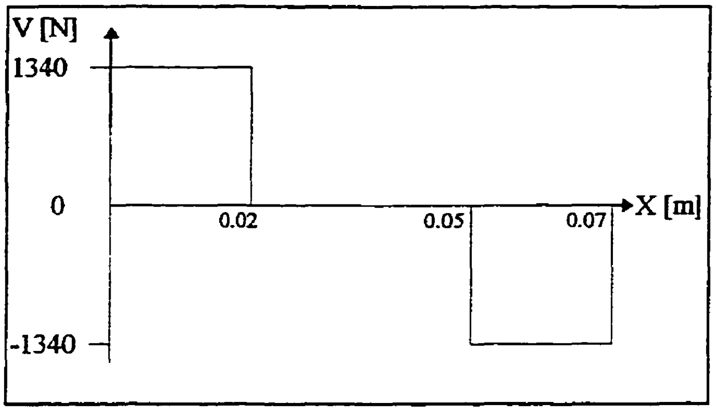

Figure 4.34: Shear Stress Diagram

Accordingly, the shear stress for this thin-walled member is given by the expression [99].

$$\tau = \frac{VQ}{It} \tag{4.102}$$

where V is the shear force, Q the first moment of the shaded area shown in the figure below, I the moment of inertia and t the width of the diametral cut. The centroid of a half cylindrical shell is shown below in Figure 4.35 [100].

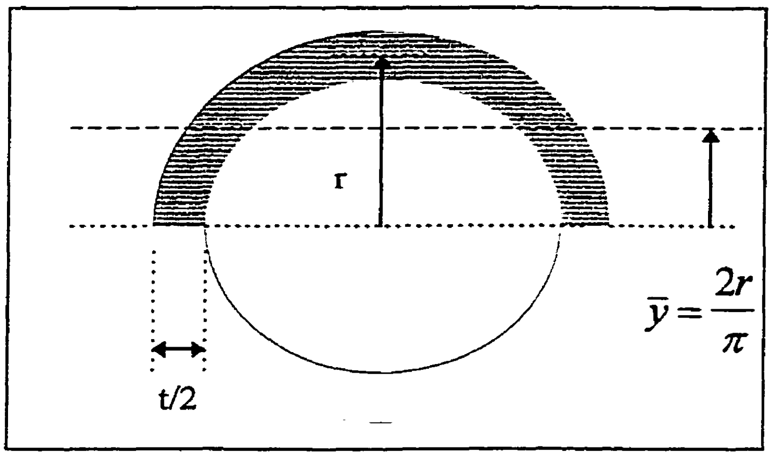

Figure 4.35: Centroid of Hollow Half-Cylinder

$$Q = A'\bar{y} \tag{4.103}$$

$$Q = \frac{\pi}{4}[(0.016m)^2 - (0.010m)^2]\cdot[\frac{2(0.065m)}{\pi}] \tag{4.104}$$

$$Q = 5.07\times10^{-7}m^3 \tag{4.105}$$

$$I = \frac{\pi}{4}[(0.008m)^4 - (0.005m)^4] \tag{4.106}$$

$$I = 2.73\times10^{-9}m^4 \tag{4.107}$$

$$t = 0.016m - 0.010m = 0.006m \tag{4.108}$$

$$\therefore \tau = \frac{VQ}{It} = \frac{(1340N)(5.07\times10^{-7}m^3)}{(2.73\times10^{-9}m^4)(0.006m)} = 41.5MPa \tag{4.109}$$

which results in a factor of safety of 4.9 against yielding in shear.

Next, we calculate the maximum deflection of the shafts to ascertain that they remain straight. Flexure of the shaft might impede the smooth running of the needle roller bearings. Intuitively, the maximum deflection occurs at the midpoint (x = 0.035 m). Again, by invoking symmetry and the principle of superposition, we can simply calculate the deflection at x = 0.035 m due to a single load and then double the result to obtain the total midpoint deflection. Referring to Figure 4.32, the deflection of any point x between points B and C is given by the following expression:

$$y_{BC} = \frac{Fa^2(L-x)^2}{6EIL^3}[(L-x)(3b+a)-3bL] \tag{4.110}$$

The midpoint deflection due to a single load is thus:

$$y_{BC}(x = 0.035) = \frac{(1340N)(0.02)^2(0.07 - 0.035)^2}{6(207 \times 10^9 Pa)(2.73 \times 10^{-9} m^4)(0.07)^3}[(0.07 - 0.035)(3(0.05) + 0.02) - 3(0.05)(0.07)]$$

$$y_{BC}(x = 0.035) = 2.6 \times 10^{-3} mm$$

$$\therefore y_{MAX} = 2 \times y_{BC}(x = 0.035m) = 5.2 \times 10^{-3} mm \qquad (4.111)$$

Evidently, the maximum deflection is so minute that it will not impede the free running of the needle bearings.

4.15 Bearing Selection

The two determining factors in choosing a bearing are obviously the dimensions and the load. For Lightarm, it was necessary to seek out small, compact bearings that were able to withstand large loads. Since the arm moves quite slowly, the maximum speed ratings are irrelevant. Also, the total number of cycles that the bearings will undergo will not likely approach the fatigue limit. Nevertheless, since the Lightarm manipulator is designed for long service use, it is prudent to select bearings with fatigue load limits that exceed the maximum load applied to the bearing. The first bearing type tabulated below is the INA K16X20X10 needle roller bearing, one of which is located in each of the three cam plates. Since these bearings are sold without an outer raceway, custom-machined steel raceways were inserted into the aluminum cam plates to protect the soft aluminum from the hard steel needles. The RNA 4901 needle roller bearings are slightly larger and stronger than the K16X20X10 and come mounted with outer raceways. Used in both bottom blocks (in the upper arm) as well as in the shoulder mechanism, the RNA 4901 is a strong yet compact bearing, far superior in that regard to ball bearings, for example which are strong but bulky. As a matter of fact, there are only three ball bearings used in the Lightarm manipulator, all of which are SKF Double-Row Angular Contact Ball Bearings. Although these possess a higher fatigue load limit than, say, the RNA 4901, they also weigh 2.5 times as much. The HK0408 TN drawn cup needle roller bearings, four of which are used in the shoulder's universal joint, are amazingly strong for their size. The dimensions of the HK0408 bearings were the limiting factors in the miniaturization of the shoulder's universal joint. Due to the very thin cup, the tolerances are critical. If the fit is too tight, the bearings don't roll properly on the shafts. Conversely, if the fit is too loose the bearings will slip out of their housings. To prevent slippage, a small amount of Loctite 648 cylindrical bond adhesive (with Primer 7649) can be applied. Tabulated below are data compiled and condensed from numerous bearing catalogs [101-104], wherein B, D and W represent bore, outer diameter and width.

Bearing Type	Designation	B (mm)	D (mm)	W (mm)	Applied Load (N)	Load Limit (N)	Safety Factor
INA Needle Roller	K16X20X10	16	20	10	893	1160	1.3
Drawn Cup Needle Roller	HK0408 TN	4	8	8	316	1320	4.2
INA Needle Roller	RNA 4901	16	24	13	1340	1460	1.1
SKF Double-Row Angular Contact Ball	5201 A	15.9	32	12	1876	10600	5.7
Torrington Needle Roller	B-44	6.35	11.11	6.35	670	1451	2.2
INA Needle Roller	HK0810	8	12	10	1340	3690	2.8

Table 4.16: Bearing Data

Bearing Designation	Unit Mass (g)	Quantity Present	Subtotal (g)
K16X20X10	5.7	3	17.1
HK0408 TN	1.6	4	6.4
RNA 4901	20	8	160
5201 A	50	3	150
B-44	2.3	8	18.4
HK0810	3	2	6
Grand Total			357.9

Table 4.17: Breakdown of Bearing Masses

4.16 Synthesis of Elbow Cam Mechanism

The objective in redesigning the elbow mechanism was to improve the strength-to-weight ratio while retaining the kinematic parameters of the previous design [105]. The new design includes a radically smaller cam mechanism, smaller bottom blocks and smaller bearings. In the previous design, the hydraulic lines were routed internally which meant that the wall thickness of the upper arm had to be large. Elegant as the internal routing was, the increase in complexity, machining cost and weight proved to be problematic.

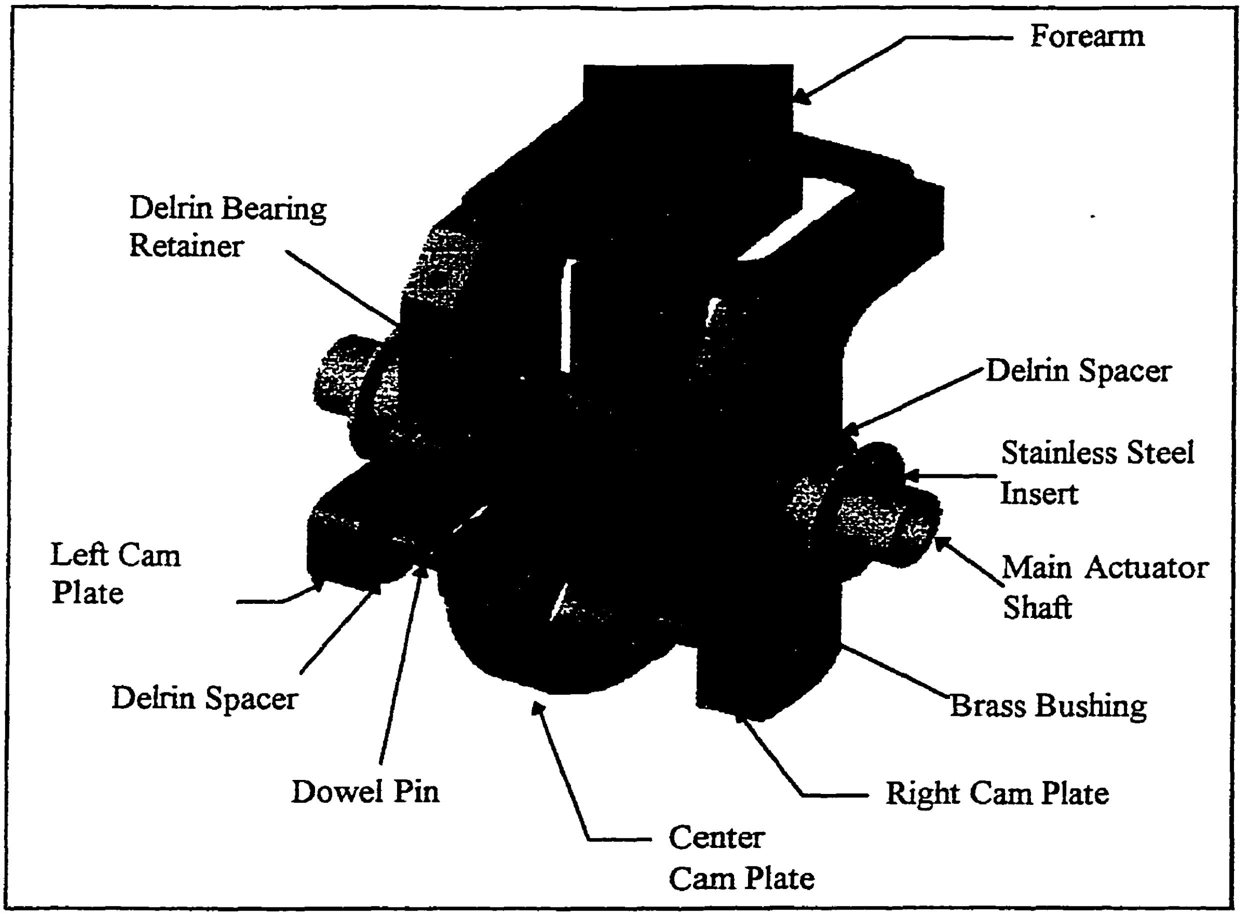

Figure 4.36: Anatomy of the Elbow Cam Mechanism

Additional weight savings were achieved by replacing the aluminum limit-stops with Delrin ones. The four black Delrin stoppers were bonded to the graphite/epoxy with Loctite 401 (possessing a tensile lap shear strength 22 MPa) and Loctite Primer 770. To cushion the small impact load of the cam mechanism on the four stoppers, small foam pads were fixed to the parts of the cam mechanism that come into contact with the stoppers. The foam pads were fastened with M3 hex-socket cap screws so that the thickness of the pads could be adjusted to ensure that both pads contact the stoppers equally.

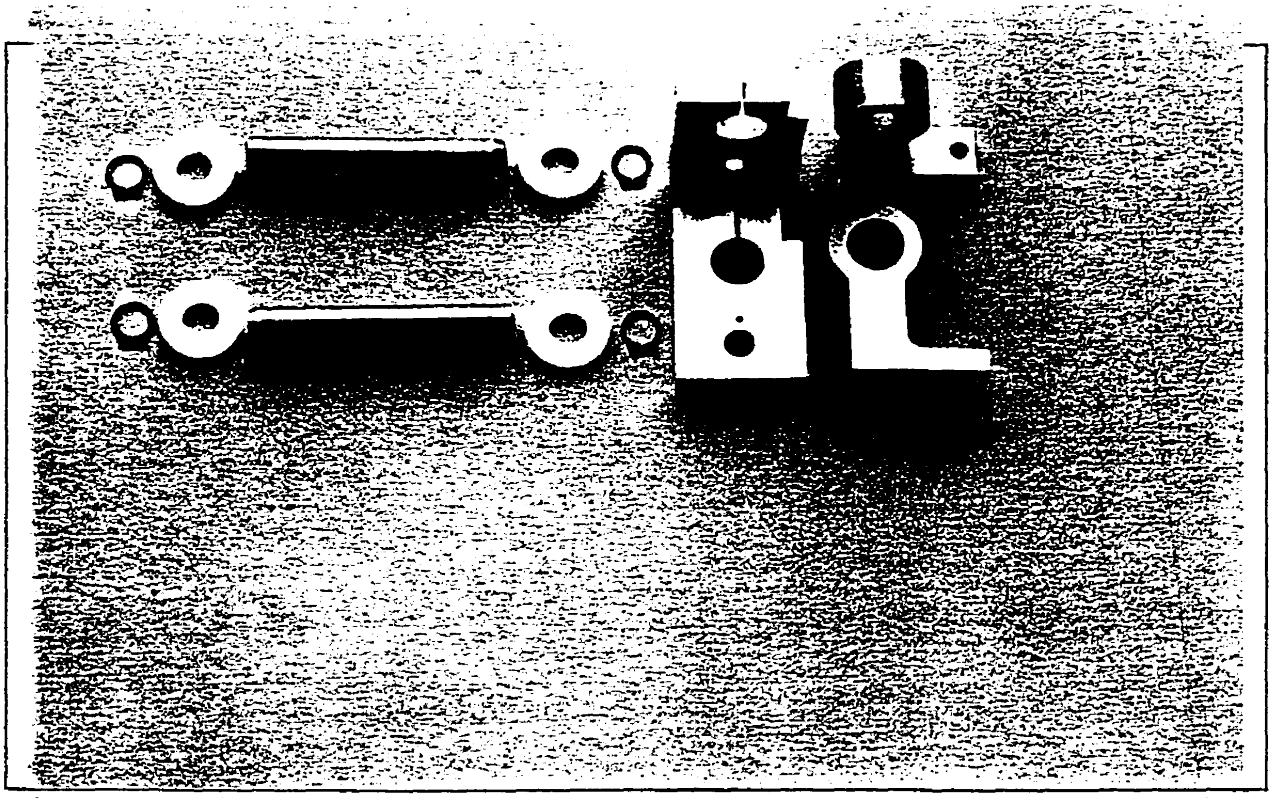

Figure 4.37: Elbow Components: retaining rings, Delrin spacers, dowel pins LVDT holder units and elbow output linkages.

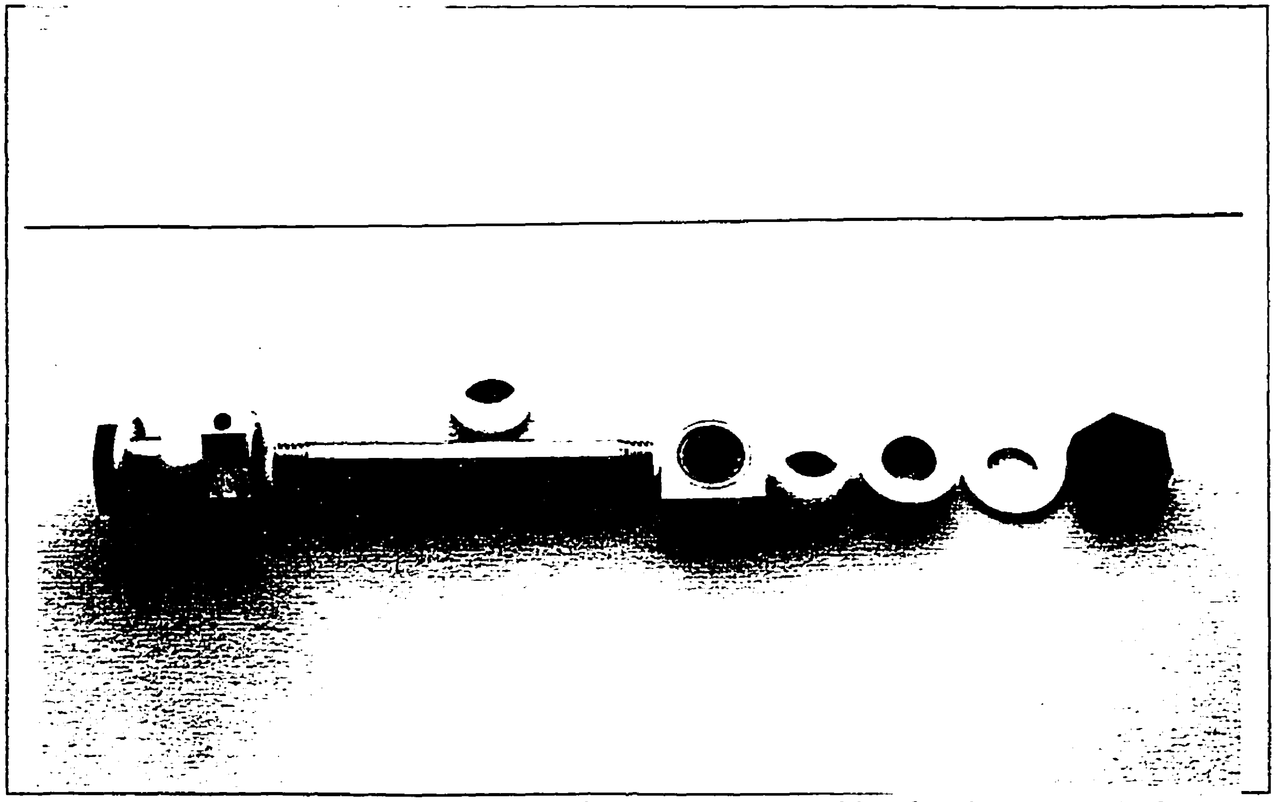

Figure 4.38: Components of Bottom Main Actuator Assembly, showing Main Shaft, Bearing Blocks, Delrin Spacers, Stainless Steel Inserts and Black Delrin M16 Nuts.

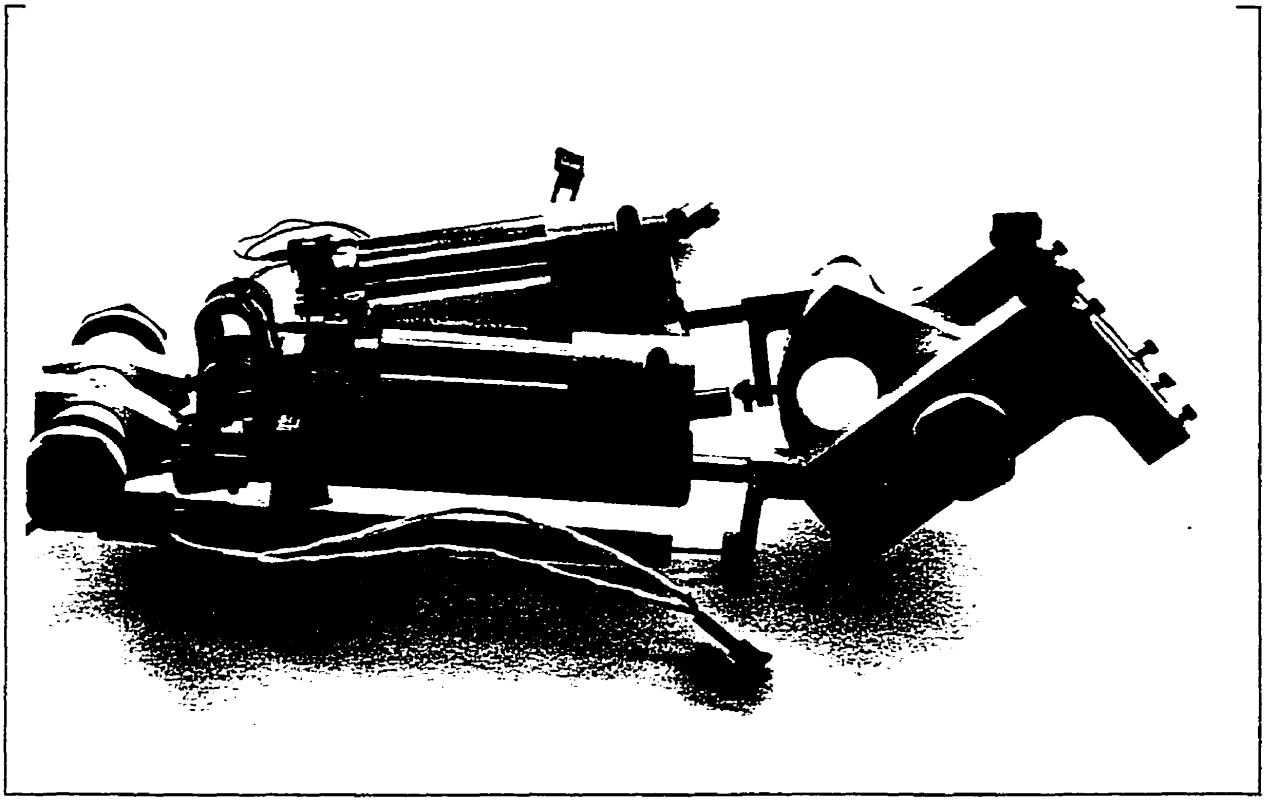

Figure 4.39: Assembled Elbow Mechanism

Chapter 5

Wrist/Forearm

5.1 Design of Forearm

The forearm, which links the wrist to the elbow, has to be strong enough to resist the loads applied to the arm yet light enough that it does not add unnecessary inertia to the manipulator. Due to the intricate nature of this component, shown in the figure below, Aluminum 6061-T6 is ideal for this application because it is strong, light and easily machined. Since the load at the end-effector has been estimated to be 400 Newtons, the moment that acts over the lever arm of 0.3 meters (the approximate distance from the base of the forearm to the end-effector) is 120 Newton-meters. In the finite-element model shown below, the left-most face of the base of the forearm is clamped (i.e. fully restrained in x,y,z translation and rotation). The cantilevered model provides a worst-case scenario for the component, assuming incorrectly that the rest of the arm is perfectly rigid. In reality, the forearm is never completely restrained because any load on the end-effector (e.g. payload) induces deflections not only in the forearm but also in other elastic components of the arm. Secondly, the twin actuators of the upper arm can only generate a maximum moment of 70 Newton-meters. This means that in practice a large load that incurs a moment in the forearm that exceeds 70 Newton-meters will cause some displacement of the actuators, in effect overpowering the actuators' moment. That the imposed boundary conditions represent a worst-case scenario has been belaboured here because the resulting safety factors for the forearm are rather miminal and are substantially lower than the safety factors that are typically considered prudent, especially for a component that undergoes repeated loading and for which some degree of material strength degradation is expected.

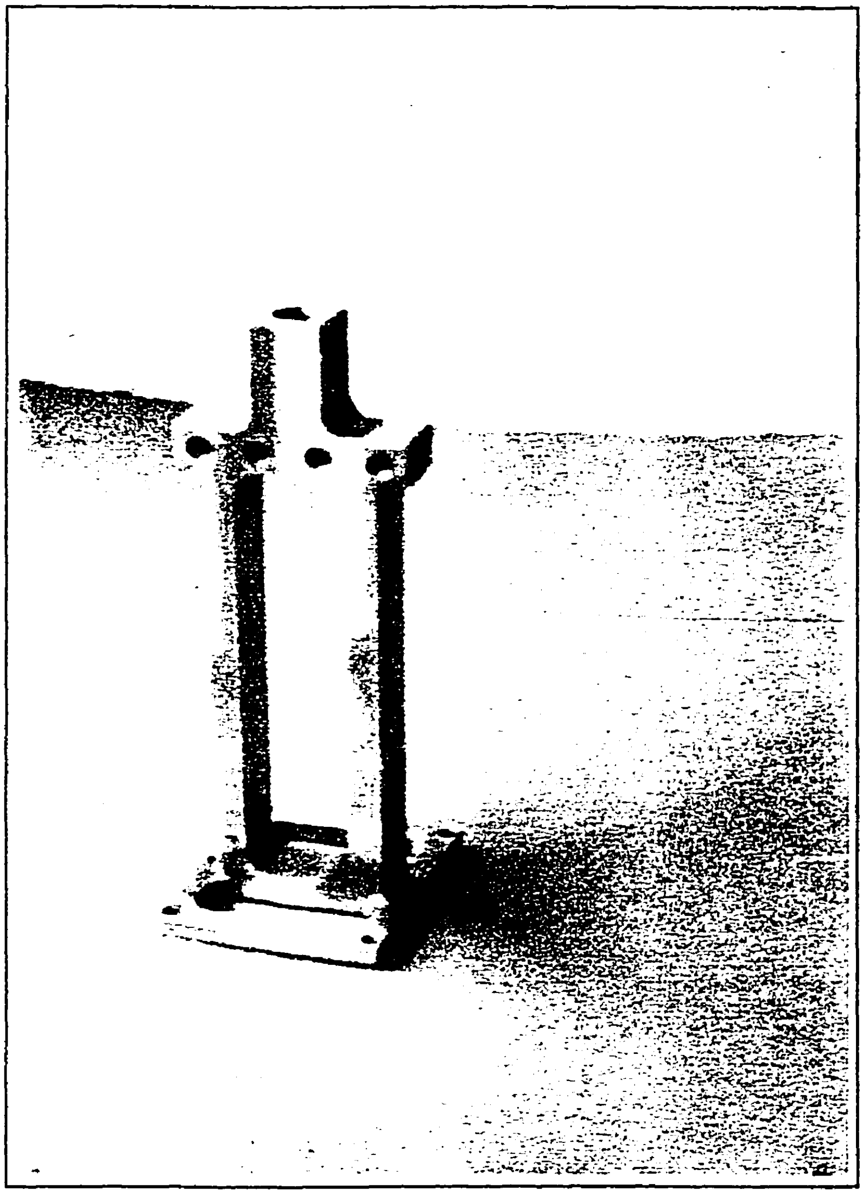

Figure 5.1: Forearm

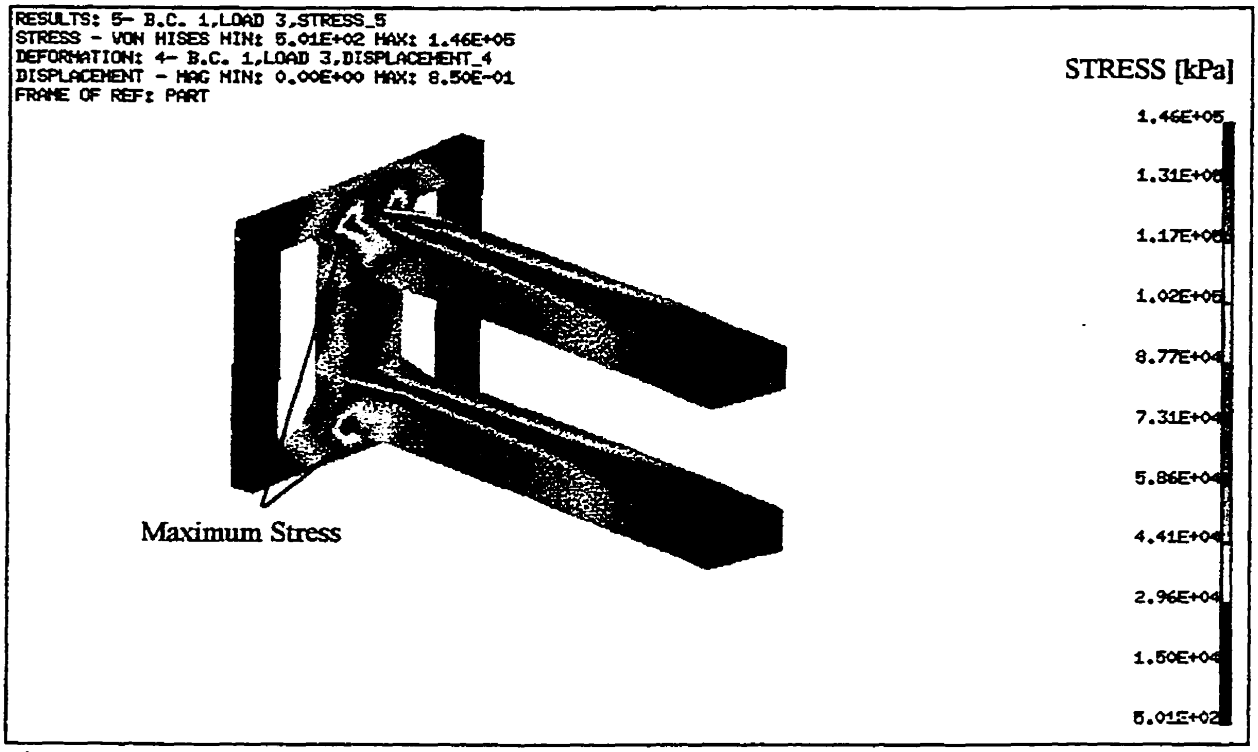

Figure 5.2: Von Mises Stress Contours on Forearm During Transverse Load

Figures 5.2 and 5.3 show the results of the stress analysis of the forearm. Clearly, the downward load case (shown in Figure 5.3) is more severe than the transverse load case (shown in Figure 5.2). The maximum deflection of 2.41 mm represents nearly a quarter of the maximum allowable end-effector static deflection of 1 cm. In terms of strength, the minimum factor of safety is 1.3.

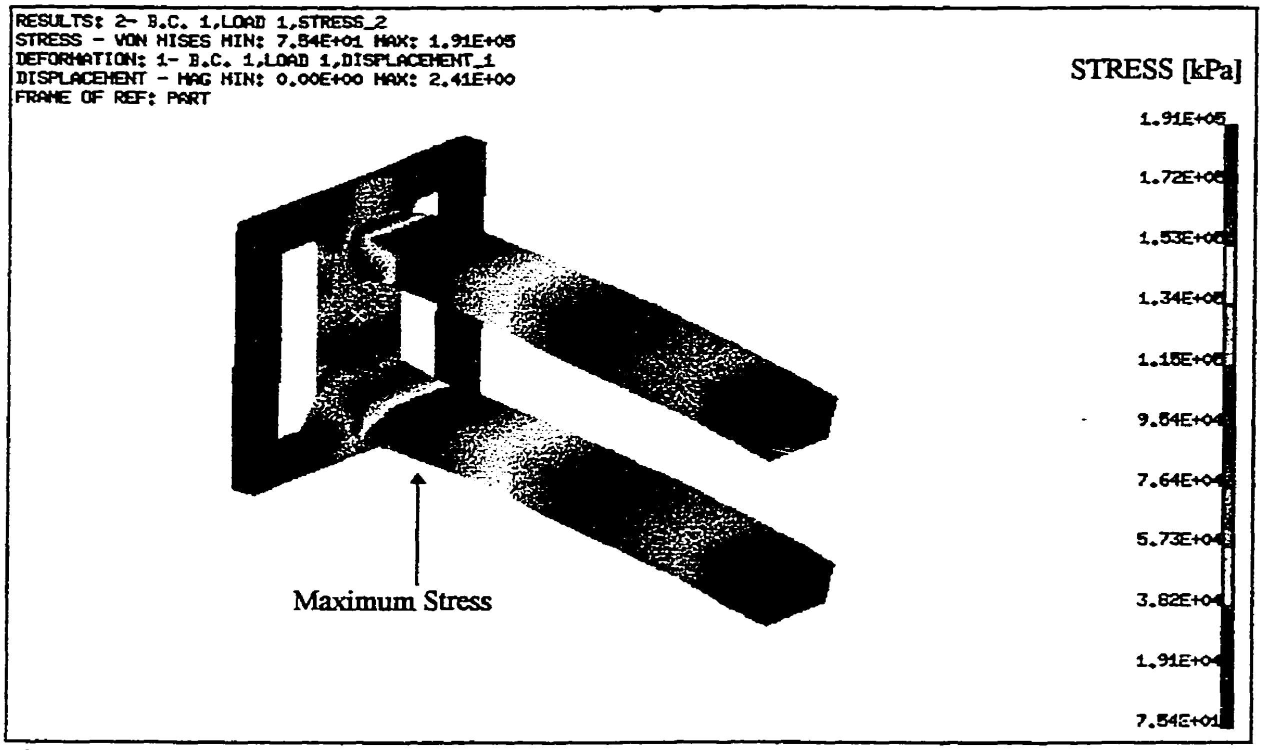

Figure 5.3: Von Mises Stress Contours on Forearm During Downward Load

Since the forearm is fastened to the cam plates of the elbow mechanism, the small M3 screws must withstand the loads induced by the application of 400 Newtons at the end-effector. The load on each of the six M3 screws can be calculated by considering the following diagram:

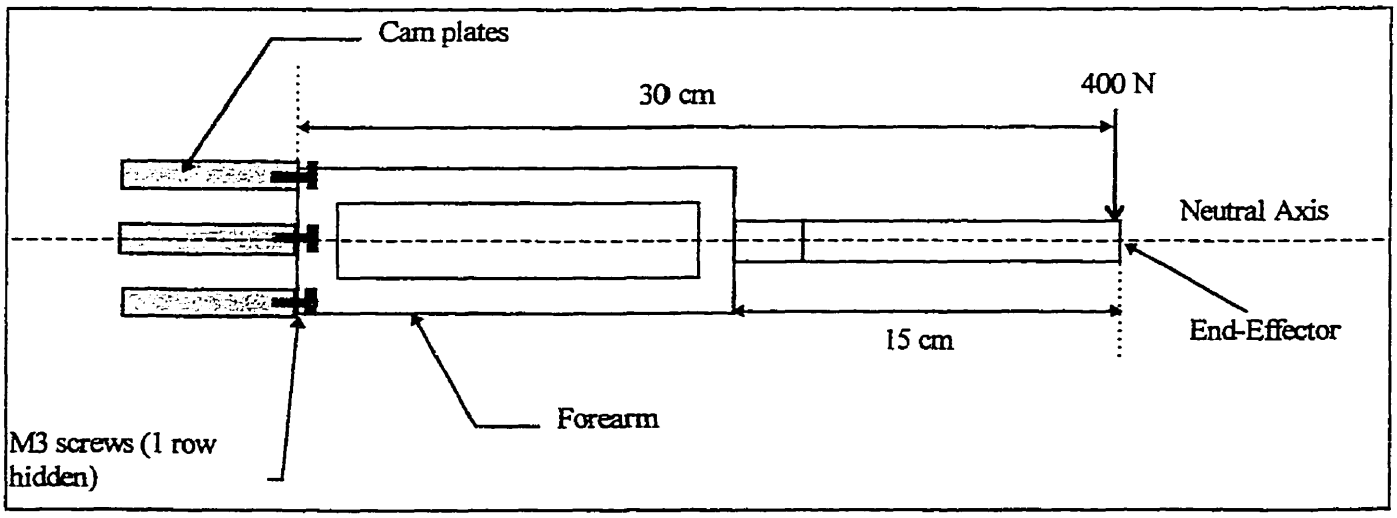

Figure 5.4: Load Analysis for Forearm's M3 Screws

In shear, the load on each screw is simply one-sixth of 400 N, or 66.7 N. Thus, the shear stress on each M3 screw is given by the load F divided by the minor-diameter area which for an M3 is 4.47 mm^2:

$$\tau = \frac{F}{A} = \frac{66.7\,N}{4.47 \times 10^{-6}\,m^2} = 14.9\,MPa \tag{5.1}$$

The moment induced by the maximum end load is counterbalanced by the two screws above the neutral axis and by the two screws below the neutral axis. Obviously, the two screws that lie on the neutral axis do nothing to counterbalance the moment created by the end load because their lever arm is zero. Thus, the tensile (or compressive) force, F, acting on the four off-axis screws is computed from the following moment balance:

$$(400\,N)(0.3\,m) = 4F(0.027\,m) \tag{5.2}$$

$$F = 1111\,N \tag{5.3}$$

The tensile (or compressive) stress can be readily computed using the tensile-stress area for an M3 screw, 5.03 mm^2:

$$\sigma = \frac{F}{A_t} = \frac{1111\,N}{5.03 \times 10^{-6}\,m^2} = 221\,MPa \tag{5.4}$$

The strength of a steel bolt, screw or stud is determined by the ISO mechanical property head marking. In the absence of head markings or appended documentation, it is prudent to assume that the screws were made from the lowest grade steel. However, the M3 is not available in the ISO 4.6 which ranges from M5 to M36. The ISO 4.8 M3 has a minimum proof strength of 310 MPa and a minimum yield strength of 340 MPa, providing a factor of safety of 1.4 against acquiring a permanent set and a factor of safety of 1.5 against yielding. Although it is best to err on the side of caution, the M3 screws resemble the M5 ISO 12.9 screws in both colour and texture. In all likelihood, the M3 screws are also ISO grade 12.9 with a minimum proof strength of 970 MPa and a minimum yield strength of 1100 MPa which provide factors of safety of approximately 5.

Since each of the four loads of 1111 Newtons is applied to the base of the forearm over a very small area, there is also a likelihood of local yielding around the holes. By invoking St. Venant's Principle [106], the area around a screw-loaded hole was analyzed using finite-element analysis. The area around one such hole was analyzed and the stress contours are shown below.

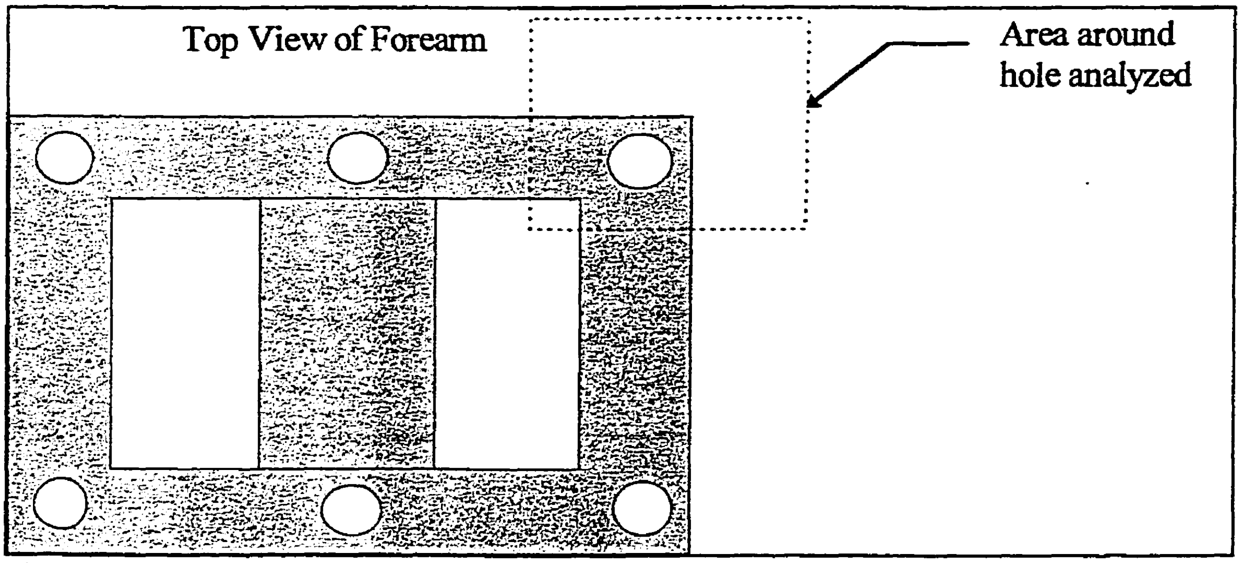

Figure 5.5: Determination of Local Yielding around Hole Region

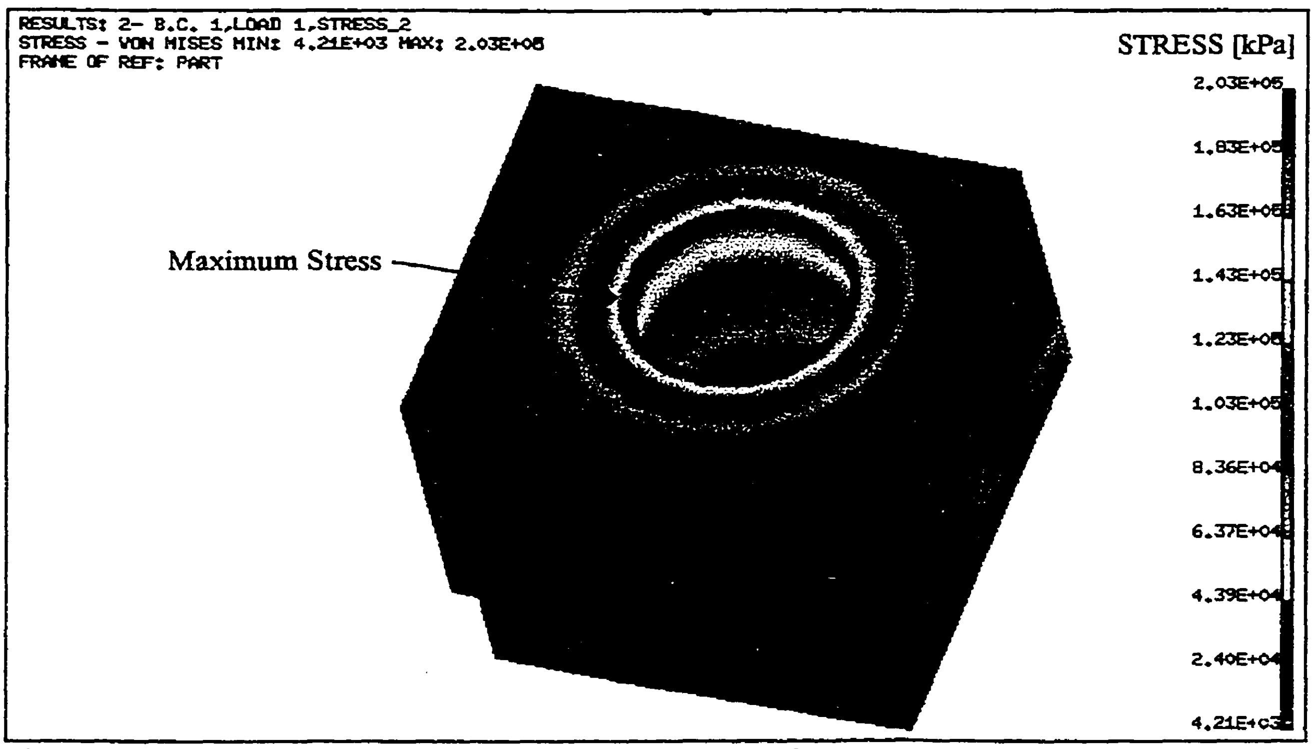

Figure 5.6: Von Mises Stress Contours around Hole Region

The maximum Von Mises stress reaches 203 MPa which affords the part a factor of safety of 1.2 against local yielding.

5.2 Design of Wrist

Figure 5.7 shows the main components of the forearm and wrist. The four Animate Systems Incorporated (ASI) valves on the right of the figure regulate.the flow of hydraulic fluid through their respective manifolds and into the four small actuators that are visible on the wrist. Shown on the left in Figure 5.8 is the fully assembled wrist and forearm unit and on the right is the forearm mounted with the wrist's four actuator valves. Although these valves contribute a great deal of inertia to the Lightarm manipulator, they are located on the forearm because that minimizes the length of the hydraulic lines running from the valves to the actuators on the wrist. Had the valves been located on the base, there would have to be long hydraulic lines running up to the wrist. Not only does this create problems routing the lines through the elbow mechanism but it introduces undesirable line dynamics which, in turn, complicates the control system. The kinematic optimization of the wrist was done by Kurtz [107]. A first kinematic prototype was built by Habib and Kee [108] and the first fully-working prototype was realized by four undergraduate students, Chevalier et al. [109].

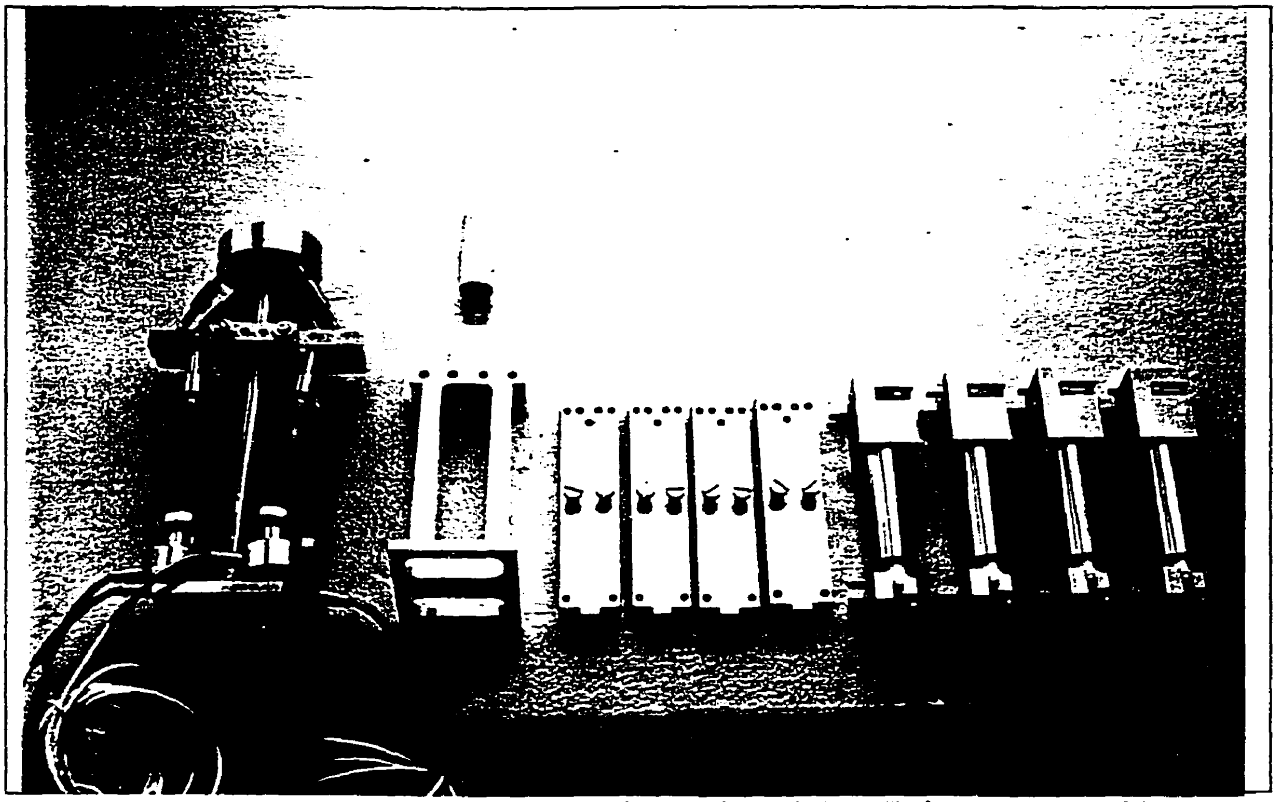

Figure 5.7: Components of Wrist/Forearm (from left to right): Wrist, Forearm with Adapter (above), ASI manifolds (modified), and ASI hydraulic valves.

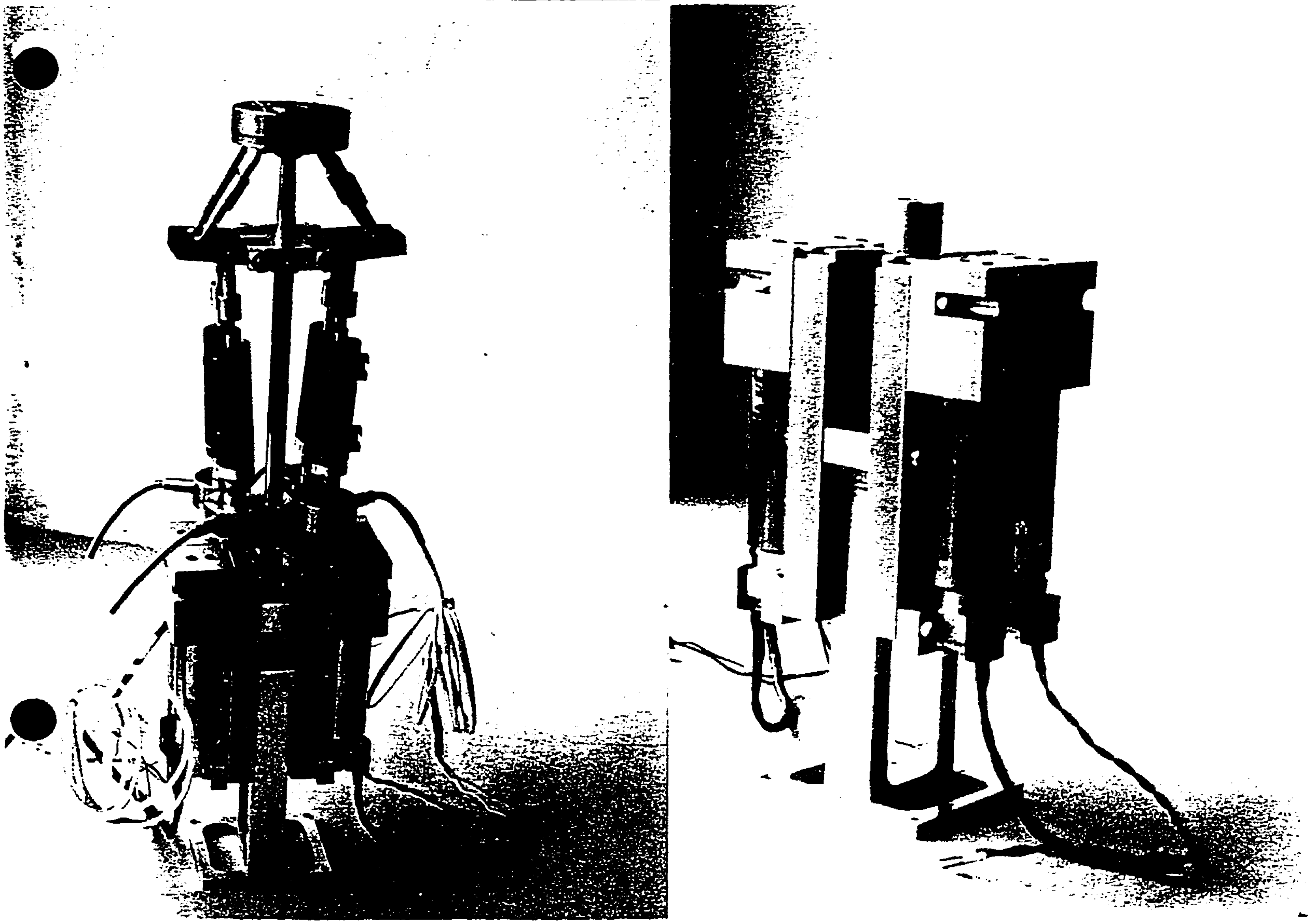

Figure 5.8: Wrist and Forearm Assembly

5.3 Selection of Gripper or Hand

For Lightarm to perform elementary teleoperated manipulations, a commercial gripper would have to be attached to the wrist's output flange. There are many types of grippers available on the market today: pivoting-arm grippers, parallel grippers with T-slots, parallel grippers with rack and pinion, cam-activated parallel grippers, finger grippers, 3-jaw grippers, 6-finger grippers, collet grippers, sheet stock grippers, indexers, toggle-tongs, suction cups, needle grippers, magnetic grippers, wide-jaw grippers and tube grippers [110]. These grippers can be combined with tool changers to allow the teleoperator to remotely select and pick different tools during a procedure. Also available are swivel units which could endow the wrist with a fourth degree of freedom to, say, perform a rotary task [111,112]. These accessories allow Lightarm to perform rudimentary tasks such as manipulating tools. For more intricate operations, a robotic hand would be necessary. There are numerous anthropomorphic robotic hands currently on the market. The Hitachi Hand uses shape memory alloy (SMA) actuation but unfortunately it has a mere load capacity of 2 kg, weighs 4.5 kg and is 70 cm long. The Utah/MIT Hand employs a tendon-drive system involving 288 pulleys. Its length makes it unsuitable for Lightarm. The same can be said for the Jameson tendon-driven hand. Although the Belgrade/USC appears to be the appropriate size, it is only capable of holding a mass of 2.2 kg which is lower than the 10 kg payload envisioned for Lightarm. The Sarcos Hydraulic Hand has a 22.7 kg load capacity as well as impressive dexterity. Unfortunately, the Sarcos Hand is too heavy and bulky and it runs at 3000 psi (20.7 MPa) whereas Lightarm's ASI actuators operate at only 500 psi (3.45 MPa). The Odetics Hand is a simple, three-fingered, human-sized hand which is powered by electric motors and solenoids. It possesses rudimentary kinematics that are more akin to a claw or talon than a hand but the Odetics Hand appears to be a feasible hand for Lightarm. Should a more dextrous hand be sought, there are two which were featured in Chapter 2, the Barrett Hand and the Omni-Hand. The Barrett Hand weighs only 1.1 kg and is roughly the size of a human hand. It consists of a thumb and two fingers, complete with built-in position and force transducers. But unfortunately, the maximum payload is only 5 kg which is half of what was originally prescribed for Lightarm. The Ross-Hime Designs Incorporated Omni-Hand is a truly human-like hand with a load capacity of 25 pounds (11.4 kg) which is ideal for Lightarm's expected maximum payload of 10 kg. Omni-Hand, which is controlled by electric servos and even features tactile sensors in the fingers and palm, represents the state of the art in robotic hands.

Chapter 6

Synthesis of Lightarm

6.1 Final Assembly

Shown in Figure 6.1 are front and side views of the fully assembled Lightarm. In Figure 6.2 are three additional views of Lightarm, showing the slot in the box-beam and the elbow bent to its maximum angle. Each major mechanism, namely the shoulder, elbow, and wrist, is modular and can be rapidly assembled and disassembled which is highly advantageous for maintenance and repair. Similarly, each actuator/valve is a modular unit which can also be easily replaced.

Although the wires and hydraulic lines have not yet been fully integrated, the elbow, forearm and shoulder were carefully designed to accommodate these wires and lines. The hydraulic lines for the elbow and wrist will be routed through the holes in the SRC flange and the stainless steel end-fitting and will be affixed to the inner wall of the graphite/epoxy box-beam. A full centimeter of clearance has been left expressly for this purpose. As shown in Figure 6.1, the black Delrin cap on top of the graphite/epoxy box-beam was modified to fit the slot and bonded with Loctite 401 and Primer 770. The Delrin inside the slot acts as a bumper for the forearm when the elbow joint is fully contracted, as shown in Figure 6.2, and thus prevents damage to the top edge of the graphite/epoxy box-beam.

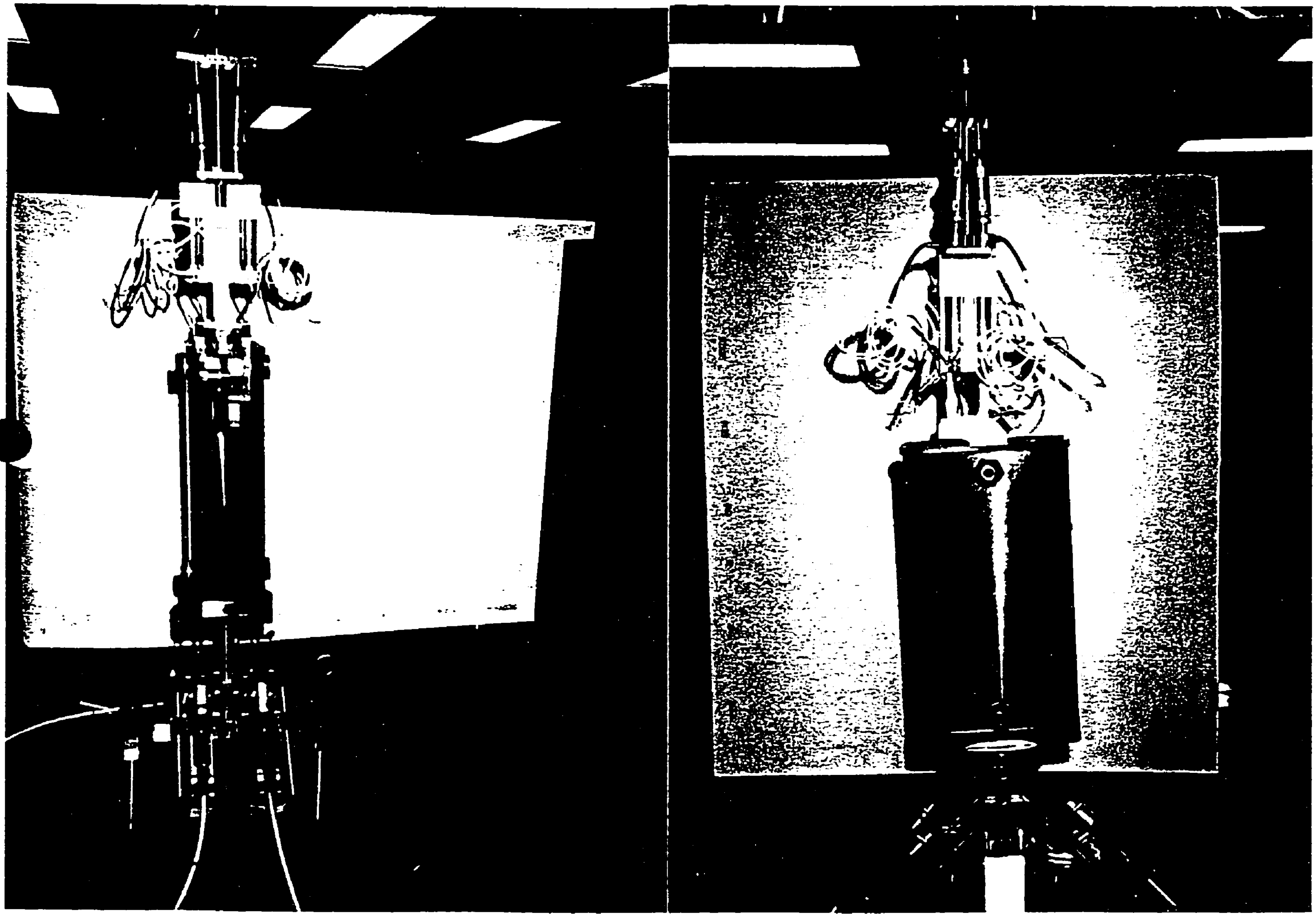

Figure 6.1: Front and Side Views of Lightarm

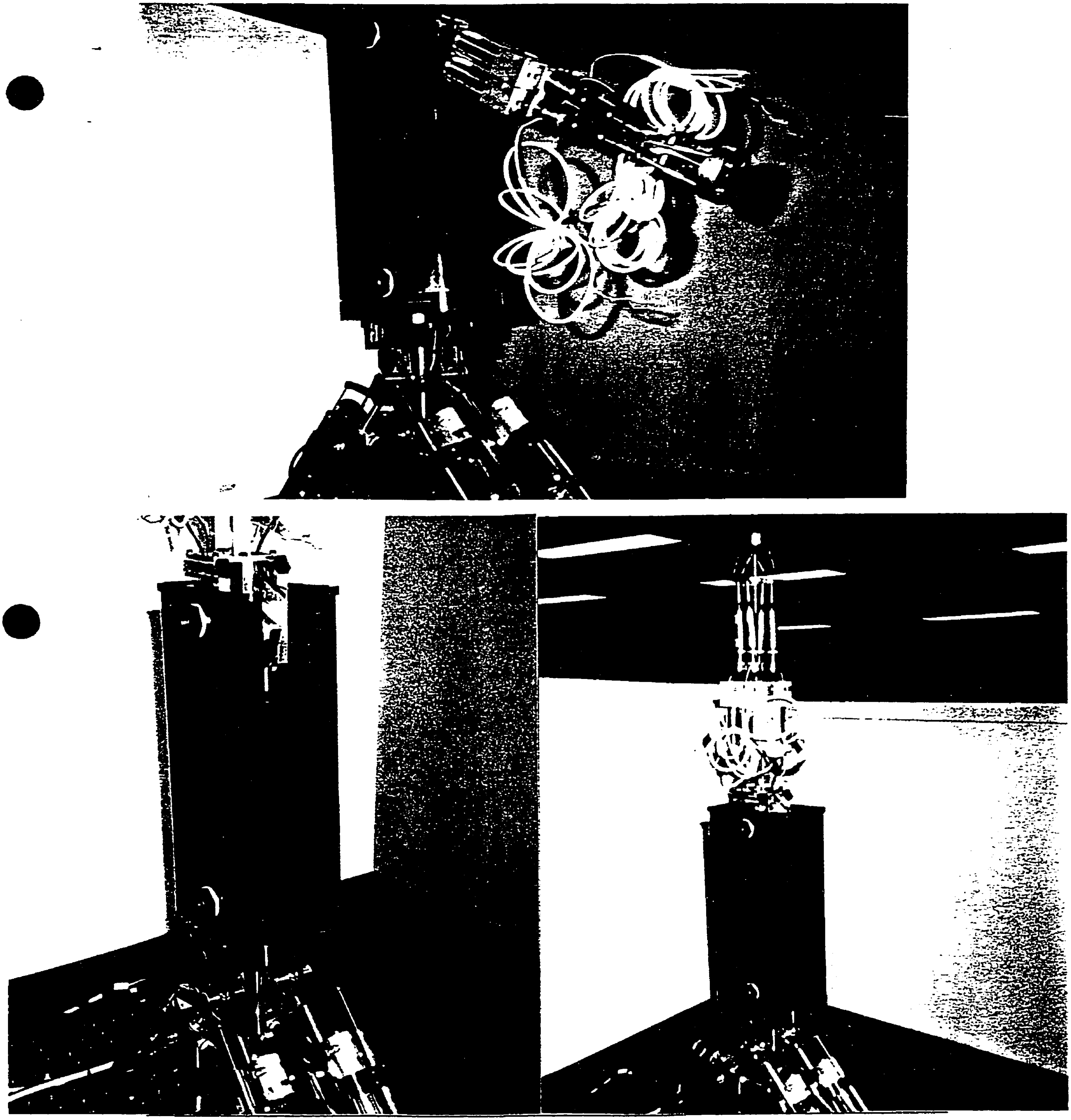

Figure 6.2: Views of Lightarm

6.2 Evaluation of Mass and Inertia

Tabulated below is a breakdown of the masses of each major mechanism. The total mass of Lightarm (shoulder, elbow and wrist/forearm) is currently 5660 g. If we add to that the mass of a hand/gripper like Barrett Hand, the total mass of Lightarm would rise to 6.76 kg which is considerably less than the payload of 10 kg. However, the Barrett Hand cannot grip more than 5 kg so it would be necessary to employ a different (and possibly a heavier) hand or gripper. For that reason, 2.5 kg is budgeted as a conservative estimate of the mass of such a hand, resulting in a total of 8.16 kg which is still less than the payload of 10 kg. Even with that hypothetical 2.5 kg hand, the payload-to-weight ratio would be 1.22:1 which is superior to the 1:1 ratio which was established as a benchmark for lightweight manipulators by ROTEX. The payload-to-weight ratio can still be improved, however. By relocating the wrist's four ASI valves to the base, a full 1 kg can be saved. By redesigning the wrist with aluminum instead of brass and steel, at least 300 g could be economized. Finally, a lightweight hand capable of lifting 10 kg could be designed or purchased. Presuming the hand had a mass of 1.5 kg, the overall mass savings would be 2.3 kg. The total mass of Lightarm would therefore be 5.86 kg, resulting in a truly remarkable payload-to-weight ratio of 1.7.

Mechanism/Component	Mass
Shoulder[1]	1000 g
Elbow	2465 g
Forearm	1193 g
Wrist	1002 g
TOTAL (without hand)	**5660 g**
Gripper/Hand[2]	2500 g
TOTAL (with hand)	**8160 g**

Table 6.1: Mass Summary

[1] equivalent moving mass of shoulder

[2] mass of Barrett Hand

Although the payload-to-weight ratio of the arm is a significant measure of the performance of an arm, a more rigorous approach is to quantify the inertia of the arm, or the distribution of mass with respect to the kinematic origin of the manipulator. For the sake of simplicity, the kinematic origin is taken to be at the center of the shoulder mechanism's universal joint. Using I-DEAS Master Series 2.1, the inertia matrices of the various links of the arm assembly were calculated in the X-Y-Z coordinate system shown below. The inertia of the arm changes as the arm's posture changes. For the sake of illustration, the moment of inertia of the arm is calculated for the full-extended vertical posture which is essentially when the arm is working at a worst possible mechanical advantage. The payload is assumed to be the maximum 10 kg and the gripper is presumed to have a mass of 2 kg.

$$[I] = [I]_{SHOULDER} + [I]_{ELBOW} + [I]_{FOREARM} + [I]_{WRIST} + [I]_{HAND} + [I]_{PAYLOAD} \tag{6.1}$$

$$[I] = \begin{bmatrix} 4871 & 0 & 0 \\ 0 & 86 & 0 \\ 0 & 0 & 4871 \end{bmatrix} + \begin{bmatrix} 174168 & 0 & 0 \\ 0 & 6211 & 0 \\ 0 & 0 & 170691 \end{bmatrix} + \begin{bmatrix} 289131 & 0 & 0 \\ 0 & 716 & 0 \\ 0 & 0 & 289131 \end{bmatrix} +$$

$$\begin{bmatrix} 411514 & 0 & 0 \\ 0 & 112 & 0 \\ 0 & 0 & 411514 \end{bmatrix} + \begin{bmatrix} 1999 & 0 & 0 \\ 0 & 1.02 \times 10^6 & 0 \\ 0 & 0 & 1.02 \times 10^6 \end{bmatrix} + \begin{bmatrix} 12003 & 0 & 0 \\ 0 & 6.15 \times 10^6 & 0 \\ 0 & 0 & 6.15 \times 10^6 \end{bmatrix} \tag{6.2}$$

$$[I] = \begin{bmatrix} 893686 & 0 & 0 \\ 0 & 7.18 \times 10^6 & 0 \\ 0 & 0 & 8.05 \times 10^6 \end{bmatrix} \; kg \cdot mm^2 \tag{6.3}$$

Thus, $I_{XX} = 0.9$ kg·m^2, $I_{YY} = 7.2$ kg·m^2 and $I_{ZZ} = 8.1$ kg·m^2. The radii of gyration for each of the various links can be found in Appendix B. The inertial results show that the wrist and the forearm (with the four ASI valves) contribute greatly to the overall inertia of the arm. In the fully vertical posture, illustrated in Figure 6.1, the inertia (I_{ZZ}) of the forearm and valves is 1.7 times the inertia of the elbow while I_{ZZ} of the wrist is 2.4 times that of the elbow. Similarly, the hypothetical addition of a gripper and a payload would contribute an even greater amount of inertia to the arm. This is a simple manifestation of the lever arm effect. In other words, the further a link is from the arm's kinematic origin, the more critical its mass becomes.

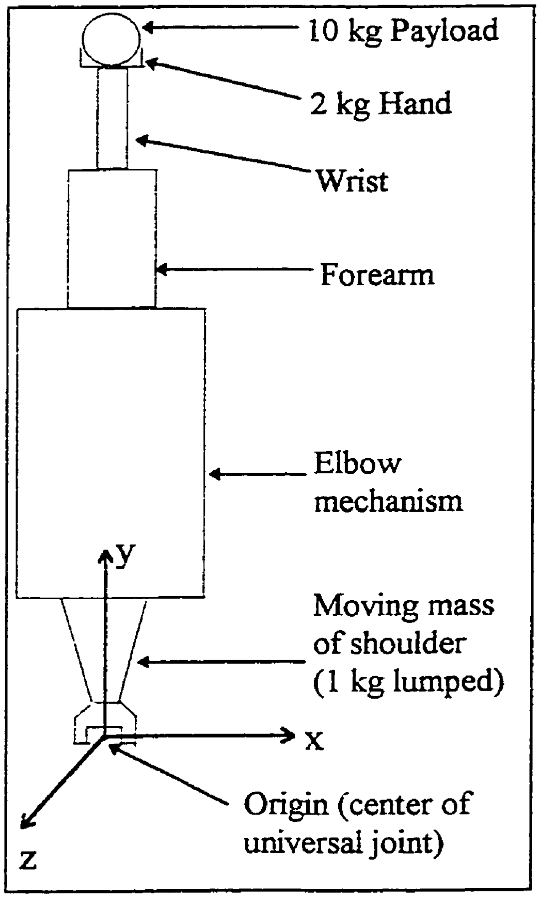

Figure 6.3: Main Links for Calculating Inertia

6.3 Summary of Stress Analysis

The material and safety factor of the most highly-stressed components of Lightarm are summarized in Table 6.2. With these safety factors, the strength-to-weight ratio of the various components can be considered optimal.

Part/Component	Material	Factor of Safety
Forearm	Aluminum	1.3
H-Base	Stainless Steel 304	1.7
Box-Beam	Graphite/Epoxy	2.2
Main Elbow Shafts	Stainless Steel 303	1.7
Centercube	Stainless Steel PH	1.9
End-fitting Bond	Hysol EA9430	1.4
M3 Cap Screws	Steel	5.0
M6 Cap Screws	Steel	3.0

Table 6.2: Material & Safety Factor Summary of Key Lightarm Components

6.4 Recommendations for Future Work

Ultimately, *two* Lightarm manipulators will be tele-operated simultaneously, thereby mimicking the full dexterity of a two-armed human. The simultaneous control of two arms has been the subject of much research [113-118], and, from a mechanical standpoint, raises the spectre of arm-to-arm collisions. Analysis of impact loads thus becomes critical in future two-arm designs [119,120].

Since the wrist prototype [109] did not perform kinematically as well as had been originally envisaged, a redesign is inevitable. Yet another alternative is to purchase a commercially available wrist such as the Omni-Wrist or the composite-material Barrett Wrist. Aside from the heavy ASI hydraulic actuators, the structure that contributes most to the inertia of the arm is the wrist since it is constructed predominantly of brass and steel, both of which have high densities. Thus, the engineers involved with the next wrist iteration should strive to lighten the mechanism dramatically. The choice of brass and steel arose out of a perceived need to find two materials that have very low wear when in contact with one another. However, the wear factor is not all that important because the wrist moves at slow speeds. A mainly aluminum structure would be substantially lighter and the problem of wear on the ball-and-socket joints could be solved by careful lubrication or by coating the sockets with a wear-resistant compound like Teflon. Plastics or ceramics might even provide better design solutions for the ball-and-socket joints.

Ultimately, the wrist and forearm should be shrouded to protect the actuators and valves from both impact damage as well as dirt, dust and rain. Although the forearm is sufficiently strong as is, the wrist/forearm shroud ought to be a structural member in order to take part of the load exerted on the wrist/forearm. This would reduce the load imposed on the forearm and further improve the factor of safety which is presently tenuous. The left and right cam plates have been tapped for M3X 0.5 screws at two places at the top of each plate for this purpose. These are the ideal lower attachment points for the shroud since they are high enough that the shroud would not interfere with the graphite/epoxy box-beam as the forearm pivots about the elbow. On the existing wrist, the shroud's upper attachment points (also threaded for M3 X 0.5) are located on the structure that restrains the rocker arms. This is the highest accessible non-moving part of the wrist but, regrettably, this leaves exposed the slender links that run from the rocker arms to the brass head, an issue which ought to be addressed in the next iteration. The shroud could be a fairly simple structure such as a box-beam, for instance, and should be very light. Either aluminum or graphite/epoxy could be used although the cost and effort associated with the design and fabrication of the latter may not be justified for such a minor part.

To further reduce the inertia of the arm, it would be possible to remove the ASI valves from the forearm/wrist and relocate them to the H-Base. This would, however, introduce line dynamics due to the hydraulics and would complicate the control. If the control problem could be solved, then hydraulic lines would have to be routed through the shoulder and elbow joints. In such a case, it would be advisable to return to the original design for the box-beam involving the ¼-inch honeycomb core through which the copper hydraulic lines could be routed.

There are three minor improvements that could be made to the graphite/epoxy box-beam. First of all, the surface finish (for final production) of the box-beam can be improved by grinding and honing the inner surface of the mold. Secondly, more detailed machining of the mold would eliminate the lines that appear at the seams of the mating parts. Thirdly, the width of the box-beam could be reduced by about 1 cm. If the elbow's actuator output linkages and LVDT holders are shortened by about 1 cm, then the width of the box-beam can be reduced by another 1 cm for a total reduction of 2 cm. The depth of the box-beam can be reduced only if the thickness of the Renshape inserts is reduced. In the extreme, the Renshape could be omitted (as it was for the tested box-beam) thereby cutting the depth of the box-beam by half an inch. Although these reductions in width and depth are by no means critical, they would simply render the elbow more compact, if ever another iteration were to be designed. Although it may be too complex for this particular application, a very interesting alternative design for a composite box-beam involving stringers, spars, ribs and cover sheets was presented by Bicos et al. [121].

6.5 Conclusion

A lightweight, anthropomorphic robotic arm was designed and fabricated using aluminum, stainless steel and graphite/epoxy to achieve a payload-to-weight ratio that exceeds 1.2 to 1. Dubbed Lightarm, this general-purpose, seven-degree-of-freedom, hydraulically actuated manipulator consists of three principal mechanisms: a shoulder, elbow and wrist/forearm. Each of these three mechanisms was optimized for strength, stiffness and low weight using finite-element analysis. The driving design criterion for the shoulder mechanism was range of motion. By designing a highly compact yet strong universal joint, the shoulder is able to achieve excellent motion. For the elbow mechanism, strength-to-weight ratio was paramount. A 400-gram graphite/epoxy box-beam houses the elbow's twin actuators. The elbow mechanism has a mass of only 2.3 kg which is substantially lighter than the previous aluminum prototype. The forearm and wrist were also designed for maximum strength and minimum weight. Together, the shoulder, elbow and wrist constitute a lightweight arm with remarkable payload, strength and stiffness as well as the manipulability, dexterity and workspace volume approaching those of a human arm.

References

1- Gordaninejad, F., Azhdari, A., and Chalhoub, N.G., "Nonlinear Dynamic Modelling of a Revolute-Prismatic Flexible Composite-Material Robot Arm", *Journal of Vibration and Acoustics*, October 1991, Vol. 113, pp. 461-468.

2- Cannon, R.H., and Schmidt, E., "Initial Experiments on the End-Point Control of a Flexible One-Link Robot", *The International Journal of Robotics Research*, Vol. 3, No. 3, November 1984, pp. 62-75.

3- Usoro, P.B., Nadira, R., and Mahil, S.S., "Control of Lightweight Flexible Manipulators: A Feasibility Study", *Proceedings of the 1984 American Control Conference*, Vol. 2, San Diego, California, 1984, pp. 1209-1216.

4- Chalhoub, N.G., and Ulsoy, A.G., "Control of a Flexible Robot Arm: Experimental and Theoretical Results", ASME *Journal of Dynamic Systems, Measurement, and Control*, Vol. 109, No. 4, December 1987, pp. 299-309.

5- Zalucky, A., and Hardt, D.E., "Active Control of Robot Structure Deflections", *Robotics Research and Advanced Applications* (Edited by W.J. Book), ASME, 1982.

6- Cleghorn, W.L., Fenton, R.G., and Tabarrok, B., "Optimum Design of High-Speed Flexible Mechanisms", *Mechanics and Machine Theory*, Vol. 16, 1981, pp. 399-406.

7- Sunada, W. H., and Dubowsky, S., "On the Dynamic Analysis and Behaviour of Industrial Robotic Manipulators with Elastic Members", *ASME J. Mech. Transmiss. Automat. Design*, Vol. 105, 1983, pp. 42-51.

8- Thompson, B.S., and Sung, C.K., "The Design of Robots and Intelligent Manipulators Using Modern Composite Materials", *Mechanism and Machine Theory*, Vol. 20, No. 6, 1985, pp. 471-482.

9- Spiteri, C.J., Robotics Technology, Saunders College Publishing, Montreal, 1990, p. 1.

10- Poole, H.H., Fundamentals of Robotics Engineering, Van Nostrand Reinhold, New York, 1989, pp. 12-13.

11- Simons, G., Robots: The Quest for Living Machines, Cassell, London, 1992.

12- Koren, Y., Robotics for Engineers, McGraw-Hill, Montreal, 1985.

13- Rivin, E.I., Mechanical Design of Robots, McGraw-Hill, Montreal, 1988.

14- Rosheim, M.E., Robot Evolution: The Development of Anthrobotics, John Wiley & Sons, Toronto, 1994.

15- Ashley, S. "Searching for Land Mines", *Mechanical Engineering*, April 1996, pp. 62-67.

16- Harpel, B.M., Dugan, J.B., Walker, I.D., Cavallaro, J.R., "Analysis of robots for hazardous environments", *Proceedings of the Annual Reliability and Maintainability Symposium*, IEEE, Philadelphia, Pa., 1997, pp. 111-116.

17- Spiessberger, S.M., Humer K., Tschegg, E.K., Weber, H.W., Noma, K., Iwasaki, Y., "Mechanical properties of carbon fiber reinforced plastics and their response to a radiation environment", *Cryogenics*, Vol. 31, 1997, pp. 133-138.

18- Unger, S.W., Unger H.M., Bass, R.T., "AESOP Robotic Arm", *Surgical Endoscopy*, Vol. 8, 1994, p. 1131.

19- Eldridge, B., Gruben, K., LaRose, D., Funda, J., Gomory, S., Karidis, J., McVicker, G., Taylor, R., Anderson, J., "A remote center of motion robotic arm for computer assisted surgery", *Robotica*, Vol. 14, No. 1, 1996, pp. 103-105.

20- Gombert, B., Hirzinger, G., Plank, G., and Schedl, M., "Modular Concepts for a new generation of light weight robots", *Proceedings of the IEEE*, 1994, pp. 1507–1514.

21- Hald, H., "Lightweight CFRP Frame Structures for a ROTEX-derived Manipulator System", *Proceedings of the International Symposium for Advanced Materials for Lightweight Structures*, Organized by European Space Agency, ESTEC, Noordwijk, The Netherlands, March 1992, pp. 21-27.

22- Titan II Telerobotic Manipulator System Brochure, Schilling Development Inc., Davis, California.

23- Mitsubishi Paint Coating Robot Brochure, Mitsubishi Heavy Industries, Ltd., Tokyo, Japan.

24- MTS 200A Robot Brochure, MTS Systems Corporation, Industrial Systems Division, Minneapolis, Minnesota.

25- ASEA Industrial Robot System IRB 6/2 Brochure, Vasteras, Sweden.

26- Advanced Automation Products, BASE Robots Catalog No. 1183/5M, Mack Corporation, Flagstaff, Arizona.

27- Sarcos Dextrous Arm Brochure, Sarcos Research Company, Salt Lake City, Utah.

28- Spine Robotics Brochure, Molndal, Sweden.

29- Barrett Technology Inc. Technical Data Folder, Cambridge, Massachusetts, 1993.

30- Ross-Hime Designs Inc. Technical Data Folder, Minneapolis, Minnesota.

31- Unimate PUMA 200, 500, 700 Series Robots, Unimation Inc., Danbury, CT

32- T^3-566 and T^3-586 Industrial Robots, Cincinnati Milacron, Publication No. A-304-1, Lebanon, Ohio.

33- Robot d'assemblage 4 C.06 SCEMI, CEM, Bourgoin-Jallieu, France.

34- Intelledex Brochure, Corvallis, OR, 1995.

35- Salomonski, N., Shoham, M., Grossman, G., "Light Robot Arm Based on Inflatable Structure", *CIRP Annals*, Vol. 44, No. 1, 1995, pp. 87-90.

36- Xu, Y., Brown, B., Aoki, S., Kanade, T., "Mobility and manipulation of a light-weight space robot", *Robotics and Autonomous Systems*, Vol. 13, 1994, pp. 1-12.

37- Lee, D.G., Kim, K.S., Kwak, Y.K., "Manufacturing of a SCARA-type direct-drive robot with graphite fiber epoxy composite material", *Robotica*, Vol. 9, 1991, pp. 219-229.

38- Lee, D.G., Jeong, K.S., Kim, K.S., Kwak, Y.K., "Development of the anthropomorphic robot with carbon fiber epoxy composite materials", *Composite Structures*, Vol. 25, 1993, pp. 313-324.

39- Kim, Y.G., Jeong, K.S., Lee, D.G. "Development of the composite third robot arm of the six-axis articulated robot manipulator", *Composite Structures*, Vol. 35, 1996, pp. 331-342.

40- Thompson, B.S., Sung, C.K., "The Design of Robots and Intelligent Manipulators Using Modern Composite Materials", *Mechanism and Machine Theory*, Vol. 20, No. 6, 1985, pp. 471-482.

41- Sung, C.K., Thompson, B.S., "A Methodology for Synthesizing High-Performance Robots Fabricated With Optimally Tailored Composite Laminates", *Journal of Mechanisms, Transmissions, and Automation in Design*, Vol. 109, 1987, pp. 74-86.

42- Chao, L-P., "Optimal Design and Sensitivity Analysis of Flexible Robotic Manipulators Fabricated from Advanced Composite Materials", *Journal of Thermoplastic Composite Materials*, Vol. 8, 1995, pp. 346-364.

43- Gordaninejad, F., Chalhoub, N.G., Ghazavi, A., Lin, Q., "Nonlinear Deformation of a Shear-Deformable Laminated Composite-Material Flexible Robot Arm", *Journal of Mechanical Design*, Vol. 114, 1993, pp. 96-102.

44- Ghazavi, A., Gordaninejad, F., Chalhoub, N.G., "Dynamic Analysis of a Composite-Material Flexible Robot Arm", *Computers & Structures*, Vol. 49, No. 2, 1993, pp. 315-327.

45- Chalhoub, N.G., Gordaninejad, F., Lin, Q., Ghazavi, A., "Dynamic Modeling of a Laminated Composite-Material Flexible Robot Arm Made of Short Beams", *The International Journal of Robotics Research*, Vol. 10, No. 5, 1991, pp. 560-569.

46- Gordaninejad, F., Azhdari, A., Chalhoub, N.G., "Nonlinear Dynamic Modeling of a Revolute-Prismatic Flexible Composite-Material Robot Arm", *Journal of Vibration and Acoustics*, Vol. 113, 1991, pp. 461-468.

47- Sung, C.K., Shyl, S.S., "A Composite Laminated Box-Section Beam Design for Obtaining Optimal Elastodynamic Responses of a Flexible Robot Manipulator", *International Journal of Mechanical Science*, Vol. 32, No. 5, 1990, pp. 391-403.

48- Caprino, G., Langella, A., "Optimization of robotic arms made of composite materials for maximum fundamental frequency", *Composite Structures*, Vol. 31, 1995, pp. 1-8.

49- Ghazavi, A., Gordaninejad, F., "A Comparison of the Control of a Flexible Robot Arm Constructed from Graphite/Epoxy Versus Aluminum", *Computers & Structures*, Vol. 54, No. 4, 1195, pp. 621-632.

50- Gordaninejad, F., Vaidyaraman, S., "Active and Passive Control of a Revolute-Prismatic Flexible Composite-Material Robot Arm", *Computers & Structures*, Vol. 53, No. 4, 1994, pp. 867-875.

51- Choi, S.-B., Thompson, B.S., Gandhi, M.V., "Modeling and control of a single-link flexible manipulator featuring a graphite-epoxy composite arm", *Proceedings of the 1990 IEEE International Conference on Robotics and Automation*, Vol. 2, pp. 1450-1455.

52- Wang, L., Chen, C., "On the Numerical Kinematic Analysis of General Parallel Robotic Manipulators", *IEEE Transactions on Robotics and Automation*, Vol. 9, No. 3, June 1993, pp. 272-285.

53- Hayward, V., "Design of a Hydraulic Robot Shoulder Based on a Combinatorial Mechanism", *Proceedings of the 3rd International Symposium on Experimental Robotics*, ISER-3, Kyoto, Japan, 1993.

54- Hayward, V., "Borrowing some design ideas from biological manipulators to design an artificial one", *Robots and Biological Systems*, NATO Series, P. Dario, P Aebisher and G. Sandini (editors), Springer Verlag, 1993, pp. 139-151.

55- Kurtz, R., and Hayward, V., "Multi-goal optimization of a parallel mechanism with actuator redundancy", *IEEE Transactions on Robotics and Automation*, Vol. 8, No. 5, 1992, pp. 644-651.
56- Boulet, B., Daneshmend, L.K., Hayward, V., and Nemri, C., "System Identification and Modeling of a High-Performance Hydraulic Actuator", *Experimental Robotics 2, Lecture Notes in Control and Information Sciences*, Springer Verlag, 1992.
57- Hollerbach, J.M., Hunter, I.W., and Ballantyne, J., "A comparative analysis of actuator technologies for robotics", Robotics Review 2, MIT Press, 1991.
58- Boulot, B., Daneshmend, L., Hayward, V., Nemri, C., "Characterization, Modeling, and Identification of a High-Performance Hydraulic Actuator for Robotics", Technical Report TR-CIM-93-9, McGill Center for Intelligent Machines, March 1993.
59- Advanced Robotic Controller System Manual, Animate Systems Incorporated (ASI), Salt Lake City, Utah, 1991.
60- Boulet, B., "Modeling and Control of a Robotic Joint with In-Parallel Redundant Actuators", Master's Thesis, Dept. of Electrical Engineering, McGill University, McGill University, Montreal, 1992.
61- Boulet, B., Hayward, V., "Robust Control of a Robot Joint with Hydraulic Actuator Redundancy. Part I: Theory, Applications and Controller Design", Technical Report TR-CIM-93-6, McGill Center for Intelligent Machines, Montreal, 1993.
62- Boulet, B., Hayward, V., "Robust Control of a Robot Joint with Hydraulic Actuator Redundancy. Part II: Practical Variations and Experimentation", Technical Report TR-CIM-93-7, McGill Center for Intelligent Machines, Montreal, 1993.
63- The Advanced Composites Group, Technical Data Sheet, Tulsa, Oklahoma.
64- Cowper, G.R., "The Shear Coefficient in Timoshenko's Beam Theory", ASME *Journal of Applied Mechanics*, Vol. 33, June 1966, pp. 335-340.
65- Madabhusi-Raman, P., Davalos, J., "Static shear correction factor for laminated rectangular beams", *Composites Part B: Engineering*, vol. 27, no. 3-4, 1996, pp. 285-293.
66- Tsai, S., Composites Design, 4th Edition, Think Composites, Dayton, Ohio, 1988, pp. 8-10.
67- Bank, L.C., and Bednarczyk, P.J., "A Beam Theory for Thin-Walled Composite Beams", *Composites Science and Technology*, Vol. 32, 1988, pp. 265-277.
68- Bank, L.C., "Shear Coefficients for Thin-Walled Composite Beams", *Composite Structures*, Vol. 8, 1987, pp. 47-61.
69- Belluzzi, O., *Scienza delle Costruzioni*, I, p. 94, Zanichelli, 1986.
70- Lessard, L., Mechanics of Composite Materials, Course Notes, McGill University, 1995.
71- Eckold, G., Design and Manufacture of Composite Structures, McGraw Hill, 1994.
72- Wang, H.-S., Hung, C.-L., Chang, F.-K., "Bearing Failure of Bolted Composite Joints. Part I: Experimental Characterization", *Journal of Composite Materials*, Vol. 30, No. 12, 1996, pp. 1284-1313.
73- Wang, H.-S., Hung, C.-L., Chang, F.-K., "Bearing Failure of Bolted Composite Joints. Part II: Model and Verification", *Journal of Composite Materials*, Vol. 30, No. 12, 1996, pp. 1359-1399.

74- Schulz, K.C., Hietala, H.J., Packman, P.F., "A Statistical Approach to the Analysis of Ultimate Strengths of Bolted Joints in Laminated Composites", *Composites Science and Technology*, Vol. 56, 1996, pp. 505-517.
75- Persson, E., Eriksson, I., Hammersberg, P., "Propagation of Hole Machining Defects in Pin-Loaded Composites Laminates", *Journal of Composite Materials*, Vol. 31, No. 4, 1997, pp. 383-408.
76- Sadat, A.B., Chan, W.S., Wang, B.B., "Delamination of Carbon/Epoxy Laminate during Drilling Operation", *Composite Material Technology, ASME PD*, D. Hui and T.H. Kozik eds., Vol. 32, 1990, pp. 85-88.
77- Abrate, S., Walton, D.A., "Machining of Composite Materials, Part I", *Composites Manufacturing*, Vol. 3, No. 2, 1992, pp. 75-83.
78- Jeong, K.S., Lee, D.G., Kwak, Y.K., "Experimental investigation of the dynamic characteristics of carbon fibre epoxy composite thin beams", *Composite Structures*, Vol. 33, No. 2, 1995, pp. 77-86.
79- Frekote Products Technical Data Sheet, Dexter Corporation Distributor Programs, Seabrook, New Hampshire.
80- Tan, S.C., Tsai, S., "Off-Axis Plies Made by Folding", *Journal of Reinforced Plastics and Composites*, Vol. 3, October 1984, pp. 294-299.
81- TSB 124 Bonded Honeycomb Sandwich Construction, Hexcel Corporation Technical Report, 1993.
82- Strong, A.B., Fundamentals of Composites Manufacturing: Materials, Methods and Applications, Society of Manufacturing Engineers, Deerborn, Michigan, 1989, pp. 117-120.
83- MTS Reference Manual, Vol. 1-3, MTS Systems Corporation, Minneapolis, Minnesota.
84- Cole, R.T., Bateh, E.J., and Potter, J., "Fasteners for Composite Structures", *Composites*, Vol. 13, No. 3, July 1982, p. 233.
85- Parker, R.T., "Mechanical Fastener Selection", Engineering Materials Handbook, Vol. 1 (Composites), ASM International, Metals Park, Ohio, 1987, p. 706.
86- Cherry Commercial Fastening Systems, Cherry Division of Textron, Inc., Santa Ana, CA.
87- Tucker, W.C., Brown, R., and Russell, L., "Corrosion Between a Graphite/Polymer Composite and Metals", *Journal of Composite Materials*, Vol. 24, 1990, pp. 90-92.
88- Fontana, N.G., Corrosion Engineering, McGraw Hill, 1986.
89- Riggs, E.L. and Krupp, W., "Corrosion Principle and Protection", Paper presented at Technical Symposia for China, Peking, Oct. 1978.
90- Stone, R.H., "Dissimilar Material Separation", Engineering Materials Handbook, Vol. 1 (Composites), ASM International, Metals Park, Ohio, 1987, pp. 716-718.
91- Bouraad, J., "Joining of Laminated Composite Materials with Titanium", Master's Thesis, McGill University, January 1997.
92- Adams, R.D., Harris, J.A., "Bonding of composites to metals", *Adhesion*, Vol. 12, 1988, pp. 193-204.
93- Lees, W.A., "Stress in bonded joints", *Adhesion*, Vol. 12, 1988, pp. 141-158.

94- Price, A., Moulds, R.J., "Bonded propshafts: design and assembly of composite tubes and metal end fittings", *Materials Science and Technology*, Vol. 9, June 1993, pp. 528-535.
95- Hysol Adhesives Selection Guide, Hysol Engineering Adhesives, Dexter Corporation Distributor Programs, Seabrook, NH.
96- Loctite Technology, Loctite Canada, Mississauga, Ontario.
97- CIBA Formulated Systems Group Araldite and Arathane Adhesives Selector Guide, CIBA-GEIGY Corporation, East Lansing, MI.
98- Shigley, J.E., and Mischke, C.R., Mechanical Engineering Design, McGraw-Hill, 1989, p. 742.
99- Beer, F.P., and Johnson, E.R., Mechanics of Materials, 2nd Edition, McGraw-Hill, 1992, p. 285.
100- Meriam, J.L., and Kraige, L.G., Engineering Mechanics Volume 2: Dynamics, 2nd Edition, John Wiley and Sons, 1987, p. 630.
101- SKF Needle Roller Bearings Catalog, Scanprint, Denmark, 1991.
102- SKF Precision Bearings Catalog, Scanprint, Denmark, 1987.
103- SKF 925 Bearing Catalog, Canada, 1993.
104- The Torrington Company Service Catalog, Ingersoll-Rand, p.338.
105- Adams, G., de Silva, E., Metaxas, N., Mocanu, R., Schincariol, A., "Robotic Elbow Joint", Design Report, Dept. of Mechanical Engineering, McGill University, 1995.
106- Boresi, A.P., Schmidt, R.J., Sidebottom, O.M., Advanced Mechanics of Materials, Fifth Edition, John Wiley & Sons, Toronto, 1993, p. 240.
107- Hayward, V., Kurtz, R., "Modeling of a Parallel Wrist Mechanism with Actuator Redundancy", McGill Research Center for Intelligent Machines, Technical Report CIM-89-4, January 1989.
108- Habib, C, Kee, R., "Modeling of a Redundant Acutator Parallel Mechanism Wrist Joint", Mechanical Laboratory II Report, McGill University, 1994.
109- Chevalier, P., Elsafiti, S., Sharifian, J., Sveinbjornsson, B., "Design of Robotic Wrist", Design Report, McGill University, 1997.
110- Robotic Grippers and Automation Components, Techno Sommer Automatic Catalog, New Hyde Park, N.Y., 1995.
111- Sensoflex/Astek End of Arm Products, Product Digest, Barry Wright Corporation, Watertown, Massachusetts.
112- Salerno, R.J., Canfield, S.L., Ganino, A.J., Reinholtz, C.F., "Parallel, four degree-of-freedom robotic wrist", 21st Annual Design Automation Conference, American Society of Mechanical Engineers, Design Engineering Division, vol. 82, no. 1, 1995, pp. 765-771.
113- Beaumont, R.G., Crowder, R.M., "Two-Armed Robot Systems: A Review of Current Theory and the Development of Algorithms for Real-Time Collision Avoidance", *IEEE Colloquium on Controllers for Robotic Applications-Concepts and Implementations*, Digest No. 1989/127, November 1989.
114- Koivo, A.J., Bekey, G.A., "Report on Workshop on Coordinated Multiple Robot Manipulators: Planning, Control, and Applications", *IEEE Journal of Robots and Automation*, Vol. 4, No. 1, 1988, pp. 91-93.

115- Lee, B.H., Lee, C.S.G., "Collision-Free Motion Planning of Two Robots", *IEEE Transactions on Systems, Man and Cybernetics*, 1987, pp. 21-32.

116- Basta, R.A., Mehrotra, R., Varanasi, M.R., "Detecting and Avoiding Collisions Between Two Robot Arms in a Common Workplace", *Robot Control Theory and Applications*, 1988, pp. 185-192.

117- Roach, J.W., Boaz, M.N., "Coordinating the Motions of Robot Arms in a Common Workplace", *IEEE Journal of Robotics and Automation*, October 1987, pp. 437-444.

118- Tarn, T.J., Bajczy, A.K., Yun, X., "Design of Dynamic Control of Two Cooperating Robot Arms: Closed Chain Formulation", *Proceedings of IEEE International Conference on Robotics and Automation*, 1987, pp. 7-13.

119- Chapnik, B.V., Heppler, G.R., Aplevich, J.D., "Controlling the Impact Response of a One-Link Flexible Robotic Arm", *IEEE Transactions on Robotics and Automation*, Vol. 9, No. 3, June 1993, pp. 346-351.

120- Lagace, P.A., "Understanding Impact on Composite Structures", Copy of Presentation, Technology Laboratory for Advanced Composites, Department of Aeronautics and Astronautics, MIT, Cambridge, Mass.

121- Bicos, A.S., and Springer, G.S., "Design of a Composite Boxbeam", *Journal of Composite Materials*, Vol. 20, January 1986, pp. 86-109.

Appendix A

Detail Drawings

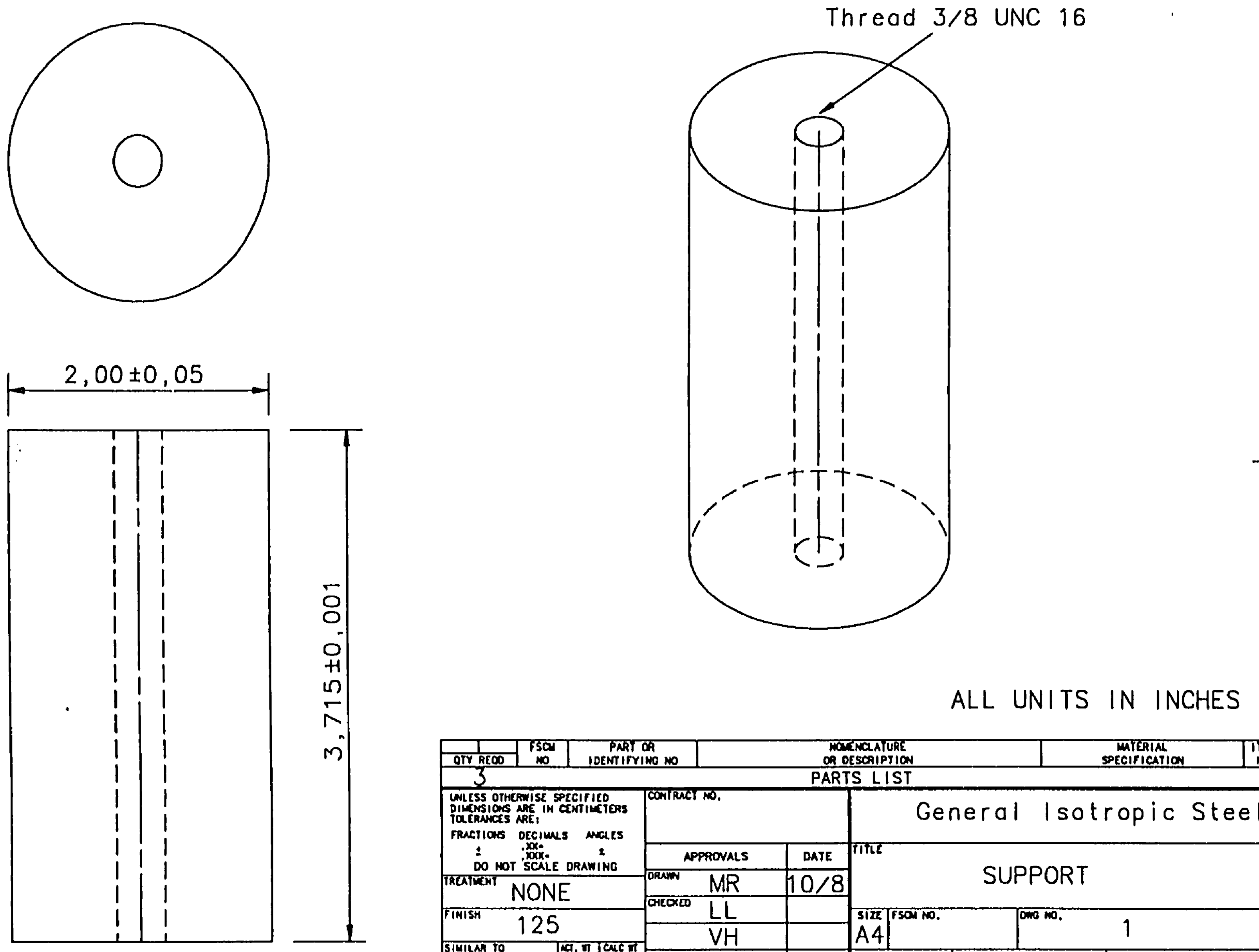

QTY REQD	FSCM NO	PART OR IDENTIFYING NO	NOMENCLATURE OR DESCRIPTION	MATERIAL SPECIFICATION	ITEM NO
3					

PARTS LIST

UNLESS OTHERWISE SPECIFIED DIMENSIONS ARE IN CENTIMETERS TOLERANCES ARE:
FRACTIONS ± DECIMALS .XX= .XXX= ANGLES ±
DO NOT SCALE DRAWING

TREATMENT NONE
FINISH 125
SIMILAR TO | ACT. WT | CALC WT

CONTRACT NO.

APPROVALS		DATE
DRAWN	MR	10/8
CHECKED	LL	
	VH	

General Isotropic Steel

TITLE SUPPORT

SIZE A4 | FSCM NO. | DWG NO. 1

SCALE N/A | SHEET 1 OF 1

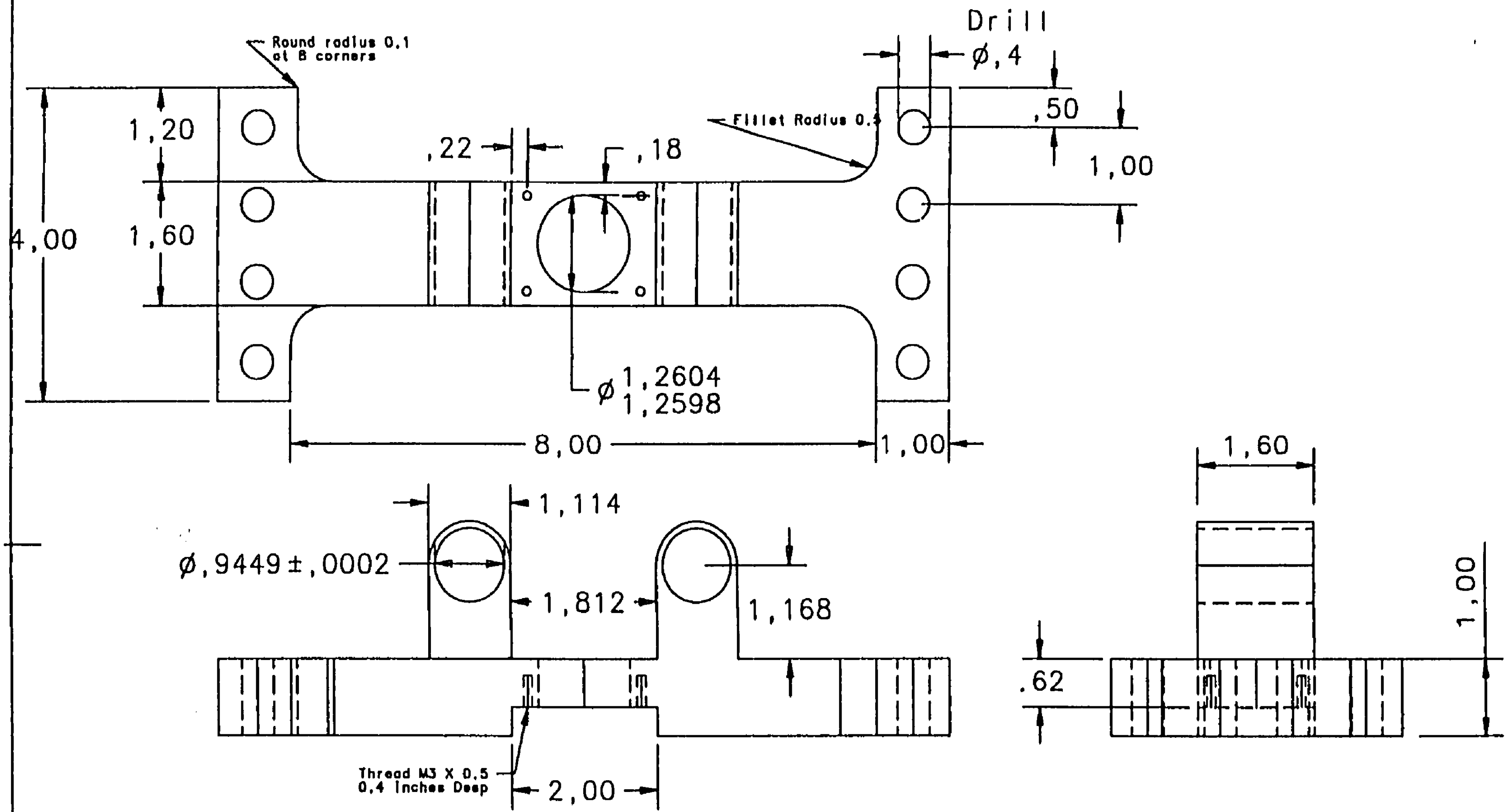

All Units in inches

QTY REQD	FSCM NO	PART OR IDENTIFYING NO	NOMENCLATURE OR DESCRIPTION	MATERIAL SPECIFICATION	ITEM NO
1			PARTS LIST	ASTM A581	

UNLESS OTHERWISE SPECIFIED DIMENSIONS ARE IN CENTIMETERS TOLERANCES ARE: ,X = ,1 FRACTIONS ± DECIMALS ,XX= ,01 ,XXX= ,001 ANGLES ± DO NOT SCALE DRAWING	CONTRACT NO.		Stainless Steel 303
TREATMENT Annealed	APPROVALS	DATE	TITLE H-BASE
	DRAWN MR	10/10	
FINISH 125	CHECKED LL		SIZE A4 · FSCM NO. · DWG NO. 2
SIMILAR TO · ACT. WT · CALC WT	VH		SCALE N/A · SHEET 1 OF 1

REVISIONS				
ZONE	REV	DESCRIPTION	DATE	APPROVED

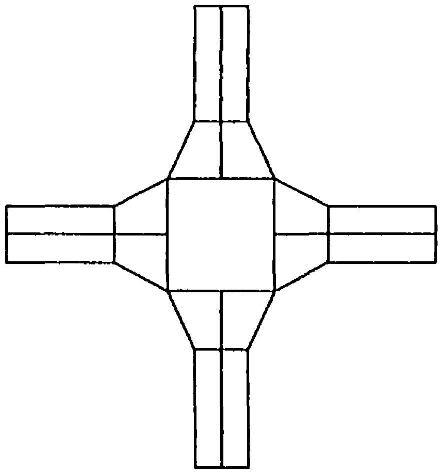

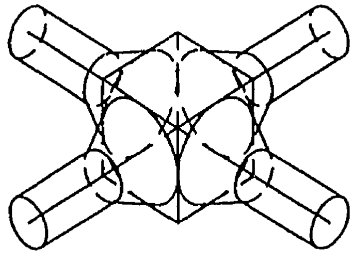

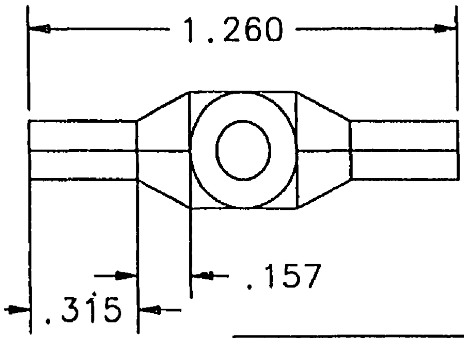

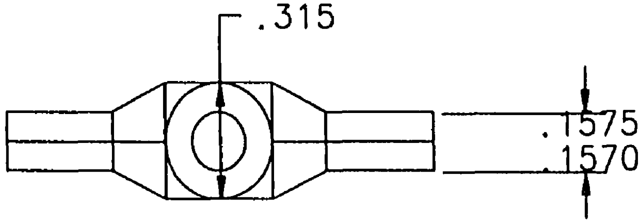

ALL UNITS IN INCHES

QTY REQD	FSCM NO	PART OR IDENTIFYING NO	NOMENCLATURE OR DESCRIPTION	MATERIAL SPECIFICATION	ITEM NO
1			PARTS LIST	ASTM A276	

UNLESS OTHERWISE SPECIFIED DIMENSIONS ARE IN INCHES TOLERANCES ARE: FRACTIONS ± DECIMALS .XX= ±.02 .XXX= ±.002 ANGLES ± DO NOT SCALE DRAWING	CONTRACT NO.		Stainless Steel Type 403
	APPROVALS	DATE	TITLE TAPERED CENTER CUBE
TREATMENT Intermediate Temper Hot Finished	DRAWN MR	10/9	
	CHECKED LL		
FINISH 125	ISSUED		SIZE A | FSCM NO. | DWG NO. 3
SIMILAR TO | ACT. WT | CALC WT			SCALE N/A | SHEET 1 OF 1

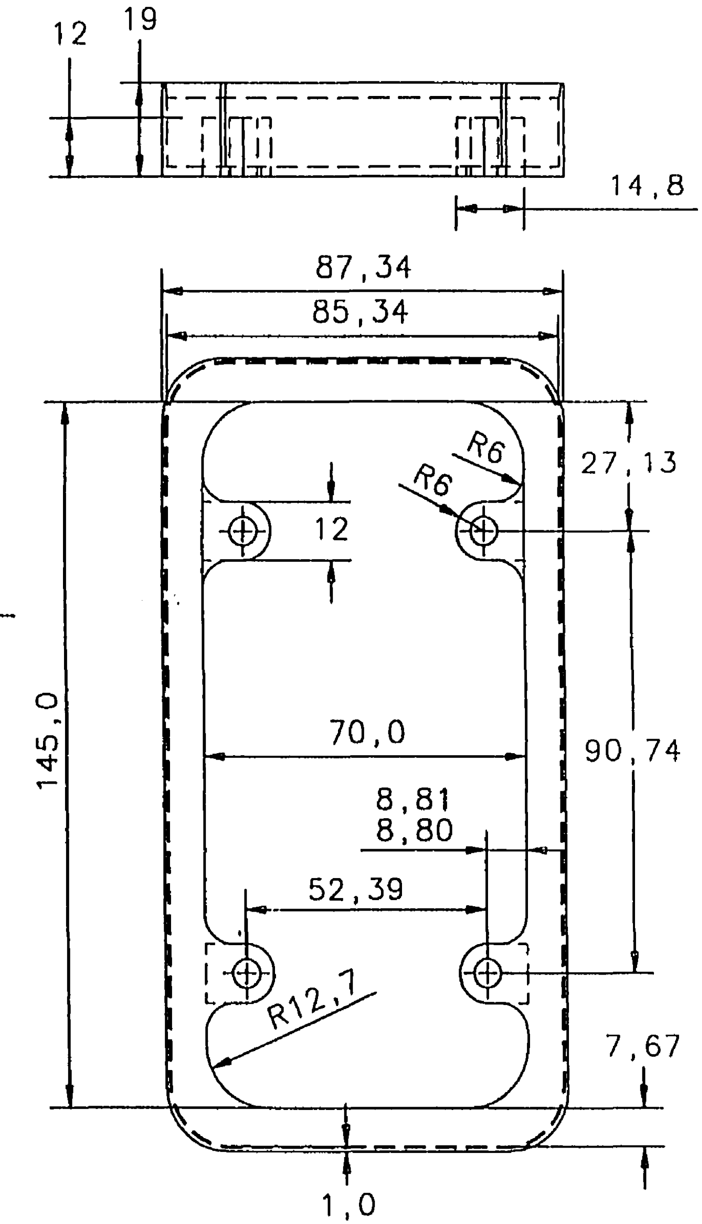

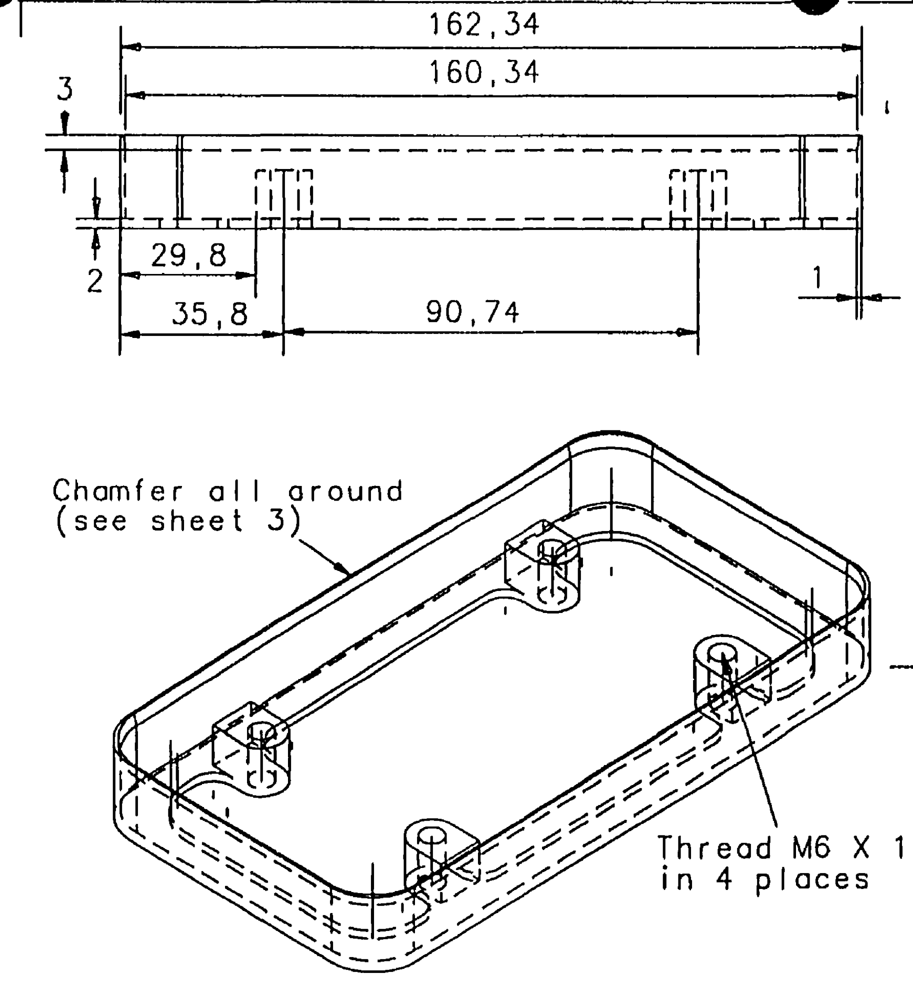

QTY REQD	FSCM NO	PART OR IDENTIFYING NO	NOMENCLATURE OR DESCRIPTION	MATERIAL SPECIFICATION	ITEM NO
1			PARTS LIST	ASTM A581	

UNLESS OTHERWISE SPECIFIED DIMENSIONS ARE IN CENTIMETERS TOLERANCES ARE: ,X = ±0,1 FRACTIONS ± DECIMALS ,XX= ±.01 ,XXX= ±.005 ANGLES ± DO NOT SCALE DRAWING	CONTRACT NO. 241-04-13-0	Stainless Steel 303
TREATMENT Annealed	APPROVALS / DATE DRAWN M. Roy 3/24 CHECKED L. Lessard	TITLE BRACKET
FINISH 125		SIZE A4 · FSCM NO. · DWG NO. 4
SIMILAR TO · ACT. WT · CALC WT		SCALE N/A · UNITS: MM · SHEET 1 OF 3

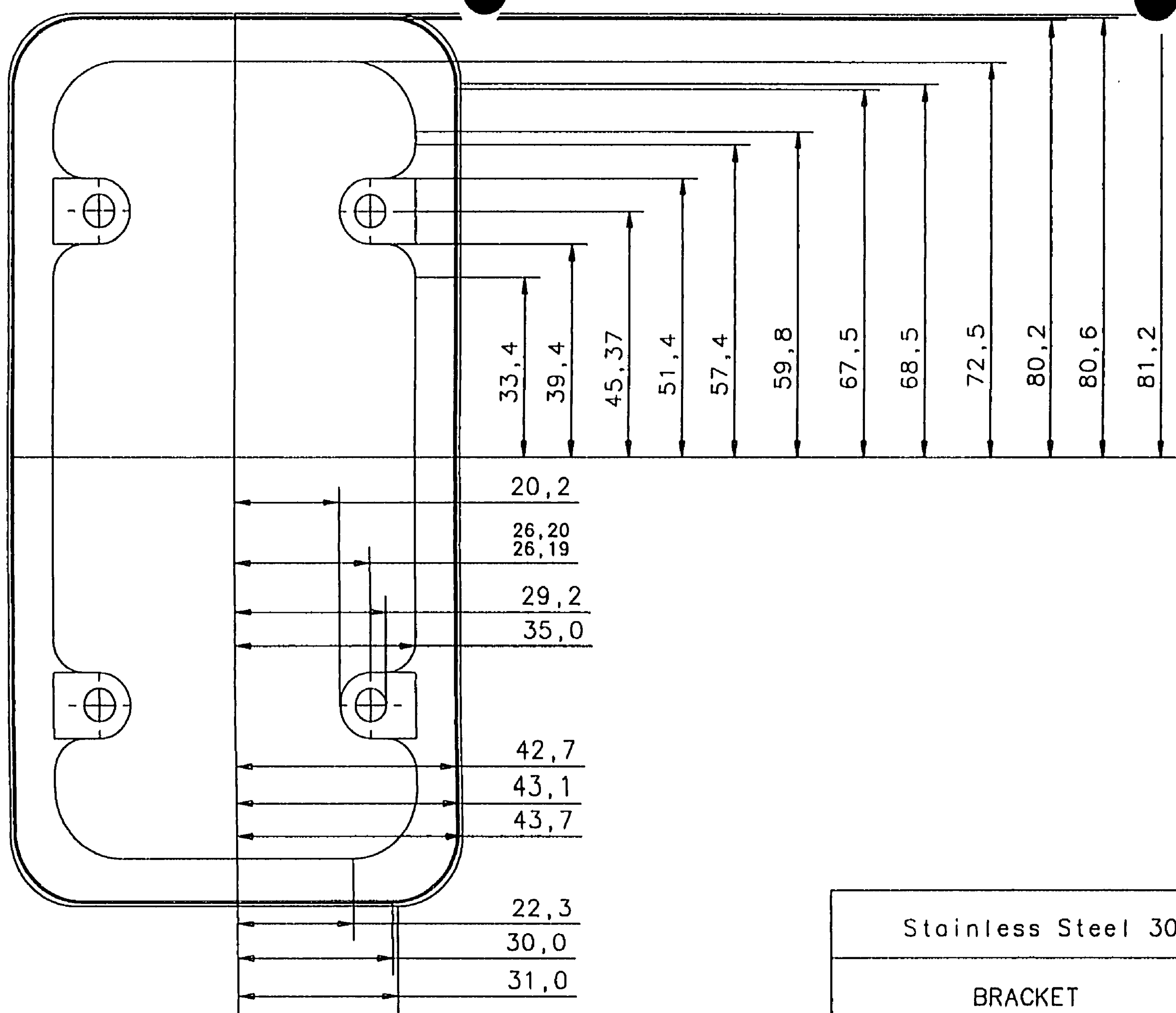

Stainless Steel 303	
BRACKET	
DWG. NO. 4	SHEET 2 OF 3

DETAIL OF CHAMFER

Outside

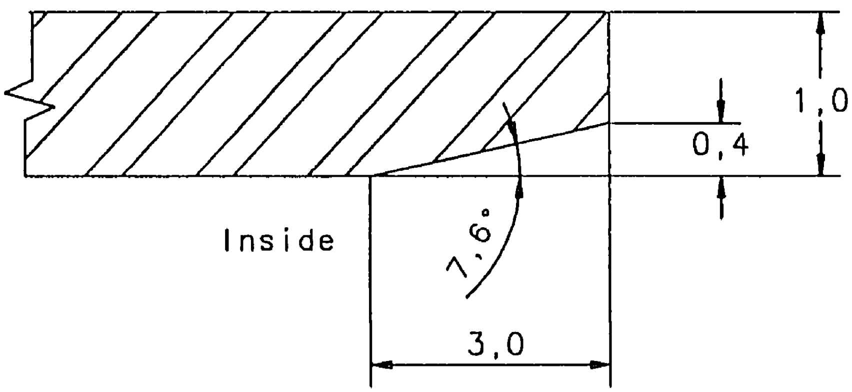

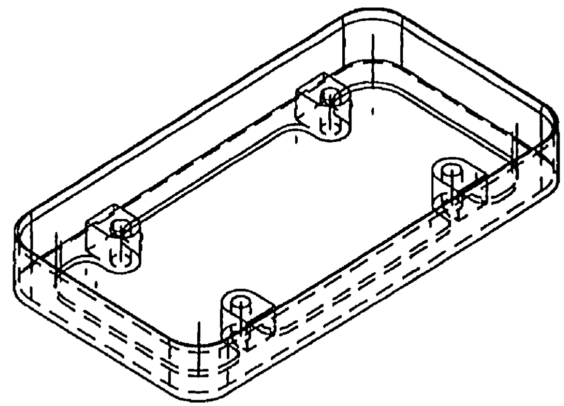

QTY REQD	FSCM NO	PART OR IDENTIFYING NO	NOMENCLATURE OR DESCRIPTION	MATERIAL SPECIFICATION	ITEM NO

PARTS LIST

UNLESS OTHERWISE SPECIFIED DIMENSIONS ARE IN CENTIMETERS
TOLERANCES ARE: .X = ±0.1
FRACTIONS ± DECIMALS .XX= .XXX= ANGLES ±
DO NOT SCALE DRAWING

TREATMENT

FINISH

SIMILAR TO | ACT. WT | CALC WT

CONTRACT NO. 241-04-13-0

APPROVALS		DATE
DRAWN	M. Roy	
CHECKED	L. Lessard	

Stainless Steel 303

TITLE BRACKET

SIZE A4 | FSCM NO. | DWG NO. 4

SCALE N/A | UNITS: MM | SHEET 3 OF 3

REVISIONS				
ZONE	REV	DESCRIPTION	DATE	APPROVED

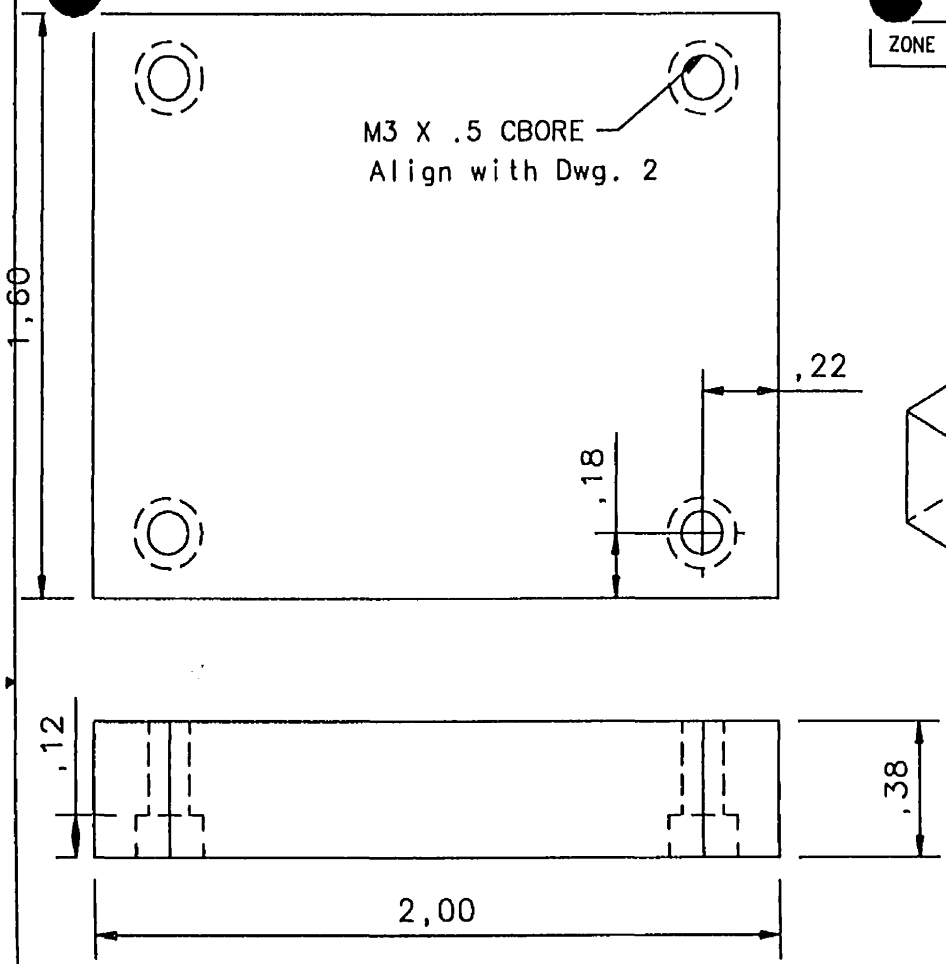

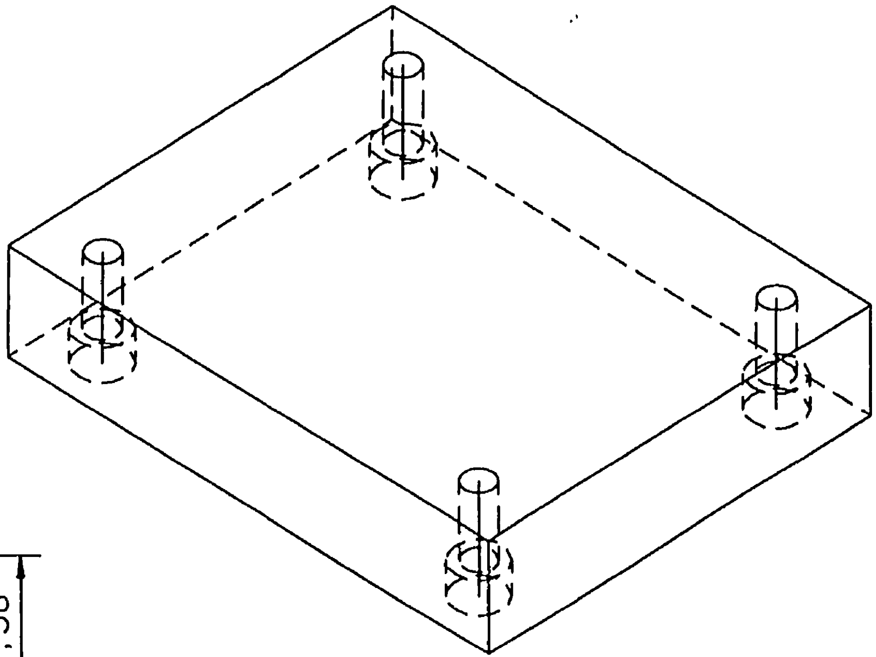

All Units in Inches

QTY REQD	FSCM NO	PART OR IDENTIFYING NO	NOMENCLATURE OR DESCRIPTION	MATERIAL SPECIFICATION	ITEM NO
1			PARTS LIST	ASTM A581	

UNLESS OTHERWISE SPECIFIED DIMENSIONS ARE IN INCHES TOLERANCES ARE:
FRACTIONS ± DECIMALS .XX= .01 .XXX= ANGLES ±
DO NOT SCALE DRAWING

TREATMENT Annealed

FINISH 125

SIMILAR TO | ACT. WT | CALC WT

CONTRACT NO.

APPROVALS		DATE
DRAWN	MR	10/22
CHECKED	LL	
ISSUED		

Stainless Steel 303

TITLE
PLATE

SIZE A | FSCM NO. | DWG NO. 6

SCALE N/A | SHEET 1 OF 1

REVISIONS				
ZONE	REV	DESCRIPTION	DATE	APPROVED

N.B. Align Threaded Holes with Dwg. 8 and 9

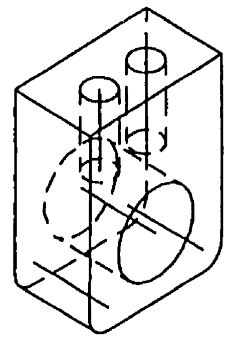

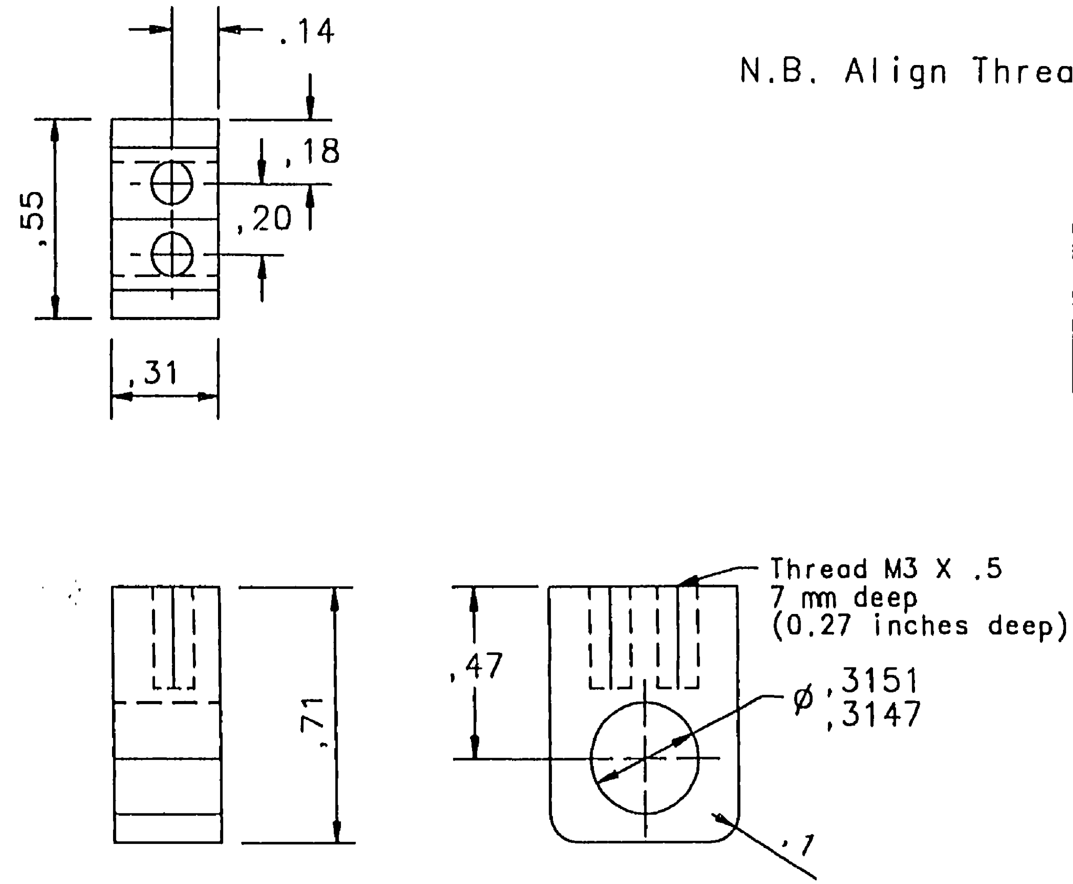

All Units in Inches

QTY REQD	FSCM NO	PART OR IDENTIFYING NO	NOMENCLATURE OR DESCRIPTION	MATERIAL SPECIFICATION	ITEM NO
2			PARTS LIST	ASTM A581	

UNLESS OTHERWISE SPECIFIED DIMENSIONS ARE IN INCHES TOLERANCES ARE: FRACTIONS ± DECIMALS .XX- .01 .XXX- .005 ANGLES ± DO NOT SCALE DRAWING	CONTRACT NO.	Stainless Steel 303
TREATMENT Annealed	APPROVALS / DATE; DRAWN MR 10/25	TITLE Side Extension Piece
FINISH 125	CHECKED LL	SIZE A; FSCM NO.; DWG NO. 7
SIMILAR TO; ACT. WT; CALC WT	ISSUED	SCALE N/A; SHEET 1 OF 1

N.B. Align Holes with Dwg. 7

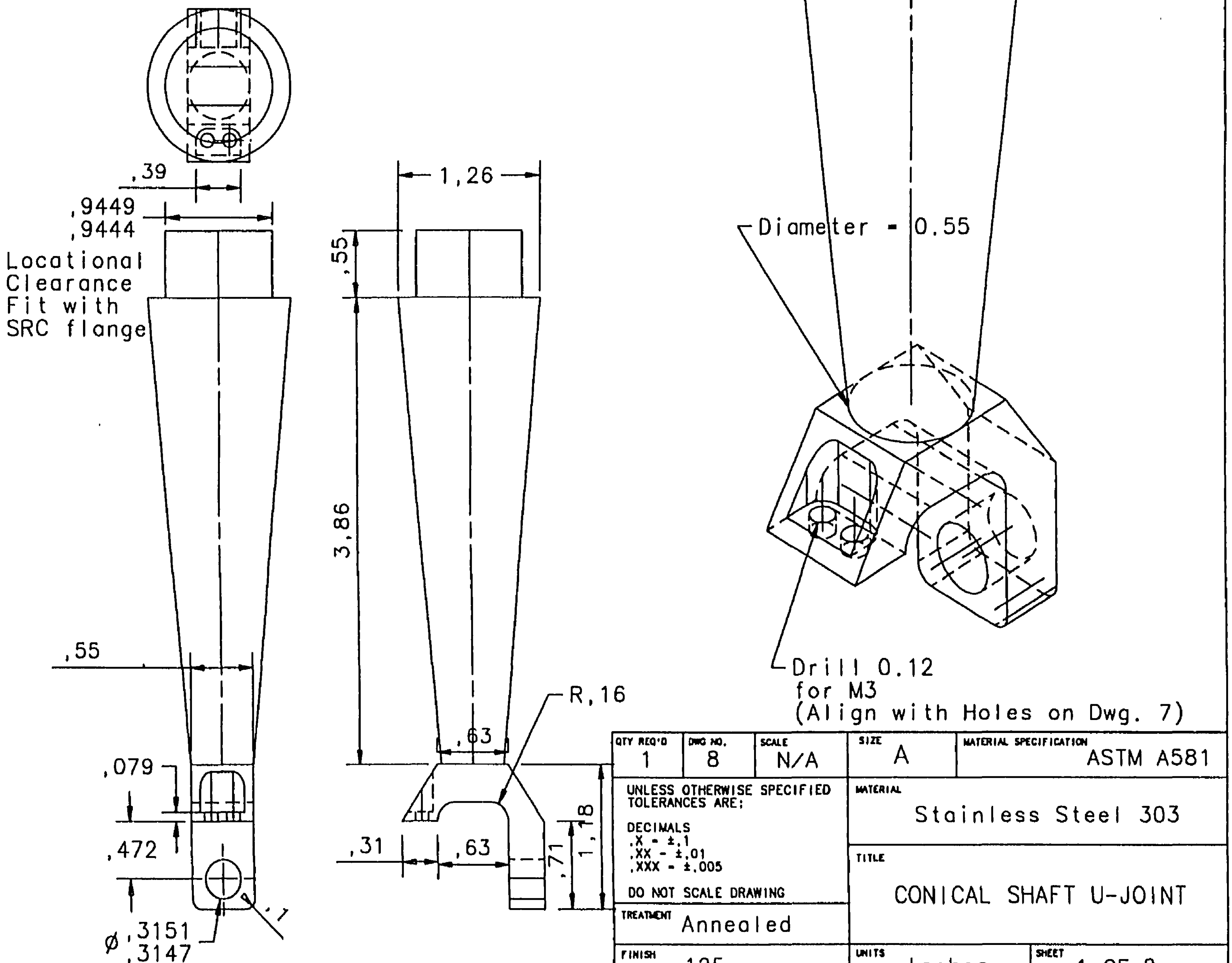

QTY REQ'D	DWG NO.	SCALE	SIZE	MATERIAL SPECIFICATION
1	8	N/A	A	ASTM A581

UNLESS OTHERWISE SPECIFIED TOLERANCES ARE: DECIMALS .X = ±.1 .XX = ±.01 .XXX = ±.005 DO NOT SCALE DRAWING	MATERIAL Stainless Steel 303
TREATMENT Annealed	TITLE CONICAL SHAFT U-JOINT
FINISH 125	UNITS Inches / SHEET 1 OF 2

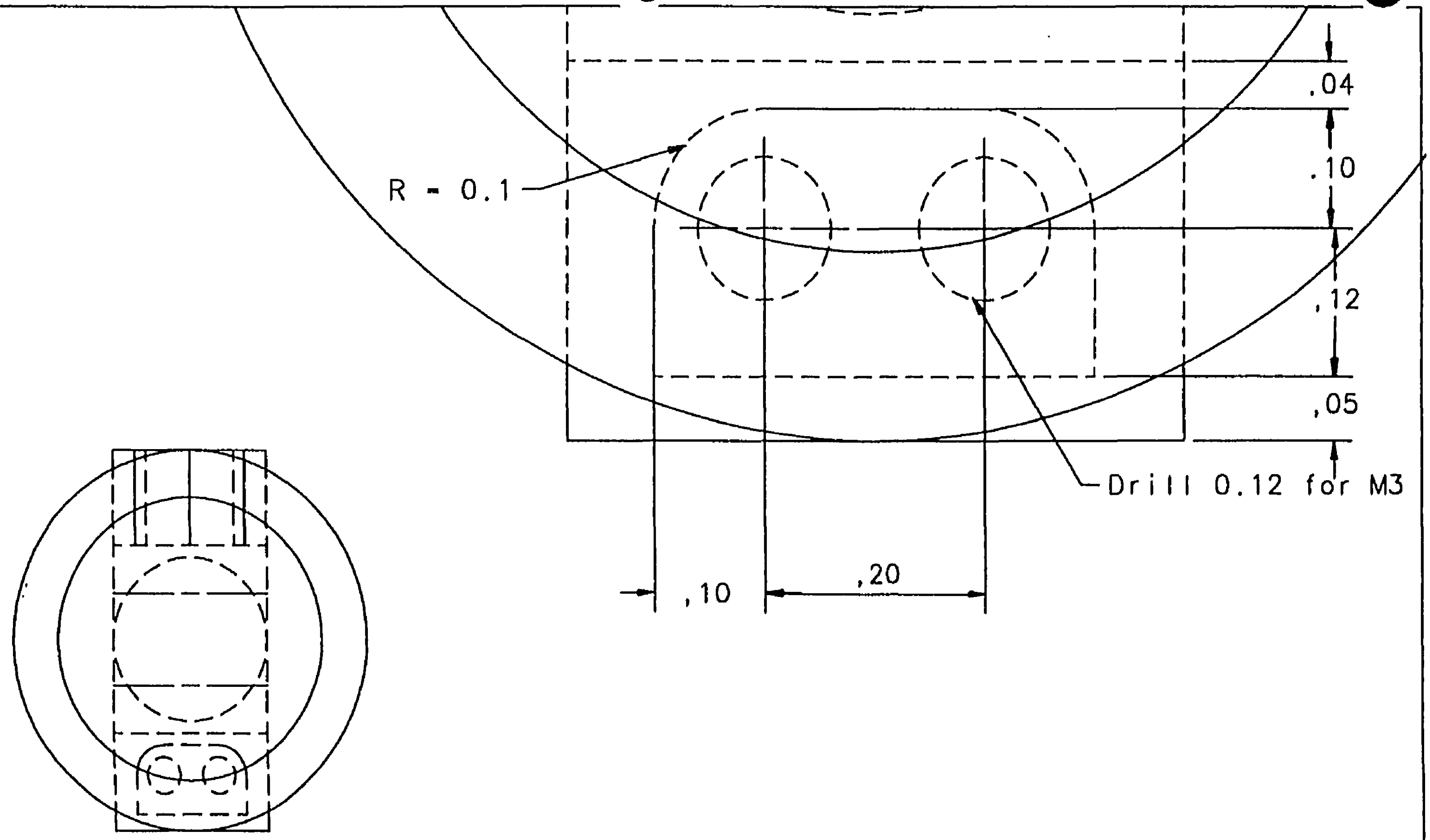

QTY REQ'D	DWG NO.	SCALE	SIZE	MATERIAL SPECIFICATION
1	8	N/A	A	ASTM A581

UNLESS OTHERWISE SPECIFIED TOLERANCES ARE: DECIMALS .X = ±.1 .XX = ±.01 .XXX = ±.005 DO NOT SCALE DRAWING	MATERIAL Stainless Steel 303
TREATMENT Annealed	TITLE CONICAL SHAFT U-JOINT
FINISH 125	UNITS Inches
	SHEET 2 OF 2

N.B. Align Holes with Dwg. 7

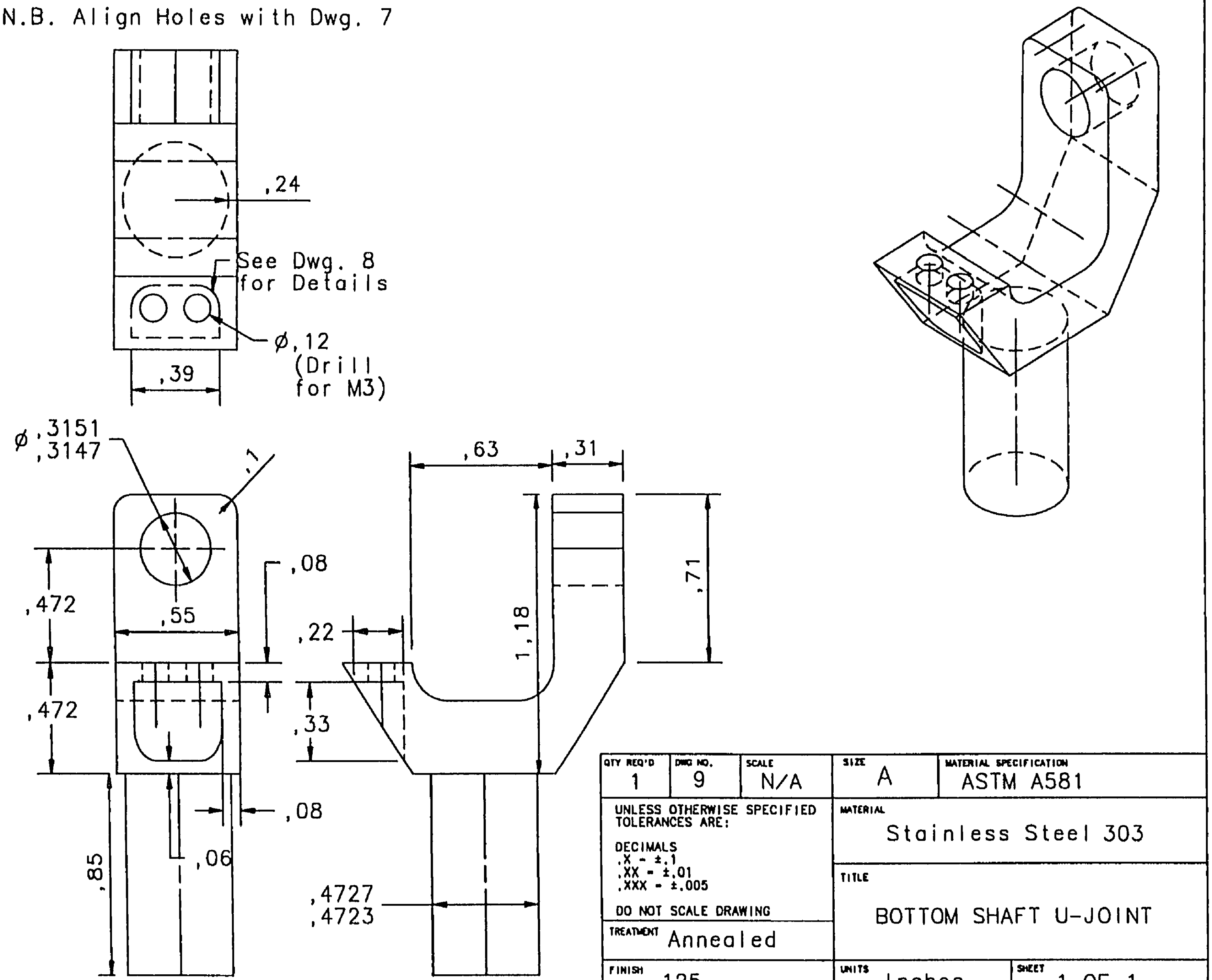

QTY REQ'D	DWG NO.	SCALE	SIZE	MATERIAL SPECIFICATION
1	9	N/A	A	ASTM A581

UNLESS OTHERWISE SPECIFIED TOLERANCES ARE: DECIMALS .X = ±.1 .XX = ±.01 .XXX = ±.005 DO NOT SCALE DRAWING	MATERIAL: Stainless Steel 303
TREATMENT: Annealed	TITLE: BOTTOM SHAFT U-JOINT
FINISH: 125	UNITS: Inches — SHEET: 1 OF 1

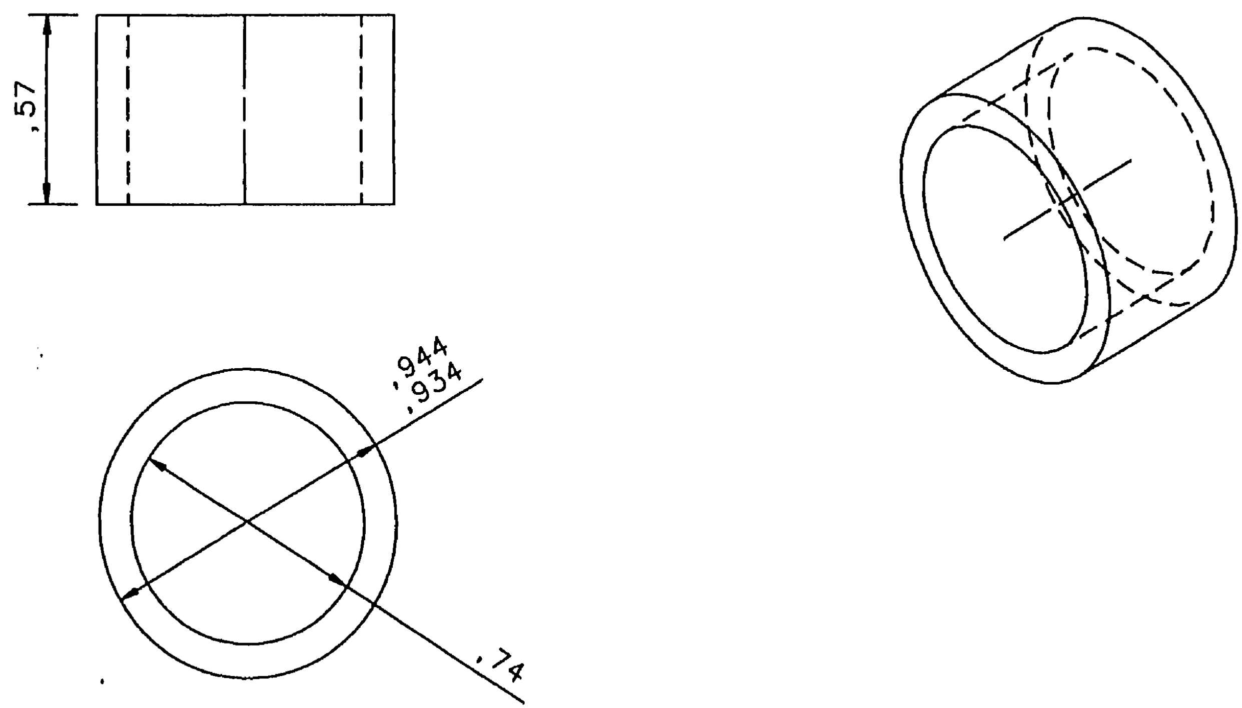

QTY REQ'D	DWG NO.	SCALE	SIZE	MATERIAL SPECIFICATION
2	10	N/A	A	

UNLESS OTHERWISE SPECIFIED
TOLERANCES ARE;

DECIMALS
.X = ±.1
.XX = ±.01
.XXX = ±.005

DO NOT SCALE DRAWING

MATERIAL	Nylon 6/6
TITLE	SPACER
TREATMENT	None
FINISH	125
UNITS	Inches
SHEET	1 OF 1

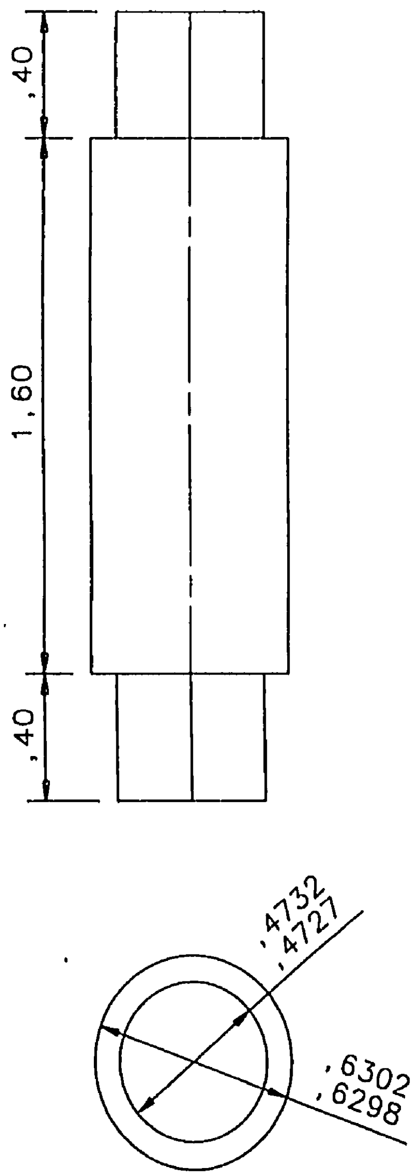

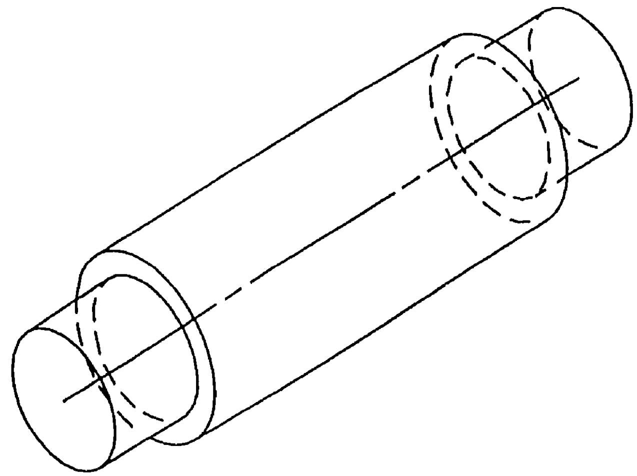

QTY REQ'D	DWG NO.	SCALE	SIZE	MATERIAL SPECIFICATION
2	11	N/A	A	ASTM A581

UNLESS OTHERWISE SPECIFIED TOLERANCES ARE: DECIMALS .X = ±.1 .XX = ±.01 .XXX = ±.005 DO NOT SCALE DRAWING	MATERIAL Stainless Steel 303
TREATMENT Annealed	TITLE BEARING SHAFT
FINISH 125	UNITS Inches — SHEET 1 OF 1

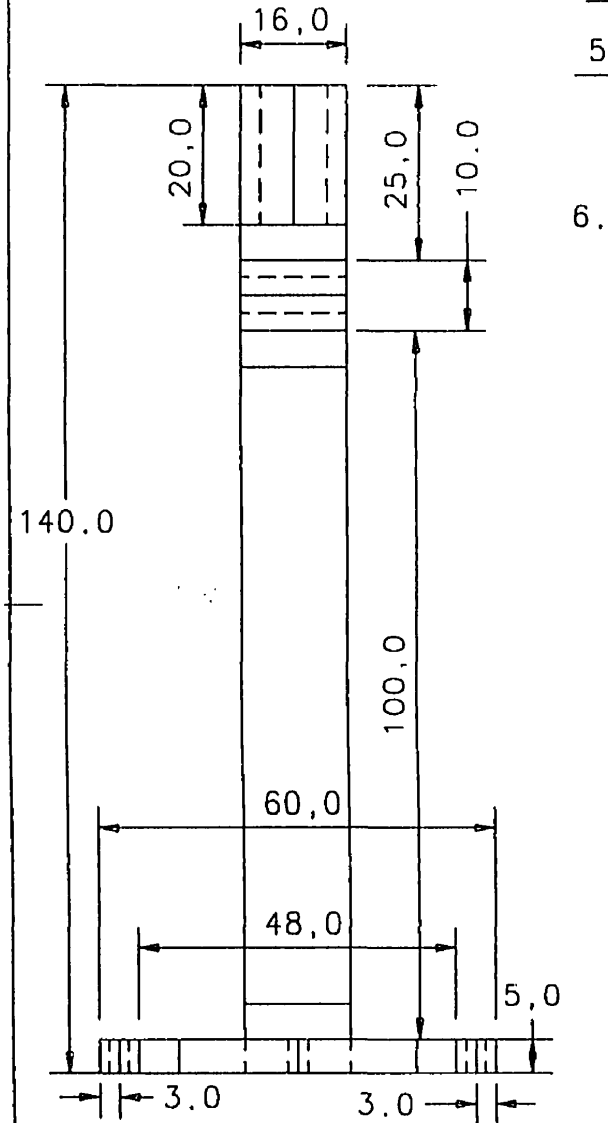

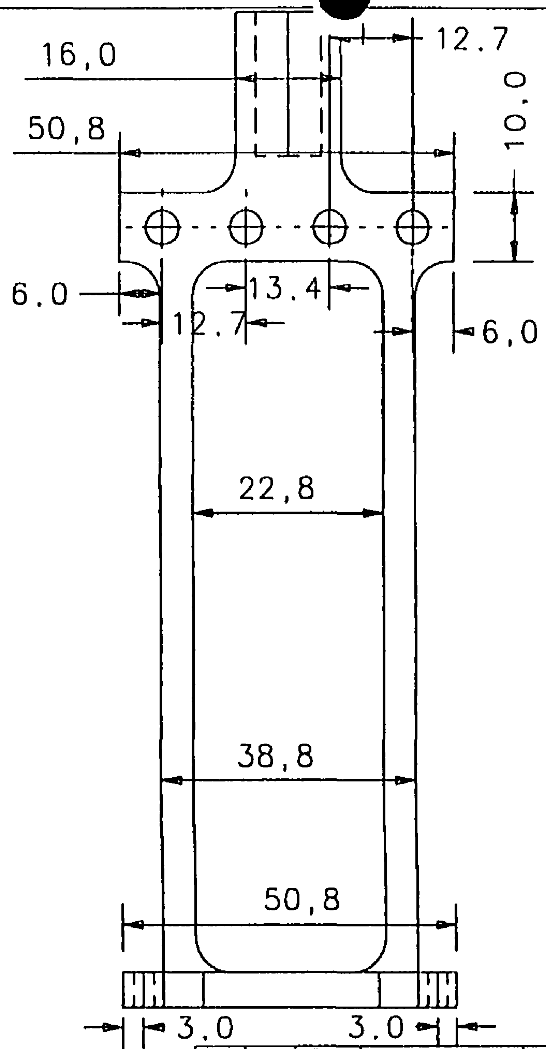

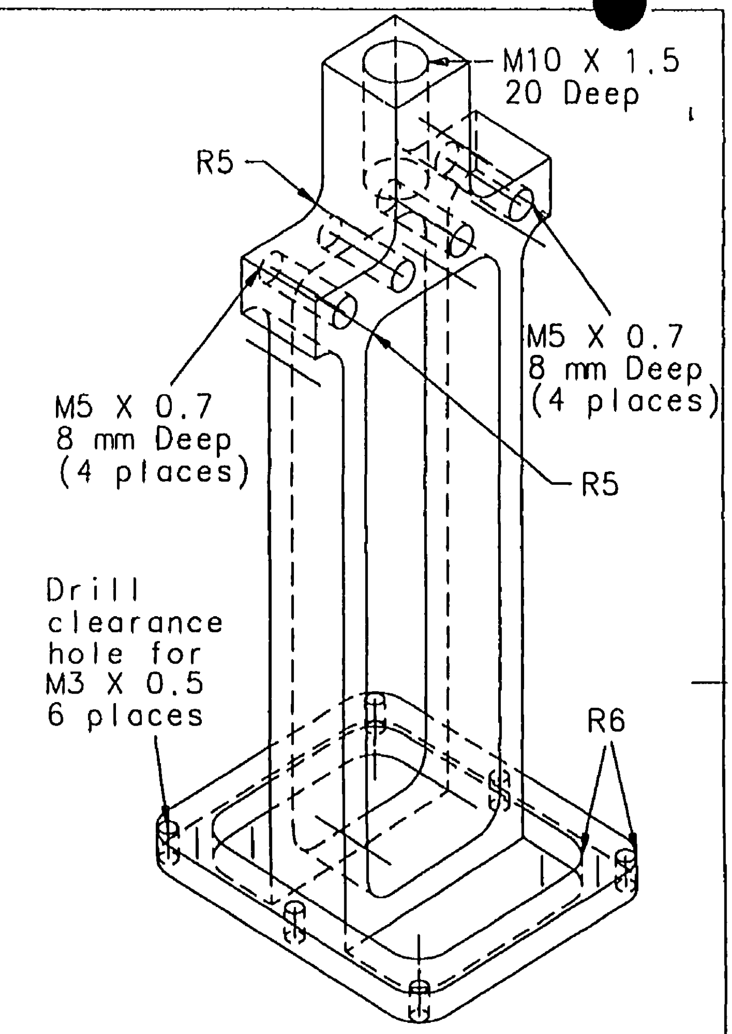

QTY REQD	FSCM NO	PART OR IDENTIFYING NO	NOMENCLATURE OR DESCRIPTION	MATERIAL SPECIFICATION	ITEM NO
1					

PARTS LIST

UNLESS OTHERWISE SPECIFIED DIMENSIONS ARE IN CENTIMETERS TOLERANCES ARE: ±.1 FRACTIONS ± DECIMALS .XX= ±.01 .XXX= ±.005 ANGLES ± DO NOT SCALE DRAWING	CONTRACT NO. 241-04-13-0		MATERIAL Aluminum 6061
	APPROVALS	DATE	TITLE FOREARM
TREATMENT NONE	DRAWN M. ROY	1/20	
	CHECKED V. HAYWARD		
FINISH 125			SIZE A4 / FSCM NO. / DWG NO. 14
SIMILAR TO / ACT. WT / CALC WT			SCALE N/A / UNITS: MM / SHEET 1 OF 1

N.B. M5 holes are to be threaded from two directions (not threaded all the way from only one side)

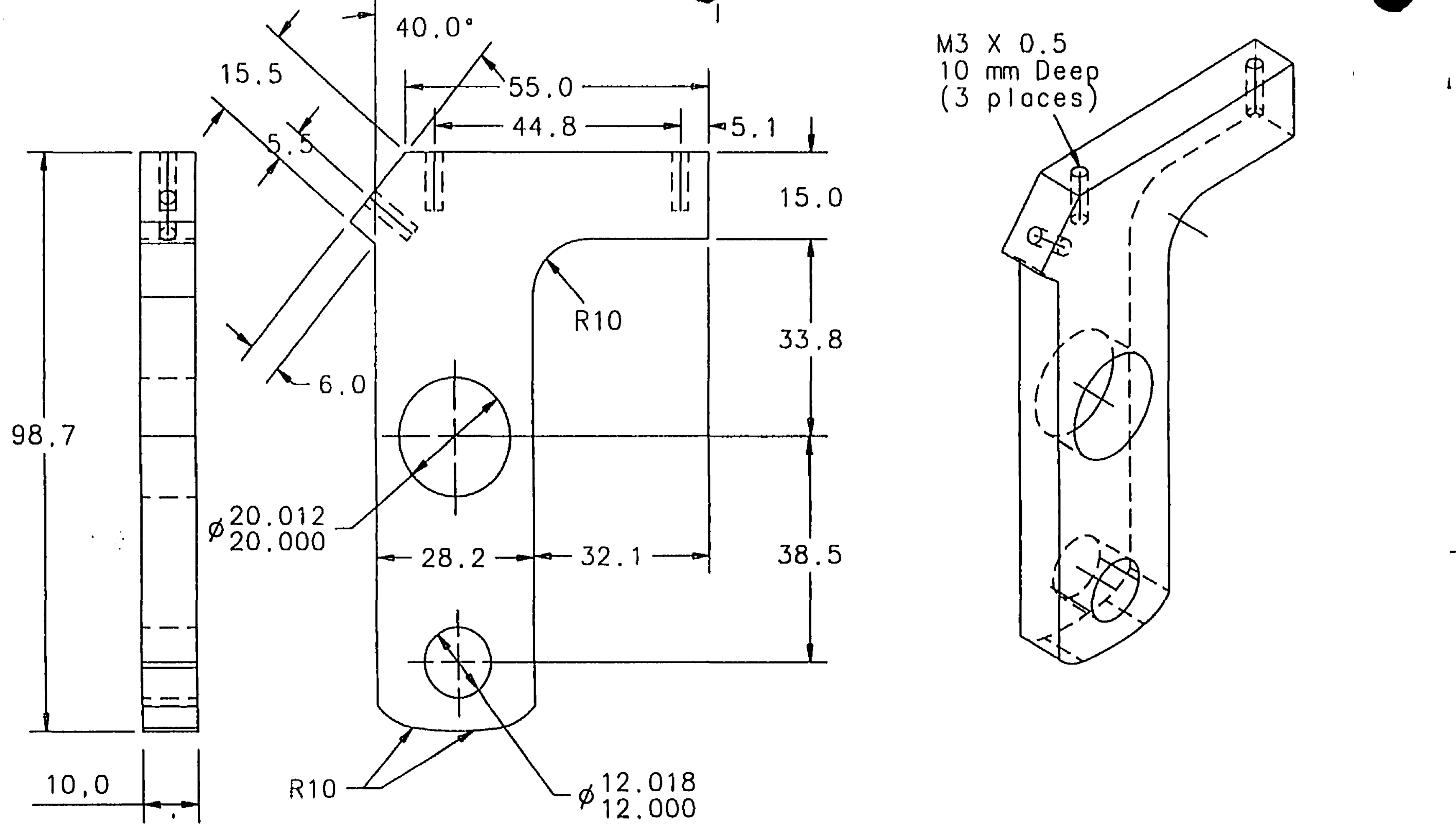

QTY REQD	FSCM NO	PART OR IDENTIFYING NO	NOMENCLATURE OR DESCRIPTION	MATERIAL SPECIFICATION	ITEM NO
1			PARTS LIST		

UNLESS OTHERWISE SPECIFIED DIMENSIONS ARE IN CENTIMETERS TOLERANCES ARE: .X = ±.1 FRACTIONS ± DECIMALS .XX= ±.01 .XXX= ±.003 ANGLES ± DO NOT SCALE DRAWING	CONTRACT NO.		Aluminum 6061
TREATMENT None	APPROVALS	DATE	TITLE RIGHT CAM PLATE
	DRAWN M. ROY	2/17	
FINISH 125	CHECKED V. HAYWARD		SIZE A4 FSCM NO. DWG NO. 15
SIMILAR TO ACT. WT CALC WT 76 g			SCALE N/A UNITS: mm SHEET 1 of 1

N.B. Align M3 Holes
with the holes on
Forearm (Dwg. 14)

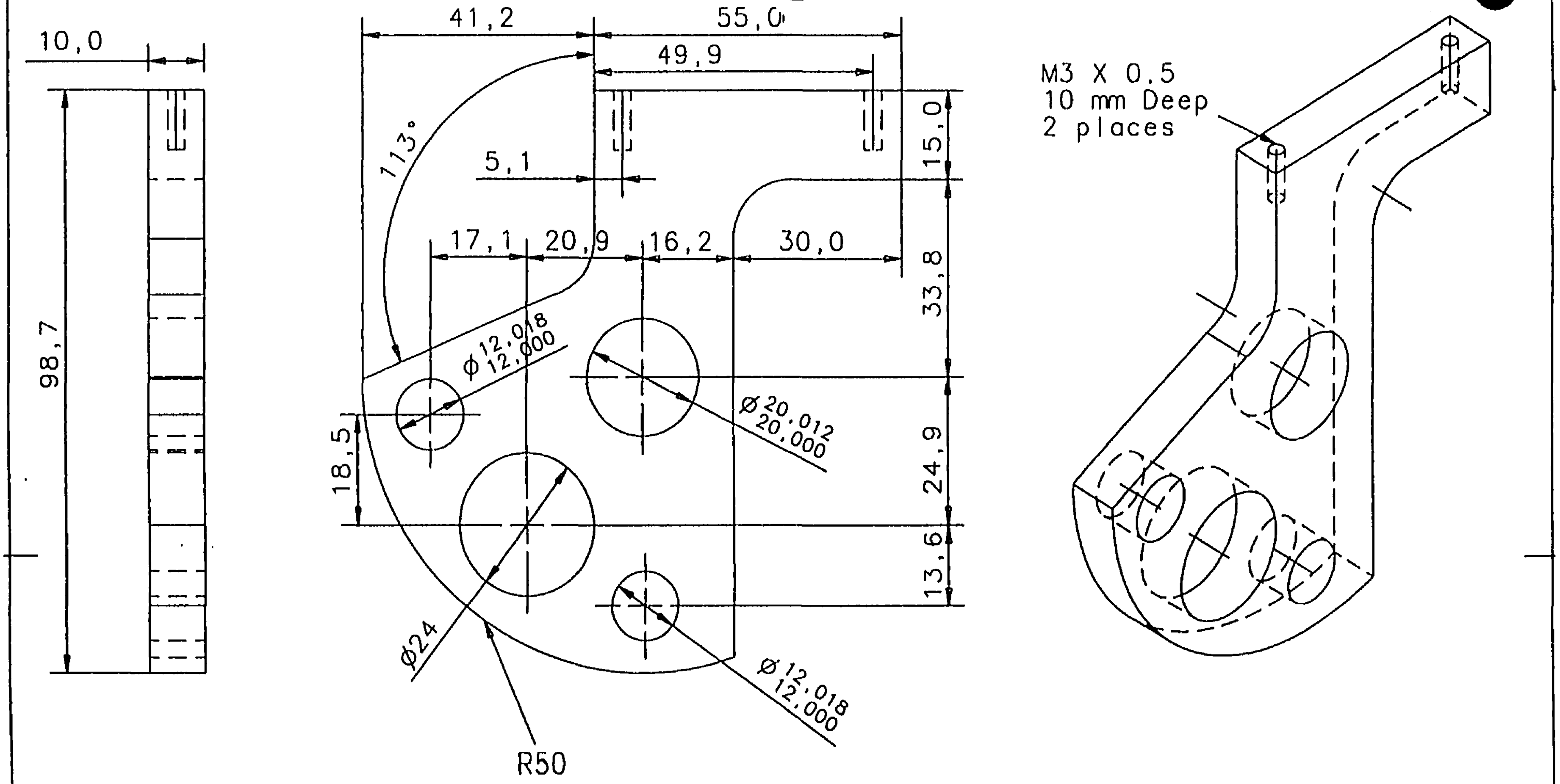

QTY REQD	FSCM NO	PART OR IDENTIFYING NO	NOMENCLATURE OR DESCRIPTION	MATERIAL SPECIFICATION	ITEM NO
1			PARTS LIST		

UNLESS OTHERWISE SPECIFIED DIMENSIONS ARE IN CENTIMETERS TOLERANCES ARE: .X = ±.1 FRACTIONS ± DECIMALS .XX= ±.01 .XXX= ±.005 ANGLES ±.1 DO NOT SCALE DRAWING	CONTRACT NO.		Aluminum 6061
	APPROVALS	DATE	TITLE CENTER CAM PLATE
TREATMENT None	DRAWN M. Roy	2/18	
FINISH 125	CHECKED V. Hayward		SIZE A4 FSCM NO. DWG NO. 16
SIMILAR TO ACT. WT CALC WT 103 g			SCALE N/A UNITS: MM SHEET 1 OF 1

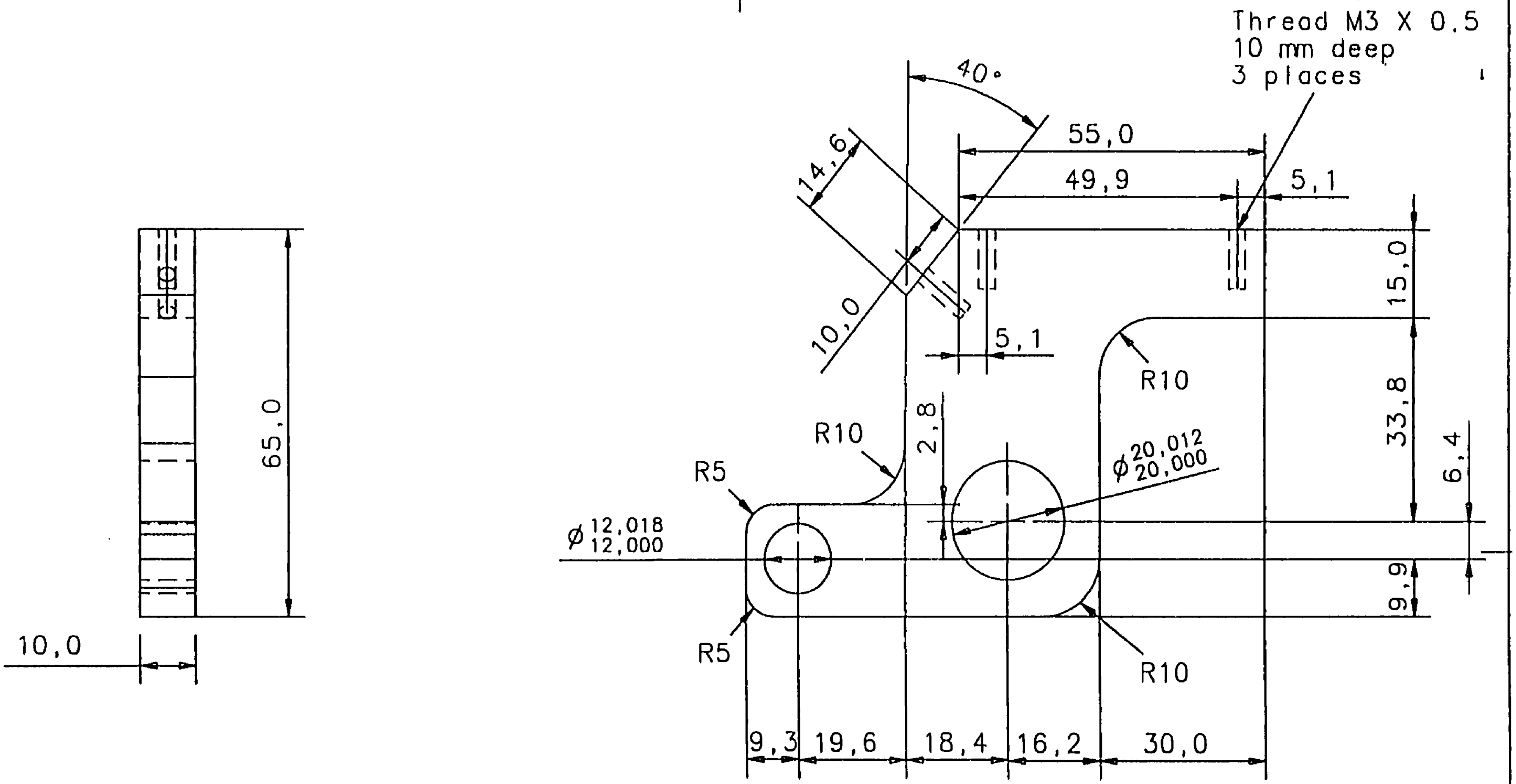

QTY REQD	FSCM NO	PART OR IDENTIFYING NO	NOMENCLATURE OR DESCRIPTION	MATERIAL SPECIFICATION	ITEM NO
1					

PARTS LIST

UNLESS OTHERWISE SPECIFIED DIMENSIONS ARE IN CENTIMETERS TOLERANCES ARE: .X = ±.1 FRACTIONS ± DECIMALS .XX= ±.01 .XXX= ±.005 ANGLES ±0.1 DO NOT SCALE DRAWING	CONTRACT NO.		Aluminum 6061
	APPROVALS	DATE	TITLE LEFT CAM PLATE
TREATMENT None	DRAWN M. Roy	2/19	
FINISH 125	CHECKED V. Hayword		SIZE A4 / FSCM NO. / DWG NO. 17
SIMILAR TO / ACT. WT / CALC WT 76 g			SCALE N/A / UNITS: MM / SHEET 1 OF 1

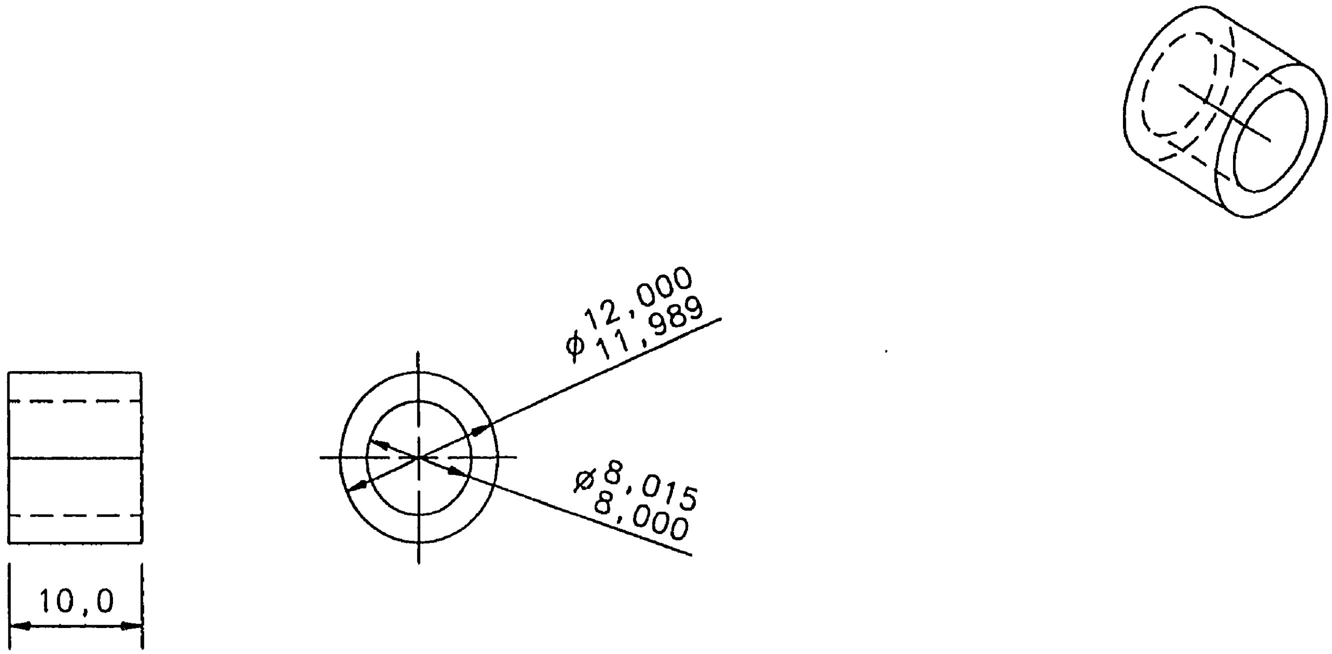

QTY REQD	FSCM NO	PART OR IDENTIFYING NO	NOMENCLATURE OR DESCRIPTION	MATERIAL SPECIFICATION	ITEM NO
4					

PARTS LIST

UNLESS OTHERWISE SPECIFIED DIMENSIONS ARE IN CENTIMETERS
TOLERANCES ARE:
FRACTIONS ± DECIMALS .XX= ±.25 .XXX= ±.125 ANGLES ±.25
DO NOT SCALE DRAWING

TREATMENT None
FINISH 125
SIMILAR TO
ACT. WT
CALC WT

CONTRACT NO.

APPROVALS		DATE
DRAWN	M. Roy	2/19
CHECKED	V. Hayward	

MATERIAL Brass
TITLE BRASS BUSHING
SIZE A4
FSCM NO.
DWG NO. 18
SCALE N/A UNITS: MM SHEET 1 OF 1

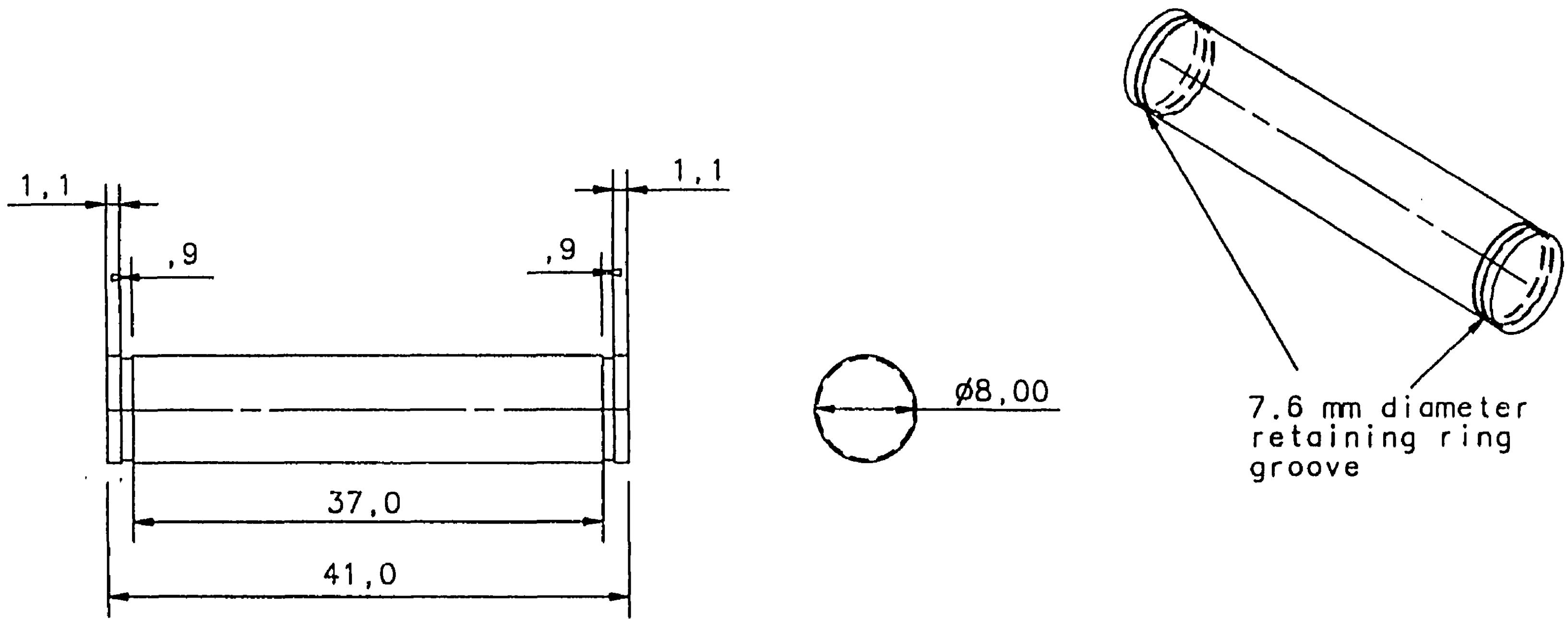

QTY REQD	FSCM NO	PART OR IDENTIFYING NO	NOMENCLATURE OR DESCRIPTION	MATERIAL SPECIFICATION	ITEM NO
2			PARTS LIST		

UNLESS OTHERWISE SPECIFIED
DIMENSIONS ARE IN CENTIMETERS
TOLERANCES ARE: ,X = ±0,1
FRACTIONS ± DECIMALS ,XX= ±0,01 ,XXX=±0,005 ANGLES ±
DO NOT SCALE DRAWING

TREATMENT None

FINISH 125

SIMILAR TO | ACT. WT | CALC WT

CONTRACT NO.

APPROVALS		DATE
DRAWN	M. Roy	2/20
CHECKED	V. Hoyword	

Steel (dowel pin)

TITLE PIN

SIZE A4 | FSCM NO. | DWG NO. 19

SCALE N/A | UNITS: MM | SHEET 1 OF 1

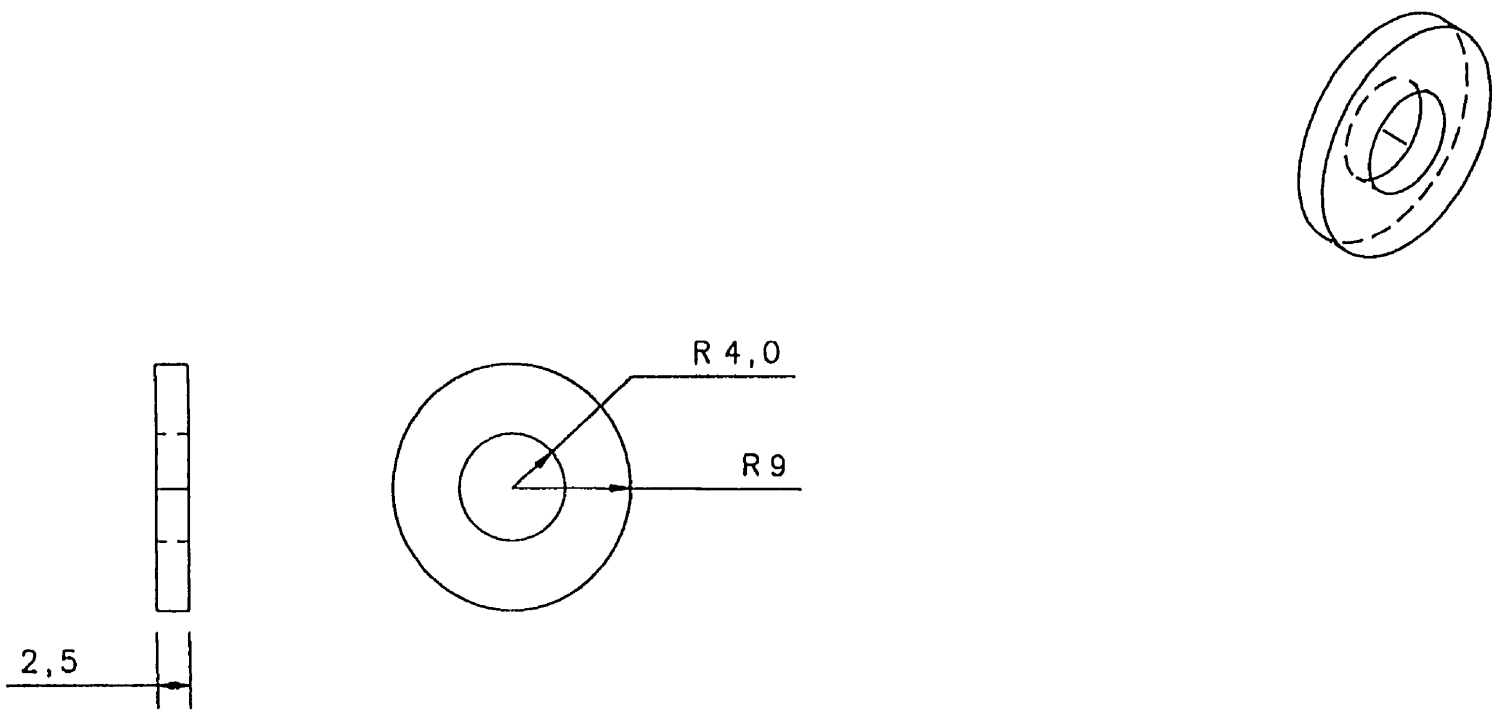

QTY REQD	FSCM NO	PART OR IDENTIFYING NO	NOMENCLATURE OR DESCRIPTION	MATERIAL SPECIFICATION	ITEM NO
4			PARTS LIST		

UNLESS OTHERWISE SPECIFIED DIMENSIONS ARE IN CENTIMETERS TOLERANCES ARE: .X = ±0.1
FRACTIONS ± DECIMALS .XX= ±.01 .XXX= ±.005 ANGLES ±
DO NOT SCALE DRAWING

TREATMENT None

FINISH

SIMILAR TO | ACT. WT | CALC WT

CONTRACT NO.

APPROVALS		DATE
DRAWN	M. Roy	2/20
CHECKED	V. Hayward	

MATERIAL Delrin

TITLE PIN SPACER

SIZE A4 | FSCM NO. | DWG NO. 20

SCALE N/A | UNITS: MM | SHEET 1 OF 1

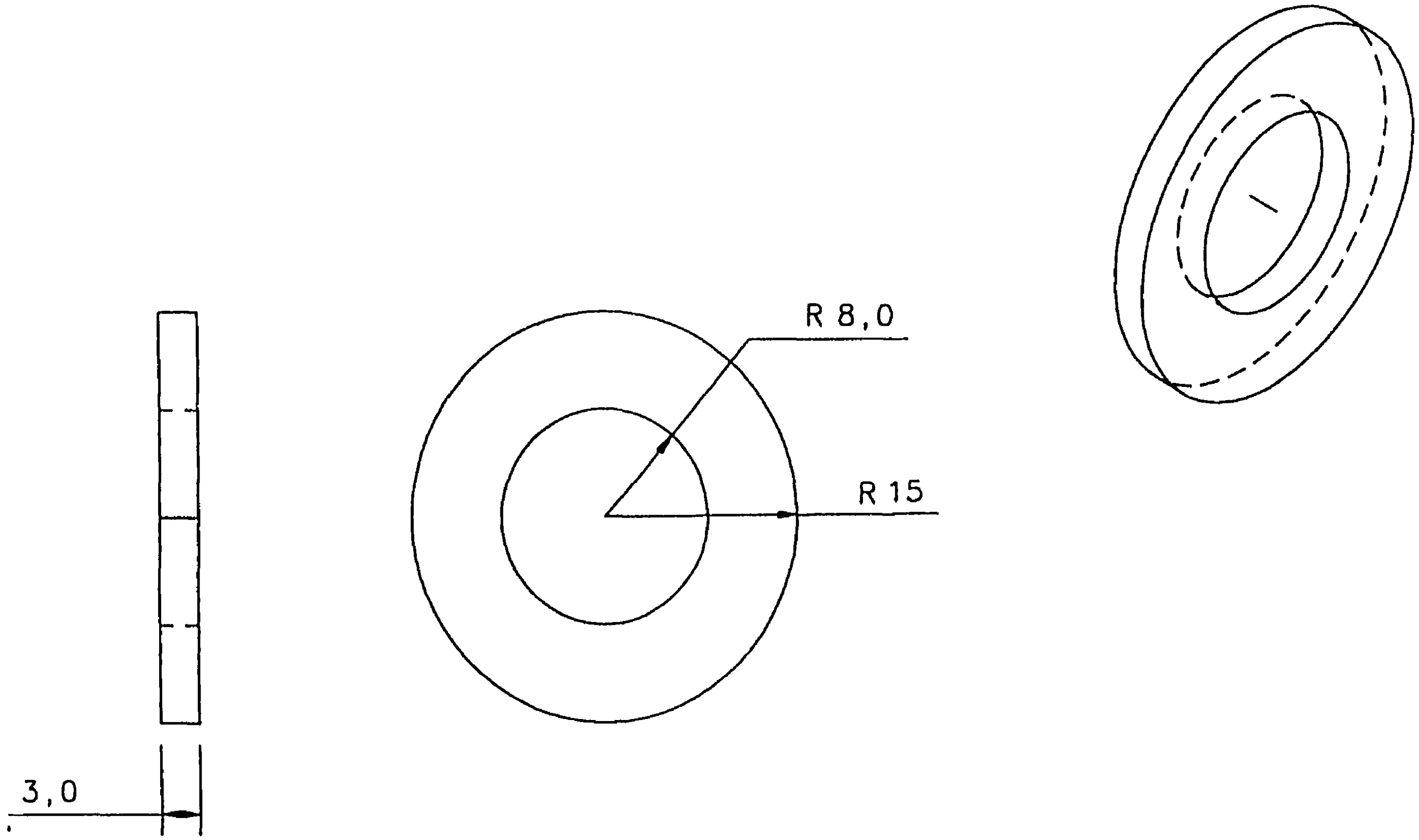

QTY REQD	FSCM NO	PART OR IDENTIFYING NO	NOMENCLATURE OR DESCRIPTION	MATERIAL SPECIFICATION	ITEM NO
2			PARTS LIST		

UNLESS OTHERWISE SPECIFIED DIMENSIONS ARE IN CENTIMETERS
TOLERANCES ARE: .X = ±.1

FRACTIONS	DECIMALS	ANGLES
±	.XX= ±.01 .XXX=±.005	±

DO NOT SCALE DRAWING

TREATMENT: None

FINISH:

SIMILAR TO: | ACT. WT | CALC WT

CONTRACT NO.:

APPROVALS		DATE
DRAWN	M. Roy	2/20
CHECKED	V. Hayward	

MATERIAL: Delrin

TITLE: ELBOW SPACER

SIZE: A4 | FSCM NO.: | DWG NO.: 21

SCALE: N/A | UNITS: MM | SHEET 1 OF 1

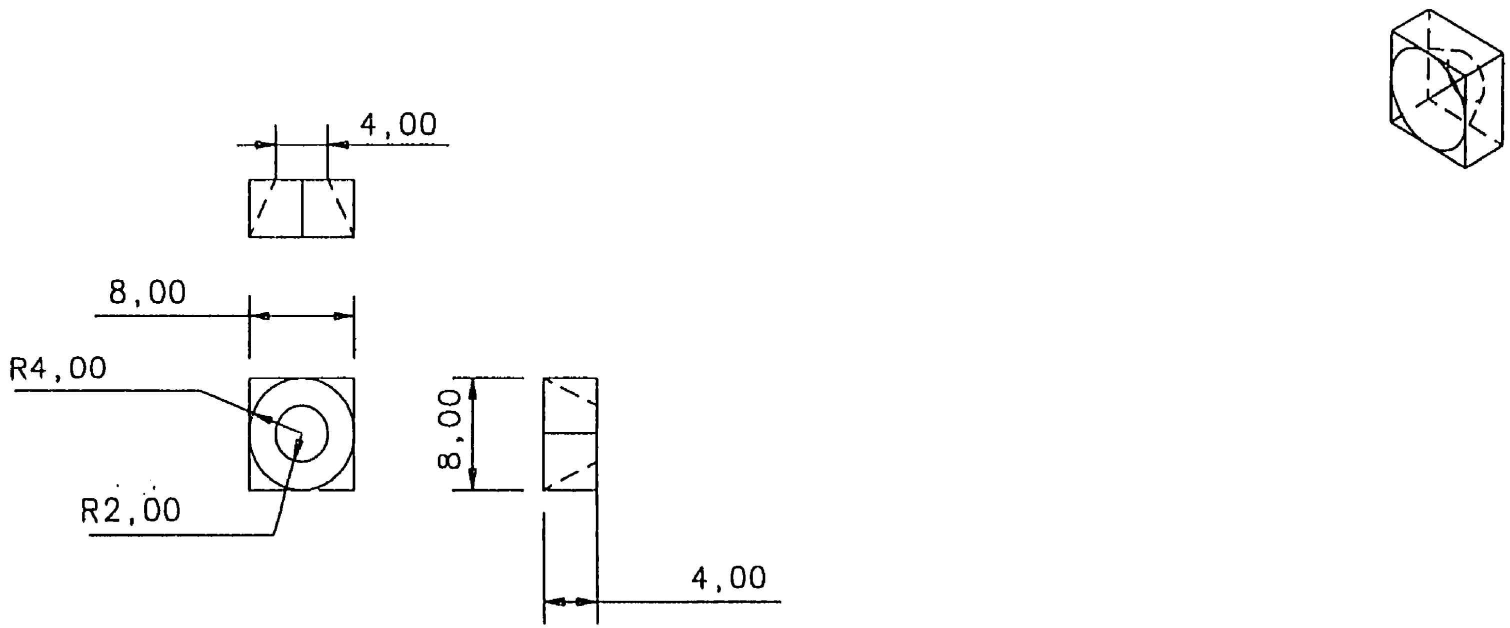

QTY REQD	FSCM NO	PART OR IDENTIFYING NO	NOMENCLATURE OR DESCRIPTION	MATERIAL SPECIFICATION	ITEM NO
4					

PARTS LIST

UNLESS OTHERWISE SPECIFIED DIMENSIONS ARE IN CENTIMETERS TOLERANCES ARE: .X = ±.1 FRACTIONS ± DECIMALS .XX= ±.01 .XXX= ±.005 ANGLES ± DO NOT SCALE DRAWING	CONTRACT NO.		Delrin
	APPROVALS	DATE	TITLE CONICAL SPACER
TREATMENT None	DRAWN M. Roy	2/25	
FINISH	CHECKED V. Hayward		SIZE A4 FSCM NO. DWG NO. 22
	L. Lessard		
SIMILAR TO ACT. WT CALC WT			SCALE N/A UNITS: MM SHEET 1 OF 1

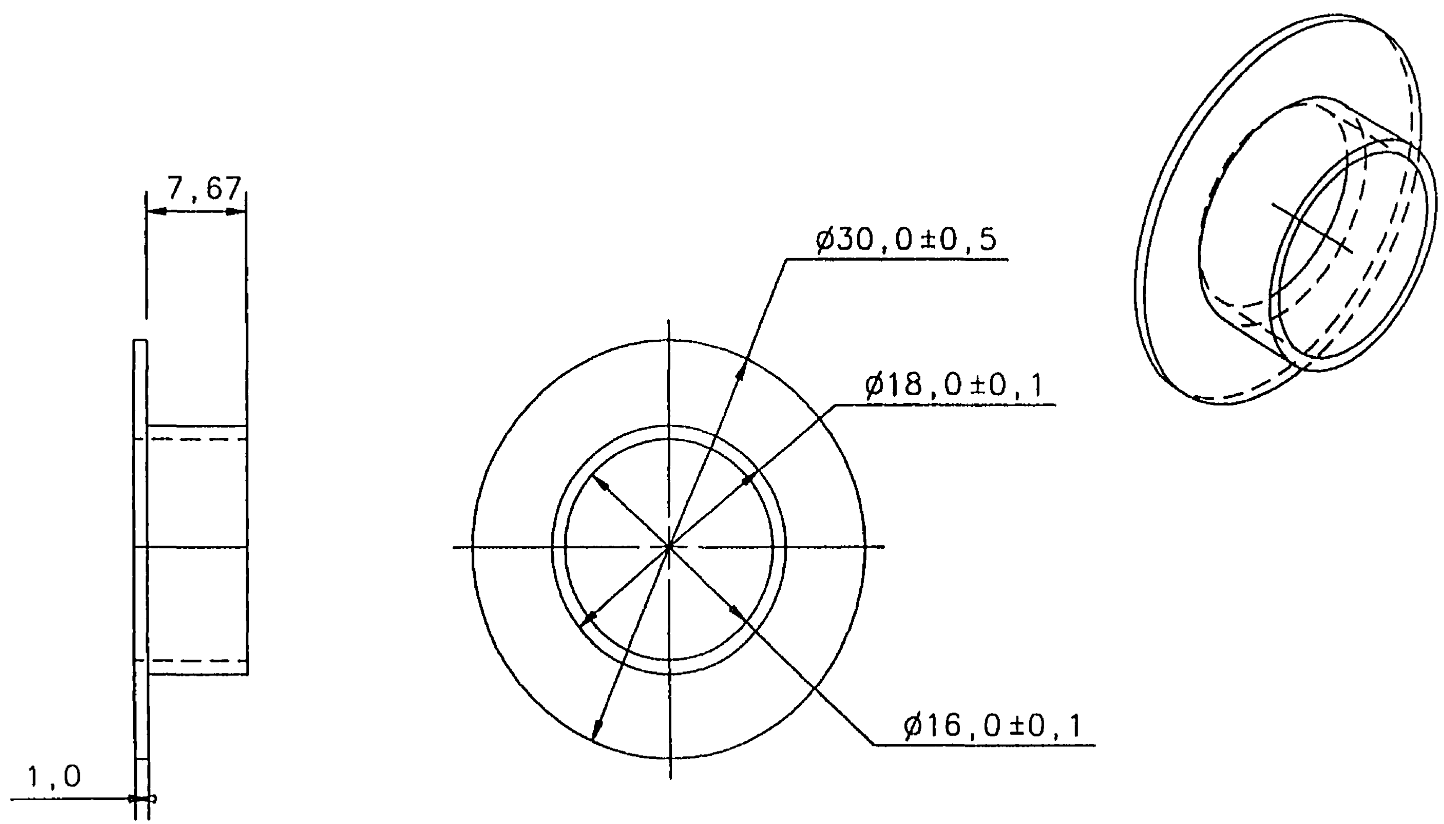

QTY REQD	FSCM NO	PART OR IDENTIFYING NO	NOMENCLATURE OR DESCRIPTION	MATERIAL SPECIFICATION	ITEM NO
4			PARTS LIST	ASTM A581	

UNLESS OTHERWISE SPECIFIED DIMENSIONS ARE IN CENTIMETERS TOLERANCES ARE:
FRACTIONS ± DECIMALS .XX- .XXX- ANGLES ±
DO NOT SCALE DRAWING

TREATMENT: Annealed	CONTRACT NO.	MATERIAL: Stainless Steel 303
FINISH: 125	APPROVALS / DATE	TITLE: COLLAR INSERT
SIMILAR TO / ACT. WT / CALC WT	DRAWN: M. Roy — 3/12	SIZE: A4 — FSCM NO. — DWG NO. 23
	CHECKED: L. Lessard	SCALE N/A — UNITS: MM — SHEET 1 OF 1

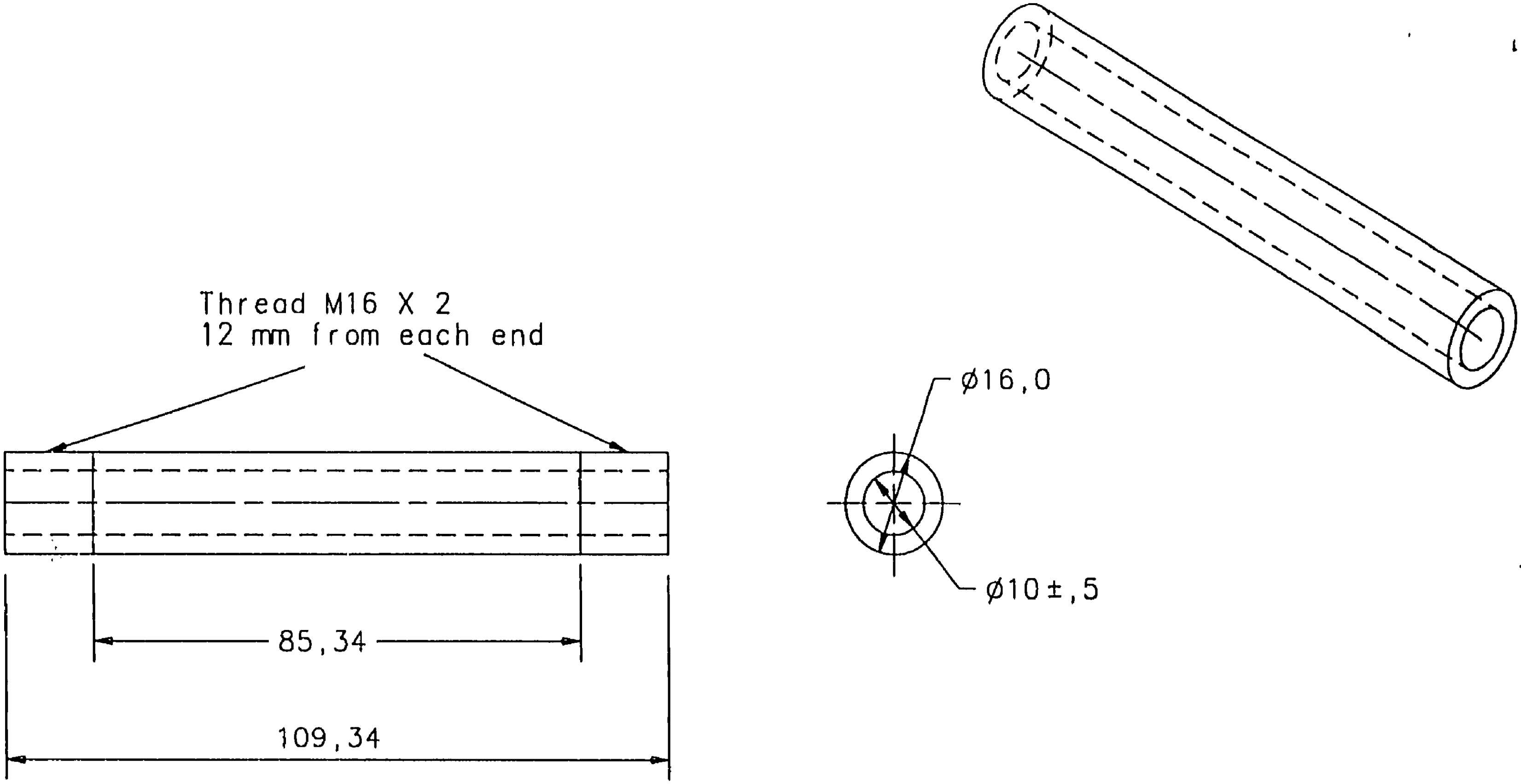

QTY REQD	FSCM NO	PART OR IDENTIFYING NO	NOMENCLATURE OR DESCRIPTION	MATERIAL SPECIFICATION	ITEM NO
2			PARTS LIST		

UNLESS OTHERWISE SPECIFIED DIMENSIONS ARE IN CENTIMETERS TOLERANCES ARE: ,X = ±0,1 FRACTIONS ± DECIMALS ,XX=±,01 ,XXX=±,005 ANGLES ± DO NOT SCALE DRAWING	CONTRACT NO. 241-04-13-0		MATERIAL Steel 4340	
	APPROVALS	DATE	TITLE MAIN SHAFT	
TREATMENT Annealed	DRAWN M. Roy	3/12		
FINISH 125	CHECKED L. Lessard		SIZE A4 FSCM NO.	DWG NO. 24
	V. Hayward			
SIMILAR TO / ACT. WT / CALC WT			SCALE N/A UNITS: MM	SHEET 1 OF 1

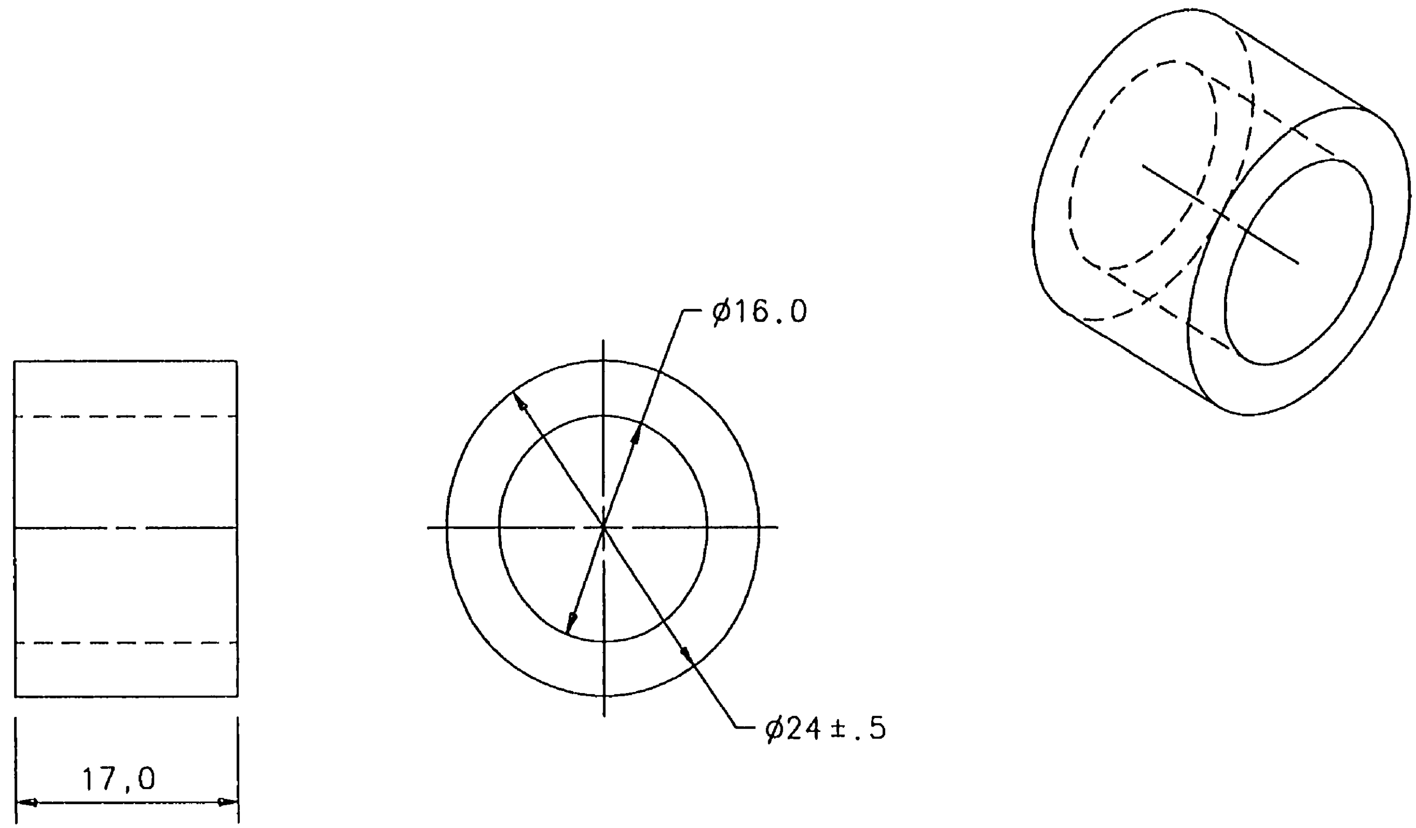

QTY REQD	FSCM NO	PART OR IDENTIFYING NO	NOMENCLATURE OR DESCRIPTION	MATERIAL SPECIFICATION	ITEM NO
2			PARTS LIST		

UNLESS OTHERWISE SPECIFIED
DIMENSIONS ARE IN CENTIMETERS
TOLERANCES ARE: .X = ±0.1
FRACTIONS DECIMALS ANGLES
± .XX= ±
.XXX=
DO NOT SCALE DRAWING

TREATMENT None

FINISH

SIMILAR TO | ACT. WT | CALC WT

CONTRACT NO. 241-04-13-0

APPROVALS	DATE
DRAWN M. Roy	3/13
CHECKED V. Hayward	
L. Lessard	

MATERIAL Delrin

TITLE MAIN SHAFT SPACER

SIZE A4 | FSCM NO. | DWG NO. 25

SCALE N/A | UNITS: MM | SHEET 1 OF 1

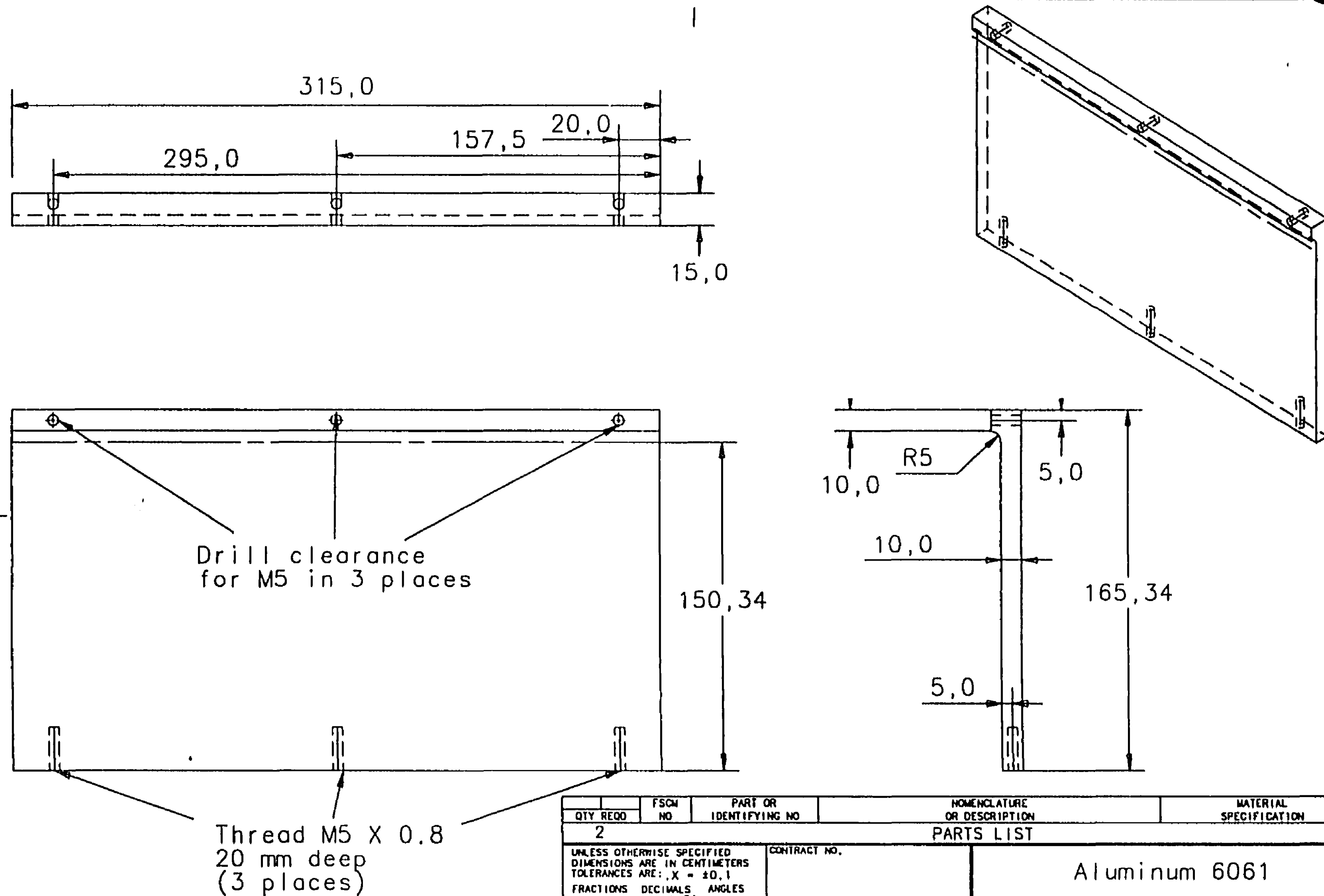

QTY REQD	FSCM NO	PART OR IDENTIFYING NO	NOMENCLATURE OR DESCRIPTION	MATERIAL SPECIFICATION	ITEM NO
2			PARTS LIST		

UNLESS OTHERWISE SPECIFIED DIMENSIONS ARE IN CENTIMETERS TOLERANCES ARE: .X = ±0.1
FRACTIONS ± DECIMALS .XX=±.01 .XXX=±.005 ANGLES ±
DO NOT SCALE DRAWING

TREATMENT None

FINISH 125

SIMILAR TO | ACT. WT | CALC WT

CONTRACT NO.

APPROVALS		DATE
DRAWN	M. Roy	3/14
CHECKED	L. Lessard	

Aluminum 6061

TITLE LARGE MOLD PLATE

SIZE A4 | FSCM NO. | DWG NO. 26

SCALE N/A | UNITS: MM | SHEET 1 OF 1

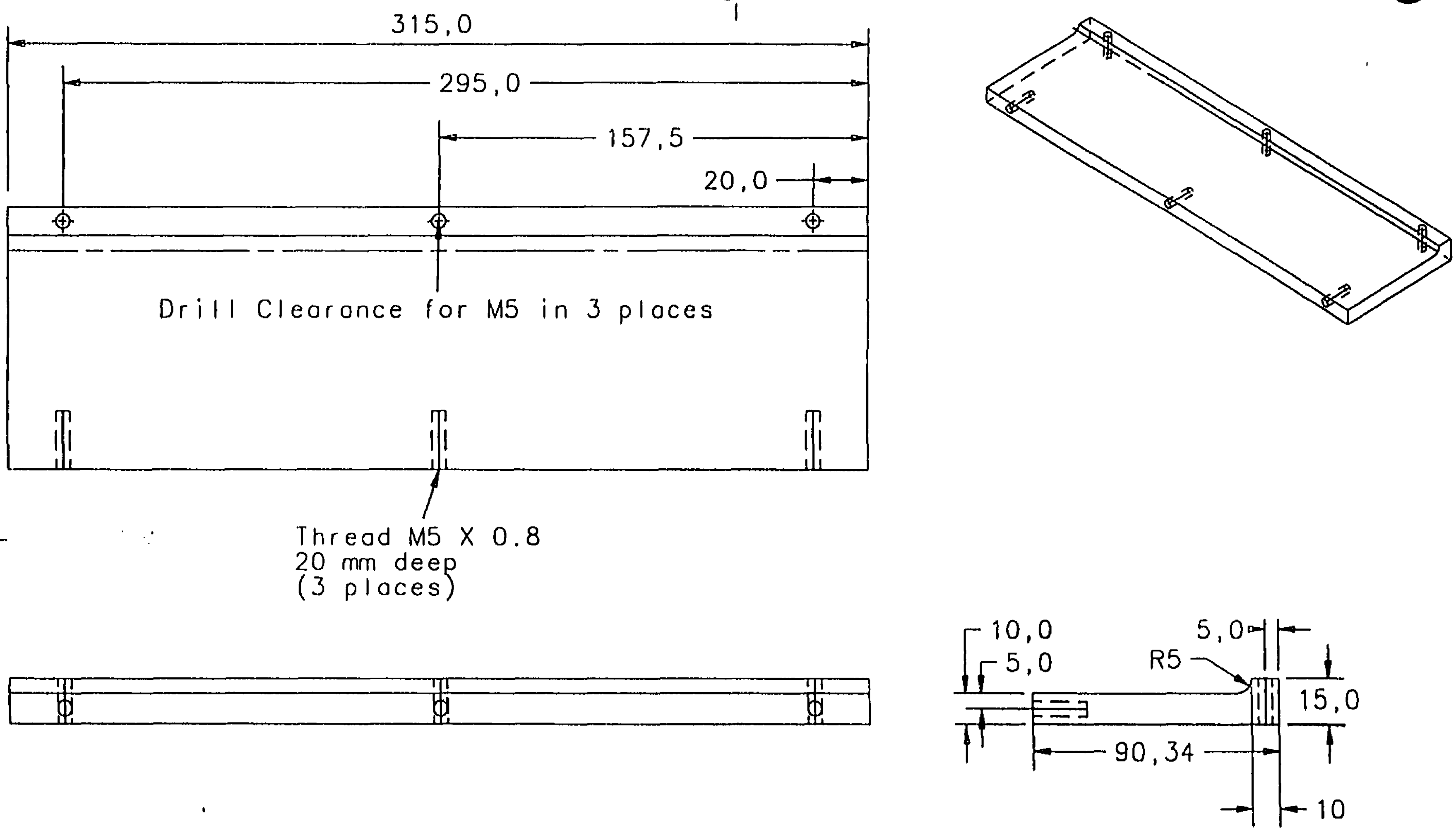

QTY REQD		FSCM NO	PART OR IDENTIFYING NO	NOMENCLATURE OR DESCRIPTION	MATERIAL SPECIFICATION	ITEM NO
2				PARTS LIST		

UNLESS OTHERWISE SPECIFIED DIMENSIONS ARE IN CENTIMETERS TOLERANCES ARE: .X = ±0.1
FRACTIONS ± DECIMALS .XX= ±.01 .XXX= ±.005 ANGLES ±
DO NOT SCALE DRAWING

TREATMENT None

FINISH 125

SIMILAR TO | ACT. WT | CALC WT

CONTRACT NO. 241-04-13-0

APPROVALS		DATE
DRAWN	M. Roy	3/14
CHECKED	L. Lessard	

Aluminum 6061

TITLE SMALL MOLD PLATE

SIZE A4 | FSCM NO. | DWG NO. 27

SCALE N/A | UNITS: MM | SHEET 1 OF 1

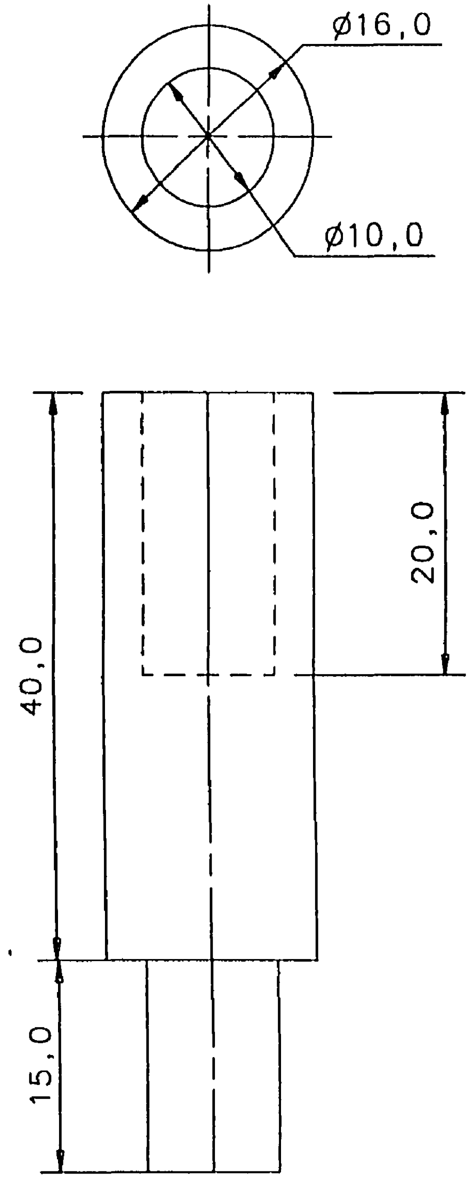

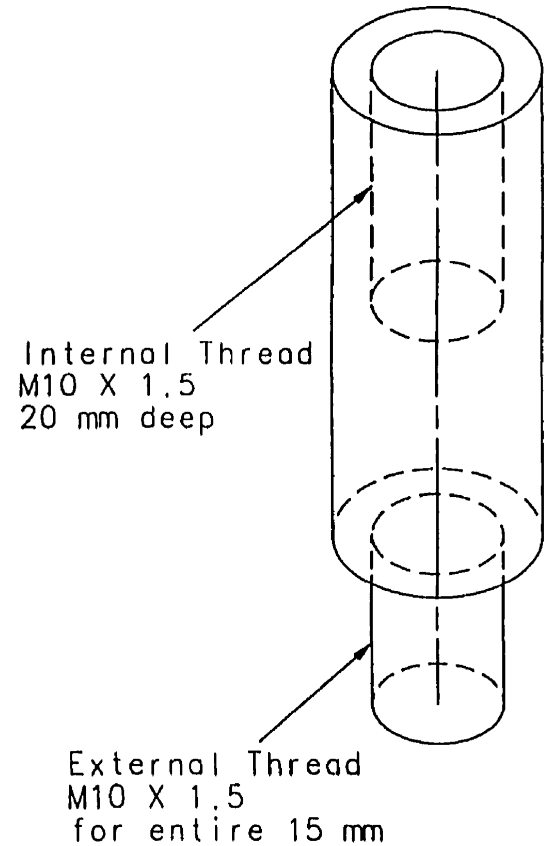

QTY REQD	FSCM NO	PART OR IDENTIFYING NO	NOMENCLATURE OR DESCRIPTION	MATERIAL SPECIFICATION	ITEM NO
1			PARTS LIST		

UNLESS OTHERWISE SPECIFIED DIMENSIONS ARE IN CENTIMETERS TOLERANCES ARE: .X = ±0.5 FRACTIONS ± DECIMALS .XX= .XXX= ANGLES ± DO NOT SCALE DRAWING	CONTRACT NO. 241-04-13-0	Aluminum 6061
TREATMENT None	APPROVALS / DATE	TITLE ADAPTOR
	DRAWN M. Roy 3/14	
FINISH 125	CHECKED L. Lessard	SIZE A4 FSCM NO. DWG NO. 28
SIMILAR TO ACT. WT CALC WT	V. Hayward	SCALE N/A UNITS: MM SHEET 1 OF 1

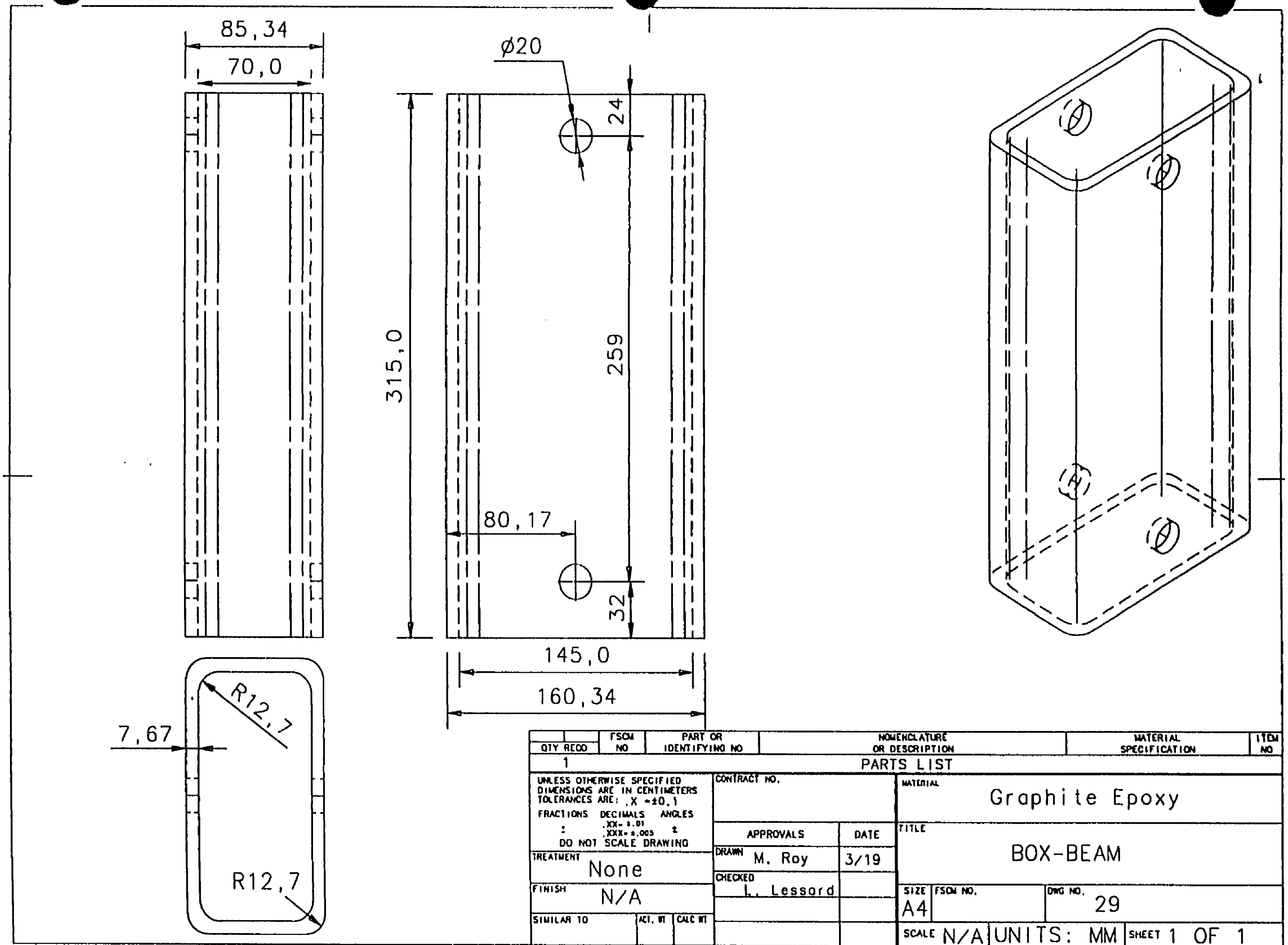

QTY REQD	FSCM NO	PART OR IDENTIFYING NO	NOMENCLATURE OR DESCRIPTION	MATERIAL SPECIFICATION	ITEM NO
1			PARTS LIST		

UNLESS OTHERWISE SPECIFIED DIMENSIONS ARE IN CENTIMETERS
TOLERANCES ARE: .X = ±0.1
FRACTIONS : DECIMALS .XX = ±.01 .XXX = ±.005 ANGLES ±
DO NOT SCALE DRAWING

TREATMENT	None
FINISH	N/A
SIMILAR TO	
ACT. WT	
CALC WT	
CONTRACT NO.	

APPROVALS		DATE
DRAWN	M. Roy	3/19
CHECKED	L. Lessord	

MATERIAL	Graphite Epoxy
TITLE	BOX-BEAM
SIZE	A4
FSCM NO.	
DWG NO.	29
SCALE	N/A
UNITS:	MM
SHEET	1 OF 1

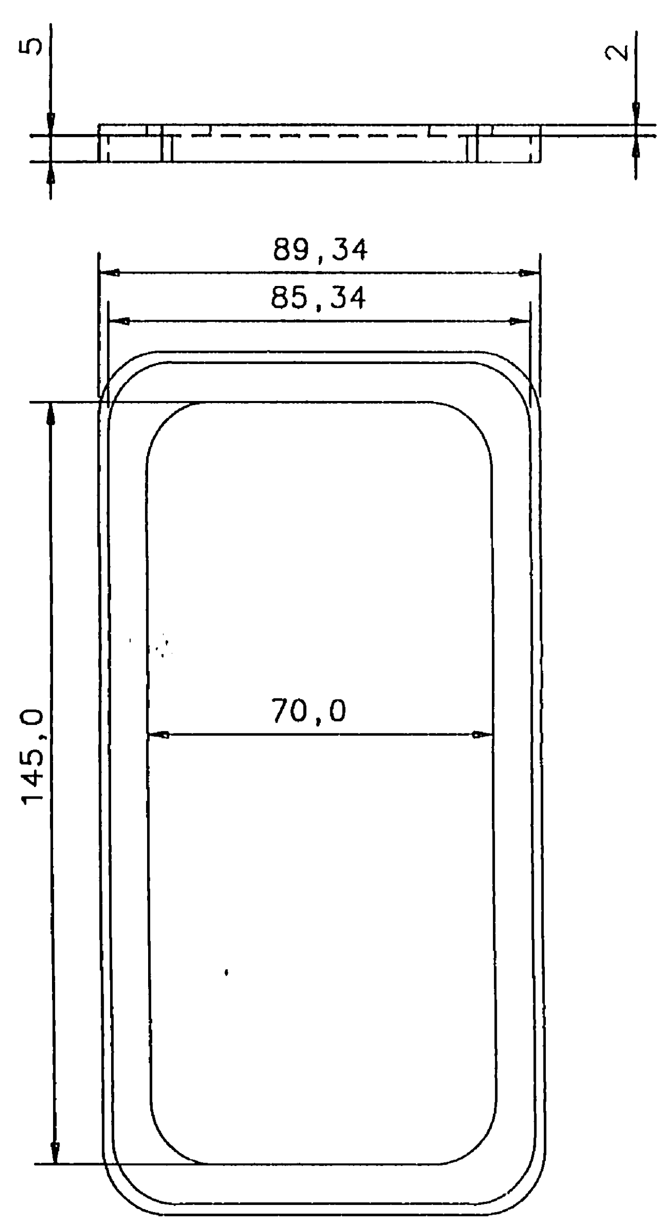

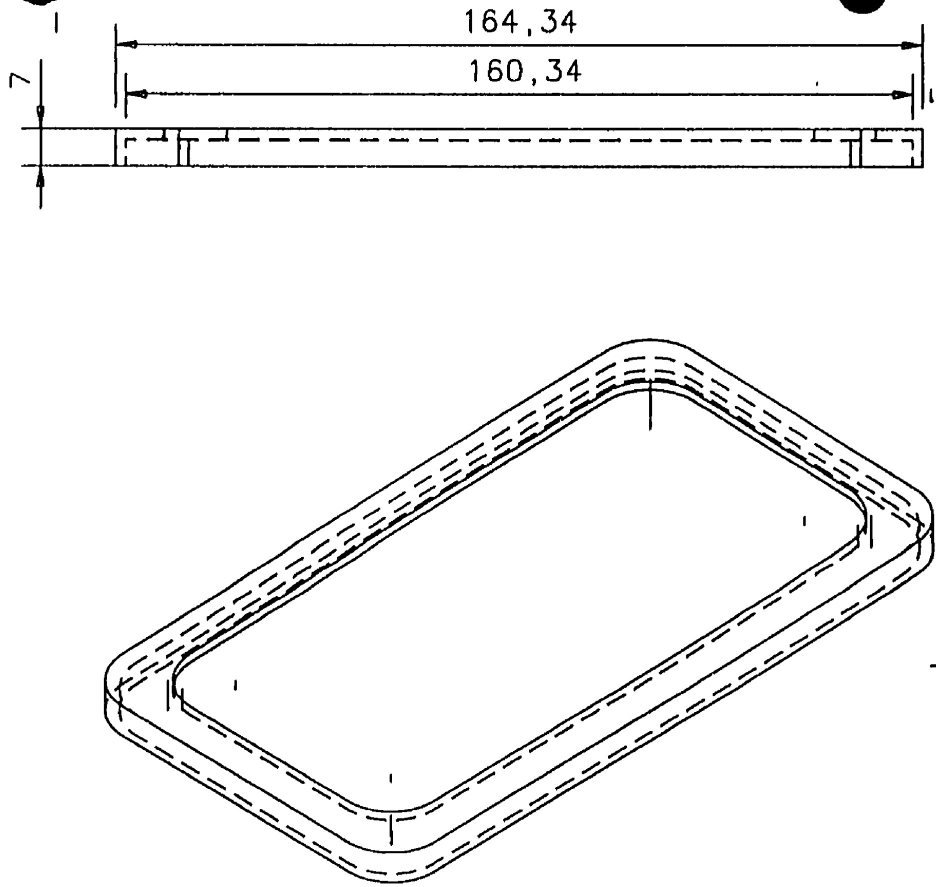

QTY REQD	FSCM NO	PART OR IDENTIFYING NO	NOMENCLATURE OR DESCRIPTION	MATERIAL SPECIFICATION	ITEM NO
1					

PARTS LIST

UNLESS OTHERWISE SPECIFIED
DIMENSIONS ARE IN CENTIMETERS
TOLERANCES ARE: .X = ±0.1
FRACTIONS ± DECIMALS .XX= ±.01 .XXX= ANGLES ±
DO NOT SCALE DRAWING

TREATMENT

FINISH

SIMILAR TO | ACT. WT | CALC WT

CONTRACT NO. 241-04-13-0

APPROVALS		DATE
DRAWN	M. Roy	3/24
CHECKED	L. Lessard	

MATERIAL Black Delrin

TITLE CAP

SIZE A4 | FSCM NO. | DWG NO. 30

SCALE N/A | UNITS: MM | SHEET 1 OF 1

Appendix B: Radii of Gyration

If a link has a mass *m* and a moment of inertia *I* about an axis, then the radius of gyration *k* about that same axis is defined as follows:

$$k = \sqrt{\frac{I}{m}}$$

Link	k_X	k_Y	k_Z
Shoulder	27	9	27
Elbow	277	52	274
Forearm	492	25	492
Wrist	642	11	642
Hand/Gripper	716	32	716

N.B. All radii are in mm.

Appendix C: Budget

The bulk of the cost of the Lightarm project was due to machining, which was done at McGill in both the Department of Mechanical Engineering and the Physics Department and at Progressive Machine Works in Anjou. Given that the hourly rate at McGill is $35 and at PMW $65 (where the graphite/epoxy was machined), it is possible to estimate the machining time of the various components of Lightarm.

Item	Cost
Steel Supports	$150.00
Stainless Steel H-Base & Plate	$2000.70
Stainless Steel Shafts & Bushings	$245.00
Adapter & Sleeves	$115.00
U-Joint & Centercube	$1260.00
Elbow Piston Output Linkages (EPOL)	$135.00
LVDT Holders	$377.50
Bearing Shafts & Modifications to EPOL	$505.00
Forearm & Conical Shaft Modifications	$1015.00
Cam Plates	$580.00
Stainless Steel End-fitting	$600.00
Aluminum Mold	$630.00
Drilling Holes in Graphite Box-Beam	$150.00
Milling Slot in Graphite Box-Beam	$68.38
TOTAL	$7831.58

Appendix D: Corrosion of Graphite with Various Metals

ANODIC
(most active)
↓
Magnesium alloys
Zinc
Alclad 7000-series aluminum alloys
5000-series aluminum alloys
7000-series aluminum alloys
Pure aluminum and alclad 2000-series alloys
Cadmium
2000-series aluminum alloys
Steel and iron
Lead
Chromium
Brass and bronze alloys
Copper
Precipitation-Hardened Stainless Steel
Martensitic Stainless Steel
Ferritic Stainless Steel
Austenitic Stainless Steel
Titanium
Silver
Nickel
Gold
Graphite
↓
CATHODIC
(least active)

Adapted from Ref. [89]

IMAGE EVALUATION
TEST TARGET (QA-3)

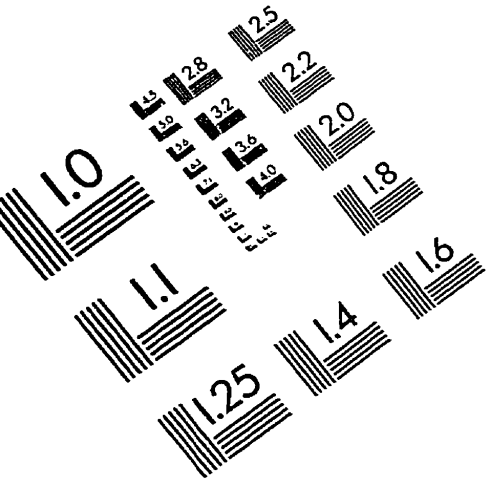

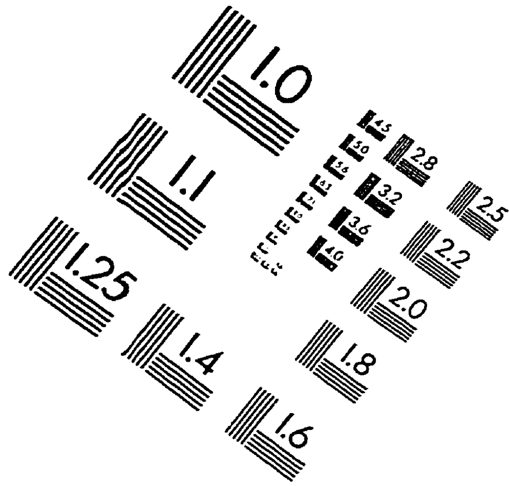

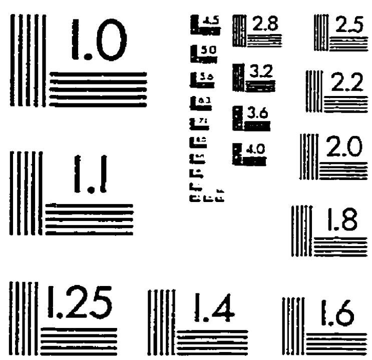

150mm

6"

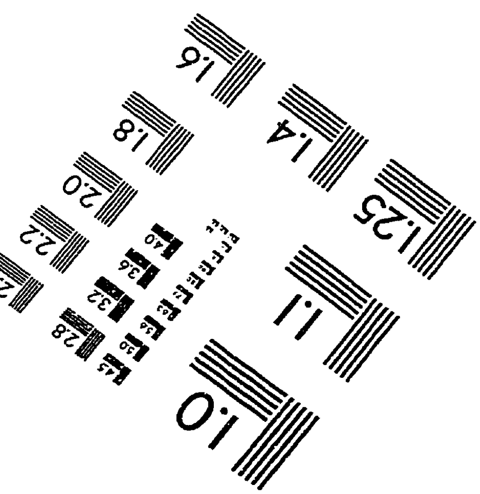

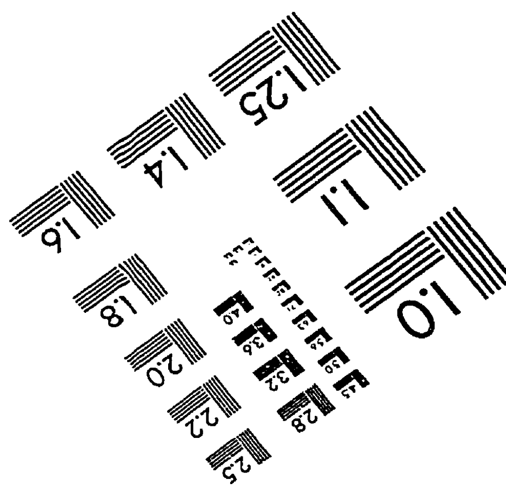

APPLIED IMAGE, Inc
1653 East Main Street
Rochester, NY 14609 USA
Phone: 716/482-0300
Fax: 716/288-5989